NISTIR 6793

Laser - Assisted Vaporization Mass Spectrometry: Application to Thermochemistry at Very High Temperatures

J. W. Hastie
D. W. Bonnell
P. K. Schenck

NIST
National Institute of Standards and Technology
Technology Administration, U.S. Department of Commerce

NISTIR 6793

Laser - Assisted Vaporization Mass Spectrometry: Application to Thermochemistry at Very High Temperatures

J. W. Hastie
D. W. Bonnell
P. K. Schenck
Ceramics Division

MSEL

September 2001

U.S. Department of Commerce
Donald L. Evans, Secretary

National Institute of Standards and Technology
Karen H. Brown, Acting Director

Table of Contents

Laser-Assisted Vaporization Mass Spectrometry: Application to Thermochemistry at Very High Temperatures

J.W. Hastie, D.W. Bonnell, P.K. Schenck
N.I.S.T., Gaithersburg, MD, U.S.A.

Abstract

Classical mass spectrometrically-based approaches to the determination of high temperature thermochemical data and functions are limited in their applicable ranges of temperature and vapor pressure. An earlier laser-based mass spectrometric approach substantially overcame these limitations, but with reduced precision in temperature and pressure determination. Here, we present new methods that largely resolve the earlier limitations of laser-assisted vaporization mass spectrometry, thereby greatly expanding the scope of application of high temperature mass spectrometric techniques to ceramics and other refractory systems.

Keywords: High temperature, mass spectrometry, thermodynamic data, laser heating, vapor pressure, ionization cross sections.

1. Introduction

Ceramics are characteristically high melting, high boiling temperature materials as may be seen in Table 1. The listed temperatures are for the most part not well established, particularly the literature boiling temperatures at 1 bar (1 bar = 10^5 Nm^{-2}) total pressure (as obtained from [A.1, A.2]).[a] The boiling temperatures from the present study do not rely on an extrapolation of lower temperature data and are listed in the table for the systems: ZrO_2 , Y_2O_3 , HfO_2 , Al_2O_3 , $BaTiO_3$, C, SiC, and BN (as B(ℓ)). Also of note in Table 1 is the complexity of the vapor phase which, from lower temperature studies, is expected to comprise a number of atomic and molecular species. Accordingly, the thermochemical characterization of these systems requires use of a molecular-specific technique such as mass spectrometry.

The thermochemical and related phase equilibria properties of refractory materials at very high temperatures, particularly for the liquid phase, are either unknown or are based on an extrapolation of lower temperature data [A.1, A.2]. As temperature increases, the vapor phase becomes a significant component of any material system, with diverse consequences for materials processing and performance [A.6]. Thermodynamic databases are widely used for modeling complex materials behavior and the data for vapor phase constituents are derived largely from high temperature mass spectrometry (HTMS), as may be seen in [A.1, A.2].

A detailed discussion of the procedures and uncertainties associated with conventional HTMS methods has recently been given elsewhere [A.19]. With the Knudsen cell mass spectrometric (KMS) approach, the upper limits of application with respect to temperature and vapor pressure are ≈2500 K and ≈10^{-4} bar. A practical upper temperature limit results from the reactivity of container materials (see Table 1) and from

[a] References denoted as [A.1] etc. refer to citations given in Appendix A, etc.

the upper pressure limit for Knudsen effusion. For transpiration mass spectrometry, the corresponding limits are ≈1800 K and 1 bar. In earlier work, we extended these limits with the development of Laser-assisted Vaporization Mass Spectrometry (LVMS) to ≥ 4000 K and ≈ 1 bar [A.3]. With this technique, some sacrifice in precision was necessary as temperature measurement was based on an indirect gasdynamics-based approach. Also, pressure determination relied on use of a secondary calibration material, combined with use of not well-established ionization cross sections (see [A.19] and Appendix E). In the present work, these limitations have essentially been avoided and the improved LVMS method tested to at least 5000 K and 20 bar. Thus the applicable measurement regime of the classical KMS approach has been extended by about a factor of two in temperature and a factor of 10^5 in pressure. The precision of partial pressure determinations has also been significantly improved, typically by factors of 2 to 10, as considered in detail in Appendix E.

The following discussion: (a) provides an overview of the LVMS technique in its present form and (b) emphasizes concepts or data not given elsewhere or in the Appendices.

2. Approach

The various key elements and improvements made in the LVMS technique are summarized as follows. A scale diagram of the facility is given by Fig. 1 (see also Fig. 1, Appendix A). Various types of pumping and operating vacuum pressures are indicated for each of the four differentially pumped stages. A lens-focused laser beam impacting a target for sample heating is depicted in stage I. Vaporization, expansion, rate monitoring, and molecular beam formation also take place in stage I. Mass spectrometric (MS) analysis is carried out in Stage IV using a mutually perpendicular configuration for the molecular, electron, and ion beams. Additional experimental detail may be found in [A.3].

2.1 Sample heating and containment

In Appendix A and in [A.3] we considered in detail the selection and application of short (≈20 ns) laser pulses to provide a spatially, temporally contained heated sample, usually in liquid form. As discussed in Appendices A and B, a high speed ICCD camera is used to measure the dimensions, in addition to the form of the temperature distribution and temperature-time dependence of the hot spot. An example of the time-dependence of temperature and total pressure (P_t) of a thermally pulsed material is given in Fig. 2. Here, the absolute pressure and temperature scales were derived from deposition rate measurements. The relative temperature (T) is given by the integrated light emission intensity (I) relation: $T \alpha I^{0.24}$ for the wavelength range of the CCD detector ($\lambda \approx 185$ nm to 1100 nm). Within the 5 ns uncertainty limit of the effective hot spot time (typically 25 ns) as utilized in eq. (4), Appendix A, the vapor pressure falls to a negligible level as may be seen in Fig. 2..

It can be shown, theoretically, that the time for a sample to reach maximum temperature is negligible compared with the laser pulse times used here. This is confirmed by our observation of thermal emission pulse profiles similar to that of the laser pulse.

2.2 Creation of a thermally equilibrated vapor and extraction of a representative sample

A key issue with the use of very short laser pulses as a heat source is the establishment and verification of a localized thermal equilibrium system. Experimental data are found to obey equilibrium-based laws such as the Maxwell velocity distribution (see Appendix, Fig. C.3 and loc. cit.) and the Planck radiation model (see Appendix, Fig. A.3). At the very high temperatures and pressures involved, significant kinetic barriers to equilibration are unlikely.

To obtain a representative vapor sample, in the form of a molecular beam, the vapor plume must expand to a collisionless condition on a shorter time scale than that for gas kinetic reactions, dimerization or other homogeneous nucleation reactions to occur to a significant degree. For the conditions of the present studies, no evidence of aggregate species or perturbed chemical equilibria was found (see Appendix A and [A.3]). A coupled chemical kinetic-gas dynamic model of the Al_2O_3 system indicated no significant shift in equilibria on the time scale (20-30 ns) of the thermal pulse (see model curves in the Appendix, Fig. B.11). Use of longer laser pulses (ms) and elevated background pressures is known to lead to significant non-equilibrium vapor processes [A.9].

2.3 Temperature measurement

2.3.1 Indirect methods

Indirect methods of determining temperature during LVMS experiments have been developed and discussed in detail elsewhere [A.3] and in Appendices B, C, and D. The main approach relies on a well-characterized isentropic expansion process where the pre- and post-expansion temperatures (and pressures) are related by a gasdynamic factor. In Appendix B, Fig. 9 provides a test of this relationship. Beam temperatures, as given in Fig. B.9, are obtained from measured Maxwell-Boltzmann velocity distribution, e.g. as in Fig. C.3, or from related time-of-arrival measurements, e.g. as in Fig. C.4. Details of this approach may be found in Appendix D. The experimentally determined gasdynamic characteristics have also been validated by Monte Carlo simulations [A.15]. A secondary approach to temperature measurement is the use of temperature-sensitive known chemical equilibria [A.3, A.27].

2.3.2 Direct method

Development and application of a direct temperature measurement method is discussed in Appendix A. The method relies upon rapid (5 ns), spectrally resolved monitoring of surface thermal emission with good spatial discrimination. An optical spectrometer, equipped with an intensified photodiode array detector, is used for this purpose. Provided the material behaves either as a grey or black body emitter, the Planck radiation law may be used to determine temperature. A good fit to the Planck law of emission intensity over a range of wavelengths also provides additional support for the presence of thermal equilibration and the absence of a significant wavelength-dependent emissivity. Figure A.3 (see also Fig. 8, below) shows typical data fits.

Analysis of integrated light emission intensity profiles across the dimensions of the hot spot indicated a temperature difference between the center and the measured edge of $\approx$ 10 %. The spectrometrically measured temperature is an effective value between

that of the center maximum and the cooler edge. Through simulations of summed Planck distributions for a typical spatial temperature profile, the effective temperature was typically determined to be about 50 K less than the maximum. From the exponential dependence of P_t on T, this temperature difference leads to too high a P_t value by ≤ 10 %. These P, T differences can be compensated for but are within experimental uncertainty.

Temperature measurement for some systems requires use of line filters or other measures to suppress interference from spectral emission (e.g. from Al over Al_2O_3) or absorption (e.g. from B and C_2) and from sample fluorescence (e.g. with AlN) and frequency doubling of the laser beam (e.g. with $BaTiO_3$).

2.4 Total pressure measurement

In Appendix A, we discuss a basically real-time approach to determining total pressure based on the use of a conventional deposition rate monitor (see also Fig. 1). A related approach has been used in the past, although infrequently, with KMS studies (e.g. see p.18 [A.18]. However, for the present application, the cos θ vapor distribution necessarily present under KMS conditions becomes $\cos^n \theta$, $n > 1$, for the gasdynamic flow conditions of LVMS. As shown in Appendix A, values of $n \approx 3$ to 12 are typical and this affects appreciably the conversion of deposition rate to pressure (see eq. 4, Appendix A). Methods developed for measurement of n are given below in sections 2.6 and 2.7. Using the measured n values, together with the derived relationship between P_t and rate (eq. (4) Appendix A) total pressures of relatively well known systems such as alumina (Fig. 4 below), graphite (Fig. A.4) and boron (Fig. 7 below) were reproduced.

Deposition rates, and hence pressures, are controlled by laser fluence, as shown for example in Fig. 3. It should be noted that the apparent deposition rates given in the figure are from actual rate monitor readings where the actual heating time (≈ 20 Hz x 25 ns) is much smaller than the nominal time displayed by the rate monitor. Hence the actual rates (e.g. as used in eq. 4 Appendix A and in Table 2) are higher than the apparent rates by a factor of $\approx 2 \times 10^6$. Rates are observed that correspond to pressures as high as hundreds of bars, which is in the region of the critical point. However, temperature measurement limitations, plasma effects, and other non-thermal perturbations appear to limit the practical upper pressure for thermochemical studies to ≤ 20 bar, depending on the material system.

2.5 Partial pressure measurement

When all pertinent species have been identified, the partial (p_i) and total pressures are related by:

$$\Sigma\, p_i = P_t\,.$$

Each partial pressure is further related to the species ionization cross section, σ_i according to:

$$p_i \sim (\sigma_i)^{-1}.$$

Methods of obtaining σ_i have been discussed in detail elsewhere [A.19]. In standard reference data publications, σ_i uncertainties of $\delta \approx 150$ % are estimated [A.2]. In Appendix E, known and previously estimated σ_i data are evaluated and we show that even larger uncertainties are possible. A new model is given whereby the uncertainties are reduced to 30 %.

In some cases, measurement of σ_i is possible using the LVMS technique, as shown in Appendix A. For such studies, we relied on the use of laser heating fluences significantly larger than those used for thermochemical studies. Under these conditions, chemical analysis of vapor deposits indicates a stoichiometric transport of target material, from which cross section ratios of vapor components may be fixed. Alternatively, a similar approach can be used during thermochemical studies provided independent composition analyses of the condensate are carried out.

When measuring p_i by LVMS, the inherent cooling of the expansion process (see Appendix C) can in some, but not all, instances lead to a beneficial reduction of the extent of electron impact fragmentation. This effect reduces uncertainties in assigning ion intensity signals to individual species and improves the accuracy of p_i determination.

In Fig. 4 we present a comparison of p_i and P_t results with the JANAF – NIST reference data [A.1] for the Al_2O_3 system. These results supersede those given earlier (Appendix B). The experimental and reference results agree to within the combined uncertainties. The most significant differences are: a higher O experimental partial pressure, which appears to be a characteristic of oxides for these experimental conditions, and a lower Al_2O experimental value.

2.6 Determination of hydrodynamic flow vapor density distributions ($\cos^n \theta$) using a kinematic deposition rate monitor

The relationship between deposition rate and source pressure depends on the distribution $\cos^n \theta$. In order to measure this distribution, a commercial deposition rate monitor was mounted on an adjustable positioning arm (see Fig. 1). With this device, the rate monitor could be swept across the impinging plume at specified θ. Fig. 2, Appendix A shows a typical result where the rates closely follow the ideal $\cos^n \theta$ distribution, which is consistent with a non-perturbed free-jet expansion process.

2.7 Determination of hydrodynamic flow vapor density distributions ($\cos^n \theta$) using spectroscopic reflectometry film thickness profiling

As an alternative approach to that using a rate monitor, the measurement of film thickness by conventional spectroscopic reflectometry was investigated. In this approach the variation in the reflectivity as a function of wavelength, due to thin film interference, is used to map the film thickness distribution. Fig. 5 shows typical film thickness distributions for two different hot spot diameters. The n values agree with those obtained using the rate monitor and with a Knudsen layer theory, as shown in Fig. 6. The theory requires some experimental input, however, in order to set the Knudsen layer thickness.

3. Results

3.1 Boron liquid vapor pressure measurements at 3700 K to 4300 K

Reference data vapor pressures for liquid boron are based on measurements made over the solid (mpt. ~ 2348 K) with the results extrapolated using calculated and estimated thermodynamic functions [A.1, A.2]. The extrapolated pressures are estimated (in [A.2]) to be accurate to within a factor of two. In an earlier LVMS study [A.4], the vapor pressure of B(ℓ) was determined (at 2800 K) using BN as a source of B(ℓ) according to the thermal decomposition process:

$$BN = B(\ell) + \tfrac{1}{2} N_2 \quad . \qquad (1)$$

The accuracy of this original study was limited by the use of lower precision indirect temperature measurements ($\delta \pm 300$ K) and by too low a value of the B atom ionization cross section (see discussion in Appendix E and [A.19]).

With the recent improvements in the LVMS technique, we have reinvestigated reaction (1). Table 2 and Fig. 7 indicate the P_t vs. T results. The P_t results depend on $M^{-0.5}$ where M is the concentration-weighted average molecular weight for B and B_2. The relative concentrations (partial pressures) of B_2/B were determined from the mass spectrometric ion intensities and appropriate ionization cross sections (Appendix E). Temperatures were obtained from Planck distribution fits as given in Fig. 8.

The P_t results (Fig. 7) are found to be in good accord with the reference data [A.2]. On the basis of data point number 4, one could speculate that the literature curve should be more nearly linear. However, the two sets of data are within the combined uncertainties. This overall agreement supports the literature extrapolation procedure used [A.2], as well as providing a further test of the LVMS technique (in addition to those of Appendix A). The experimental scatter is somewhat higher than from similar studies on other materials (C, Al_2O_3 , Y_2O_3) which may be due to the indirect and transient means used to produce boron liquid, coupled with an inefficient and time-dependent coupling of the laser radiation with BN and B(ℓ).

3.2 Comparisons with literature

In Appendix A, LVMS total and partial pressure results are compared with the extrapolated literature values. For the most part, good agreement is found, as may be seen in Fig. 9 for total pressure results. An indication of the relatively low uncertainty limits for the LVMS data is also given in Fig. 9. The estimated uncertainties are typically: T ($\pm$ 1 %), P_t ($\pm$ 25 %), p_i ($\pm$ 40 %). These uncertainties lead to reaction enthalpy uncertainties of ~ 3 kJ $mole^{-1}$. Critically evaluated literature data uncertainties [A.1, A.2] are typically 300 % for P_t and an additional 150 % for p_i. More significant differences may be expected with partial pressure comparisons. As shown in Appendix A (Table 2), the C_5 partial pressure is a notable example.

4. Conclusions

Limitations in classical high temperature mass spectrometry with respect to the upper ranges of temperature and pressure, in addition to the accuracy of partial pressures, have been largely removed. Figure 10 exemplifies the extended coverage provided by LVMS. The uncertainties associated with literature extrapolations and with LVMS results are also indicated in Fig. 10. It should be noted that the graphite example used for Fig. 10 is one of the most well-characterized literature systems and that uncertainties for other materials can be far greater.

A particular aspect of LVMS that can be limiting is the coupling of laser energy with the target surface. This coupling is dependent on surface morphology and target density, as well as the intrinsic optical properties of the target material. Only a narrow range of laser fluences is suitable for controlled vaporization with minimal laser-vapor plasma forming interaction. Also, at elevated laser fluence, ejection of liquid droplets can occur, particularly for metal targets. For the present studies, this problem has been avoided.

In summary, measurement of P_t , p_i , T data by LVMS requires accurate knowledge and control of:

(a) target material stoichiometry and morphology,
(b) laser pulse time and energy,
(c) effects of laser wavelength and fluence on system equilibration,
(d) optical multichannel analyzer wavelength sensitivity,
(e) optical interferences to Planck radiation behavior, including spectral emission and absorption together with target fluorescence, and wavelength-dependent emissivity,
(f) non-thermal or non-equilibrium events, including target ejection of particulates and cluster formation during vapor expansion and cooling,
(g) laser interaction with the initial stage of vapor formation, leading to excess production of ions with plasma-enhanced energies, and to photodissociation of molecular species,
(h) hot spot dimensions and temperature distribution across the spot,
(i) temperature-time profile during vaporization,
(j) calibration of oscillating crystal deposition rate monitor,
(k) velocity distributions,
(l) electron impact ionization pathways and cross sections, including autoionization,
(m) vapor spatial distribution, i.e. $\cos^n \theta$, and
(n) system sensitivity to molecular weight, including effects of gas-dynamic mass separation and quadrupole mass filter discrimination.

Further discussion of these factors may be found in the attached Appendices and the literature cited therein.

Acknowledgements

It is a pleasure to recognize the following colleagues for their assistance over the years with various aspects of laser vaporization mass spectrometry: Drs. Albert Paul, Matthew Joseph, and Jacob Yeheskel, together with Mr. Art Sessoms.

Table 1. High temperature characteristics for representative ceramic materials

Material	m.pt. (K)	b.pt. (K)	Vapor species
ZrO_2	2950	4320	ZrO, ZrO_2, O, Zr
Y_2O_3	≈2800	4170	YO, O, YO_2, Y
HfO_2	3173	4100	HfO, HfO_2, O, Hf
Al_2O_3	2327	3950	AlO, Al_2O, Al, O, Al_2O_2
SiO_2	1996	3000	SiO, SiO_2 , O, Si
MgO	3105	3700	Mg, O, MgO
B_2O_3	723	2320	B_2O_3 , BO, BO_2 , B_2O
$BaTiO_3$	1890	≈4700	BaO, Ba, TiO, TiO_2 , Ti, O
UO_2	3140	3800	UO_2 , UO, UO_3 , U, O
C	---	4100	C_3, C_1, C_2, C_4, C_5, C_6, ...
SiC	2400-3100?	3300	Si, SiC, Si_2C, SiC_2
BN	---	4080	B, B_2, N, N_2, BN
AlN	---	2800	Al, N, N_2, AlN
Conventional container materials			
W	3680	>6000	Form stable oxides, hence reducing to other oxide materials
Ta	3258	5778	

Table 2. Pressure versus temperature data for B(ℓ)

Point no.	Rate cm/s[a]	P_t (bar)[b]	T (K)	$\pm \delta$ T (K)[c]
1	0.017	0.1	3660	15
2	0.038	0.24	3870	10
3	0.043	0.27	4000	50
4	0.31	2.0	4220	80
5	0.044	0.28	3800	60
6	0.03	0.2	3700	90

Footnotes to Table 2:

a. Obtained from deposition rate monitor apparent rates, adjusted to actual accumulated hot spot times for 20 Hz pulse frequency and a 25 ns effective hot spot time per pulse.
b. See Appendix A for definition of the following terms:
$a = 1.13 \times 10^{-2}$ cm^2, $n = 11.7$, $M = 11$, $\ell = 3.03$ cm, $\rho_B = 2.54$ gm cm^{-3}.
c. δ T statistical $\approx \pm$ 10 K, δ T given is from average of several runs, estimated actual δ T $\geq \pm$ 50 K.

Figure Captions

1. Scale diagram of LVMS apparatus showing a cross section view.

2. Thermal pulse profile of temperature and pressure measured with ICCD camera and deposition rate monitor, respectively.

3. Apparent deposition rate, expressed as film thickness (nm), and P_t dependence on laser fluence (λ = 1064 nm) for $BaTiO_3$ with a 0.02 cm^2 hot spot area.

4. Total and partial pressures over liquid Al_2O_3 ; upper scale is temperature (K), lower scale is reciprocal temperature (K^{-1}).

5. Film thickness spatial distributions (data symbols) and $\cos^n \theta$ dependences (curves fitted to n values) from optical reflectrometry for a Y_2O_3 target.

6. Comparison of n (from $\cos^n \theta$) experimental and model values for various spot diameters. Model curve is calculated from the following expression developed by J.C.S. Kools, E. van de Riet, J. Dieleman, Appl. Surf. Sci. 69 (1993) 133:
$$n = 3.9\,[1 + 2(Z_o/x)^{1.2}]^{0.75}\,(x/Z_o)^{1.2},$$
where x is spot diameter and Z_o is Knudsen layer thickness. Data points are labeled for the various systems measured. The YO points (from vaporization of Y_2O_3) are from reflectometry and the C and Si points are from rate monitor scans.

7. Measured P_t , T values (open circles) for boron species over liquid boron. Uncertainties are indicated by the error bars. Solid curve is from the IVTANTERMO data evaluation of [A.2] and broken curves are uncertainty limits of [A.2]. Data points, as given in Table 2, are numbered chronologically.

8. Measured optical spectrometer intensity versus wavelength curves, corresponding to the numbered data points of Fig. 7. The thicker smooth curves are for the Planck temperature fits.

9. Difference and uncertainty comparisons between LVMS (P_{obs}) and literature (P_{thermo}) P_t data for the indicated material systems. Data points labeled Am and Ack are from [A.32] and [A.31], respectively. The bars indicate uncertainty limits.

10. Comparison of P – T ranges (solid curves) for KMS (curve at $\leq$ 2800 K) and LVMS (curve at 3000 K to 5000 K) using graphite as an example. The broken curve indicates the upper limit uncertainty for the literature data [A.1] and the dashed curve for the LVMS technique. The bullet statements indicate limiting factors to the temperature and pressure ranges and to their accuracy, as discussed in the main text.

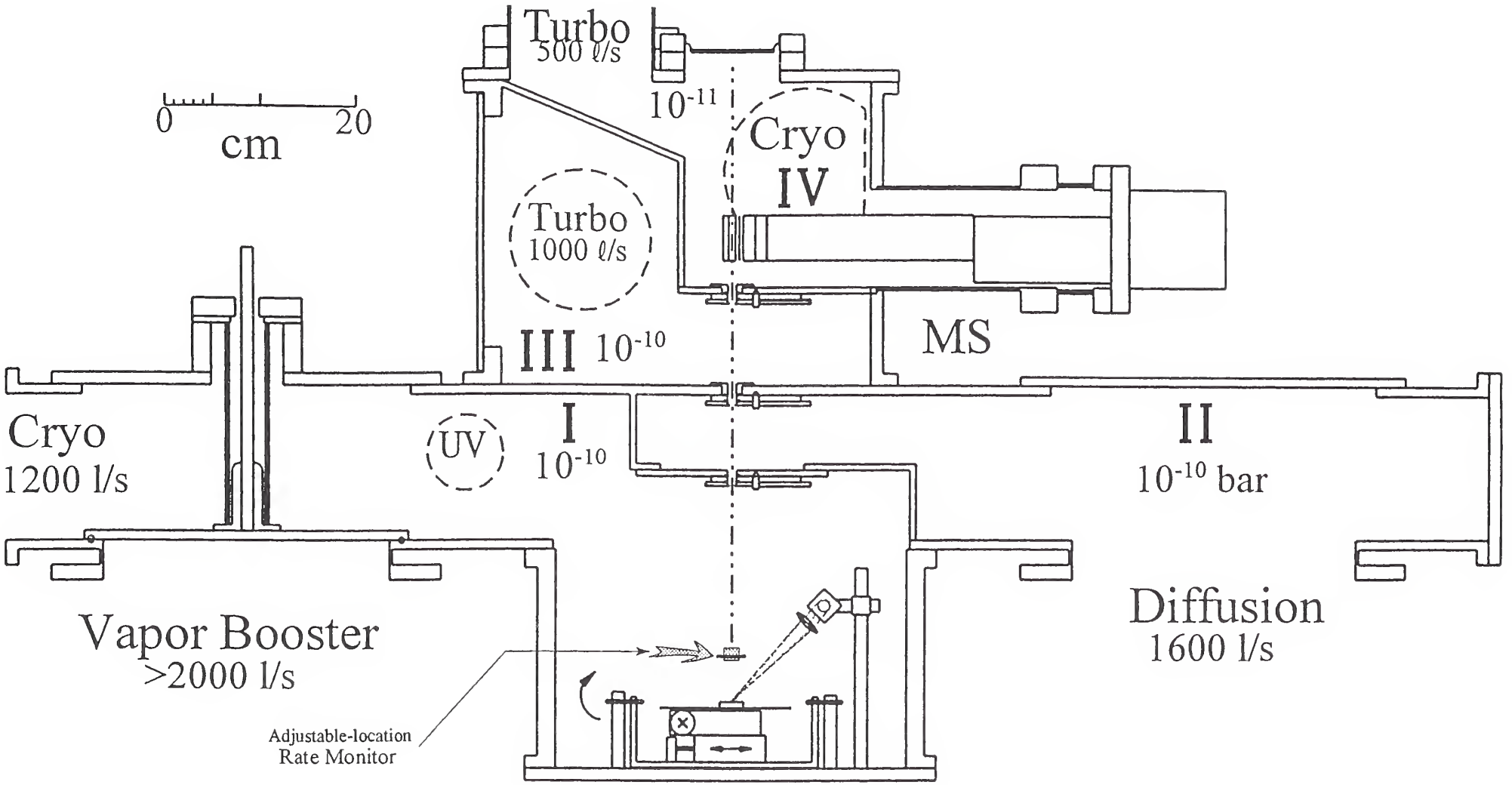
Turbo
500 ℓ/s
10-11
Cryo
IV
0
20
cm
Turbo
1000 ℓ/s
III 10-10
MS
Cryo
1200 l/s
UV
I
10-10
II
10-10 bar
Vapor Booster
>2000 l/s
Diffusion
1600 l/s
Adjustable-location
Rate Monitor

Figure 1

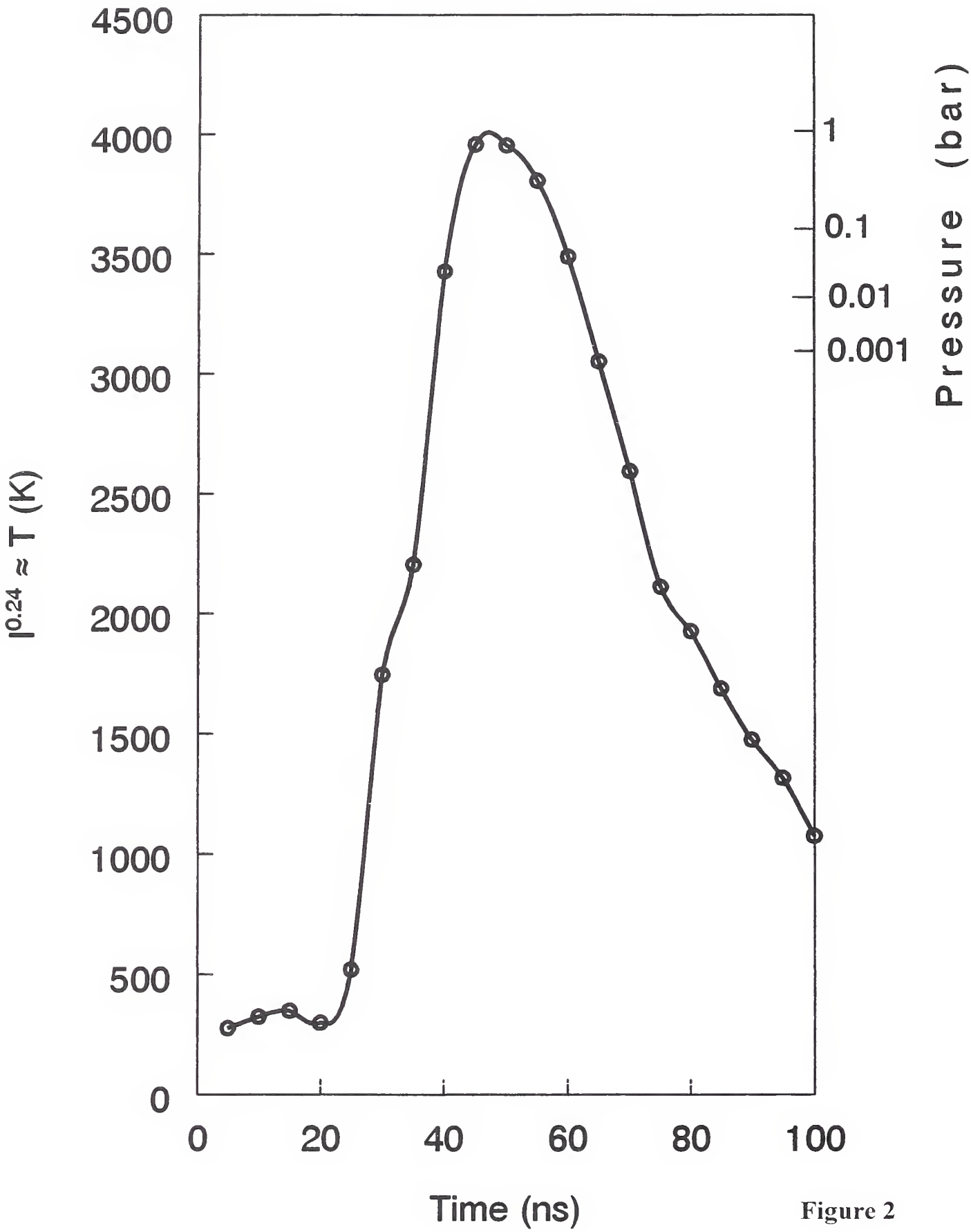
4500
4000
3500
3000
2500
2000
1500
1000
500
0
0
20
40
60
80
100
Time (ns)
I^0.24 ≈ T (K)
1
0.1
0.01
0.001
Pressure (bar)

Figure 2

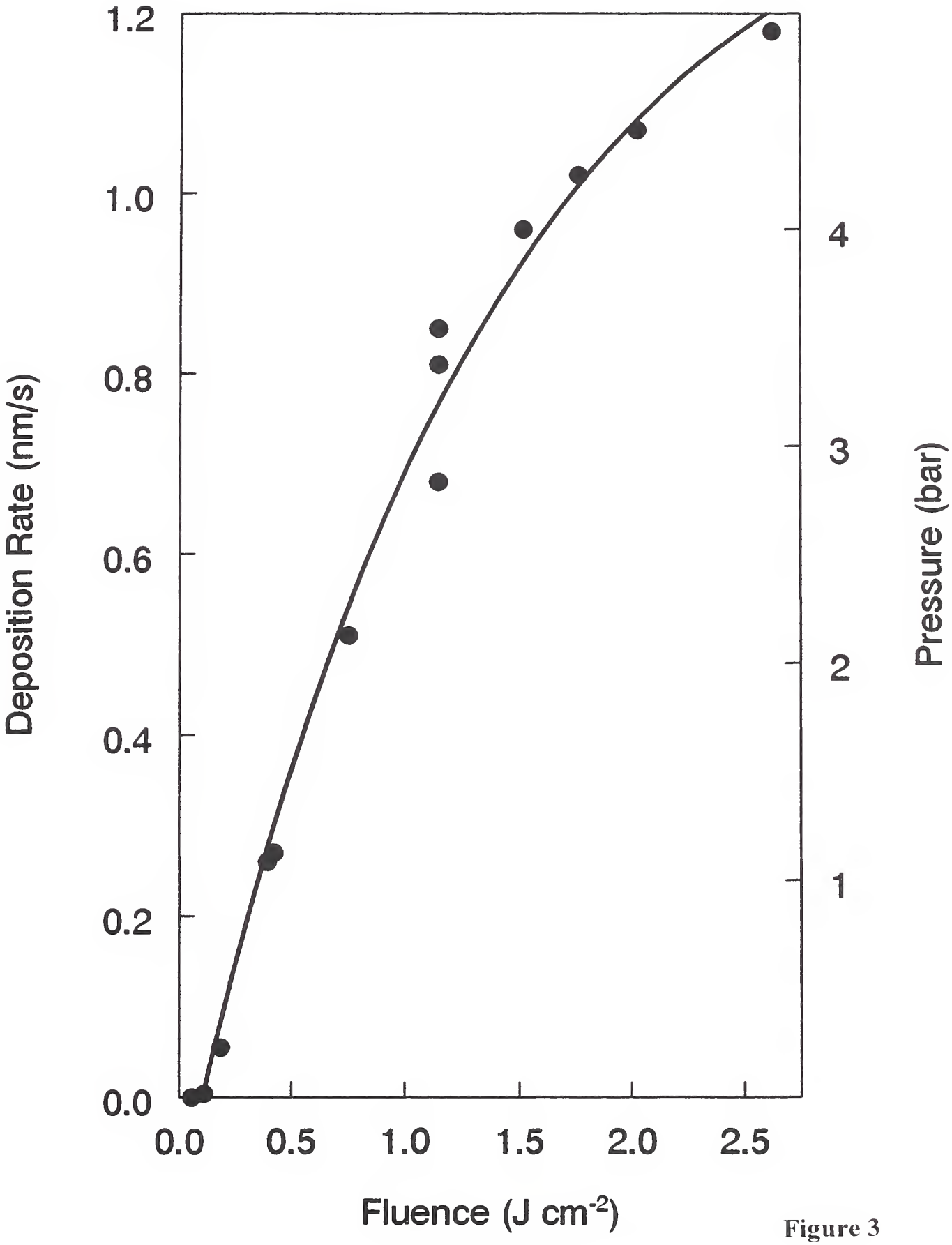
Deposition Rate (nm/s)
Pressure (bar)
Fluence (J cm-2)
0.0
0.2
0.4
0.6
0.8
1.0
1.2
1
2
3
4
0.0
0.5
1.0
1.5
2.0
2.5

Figure 3

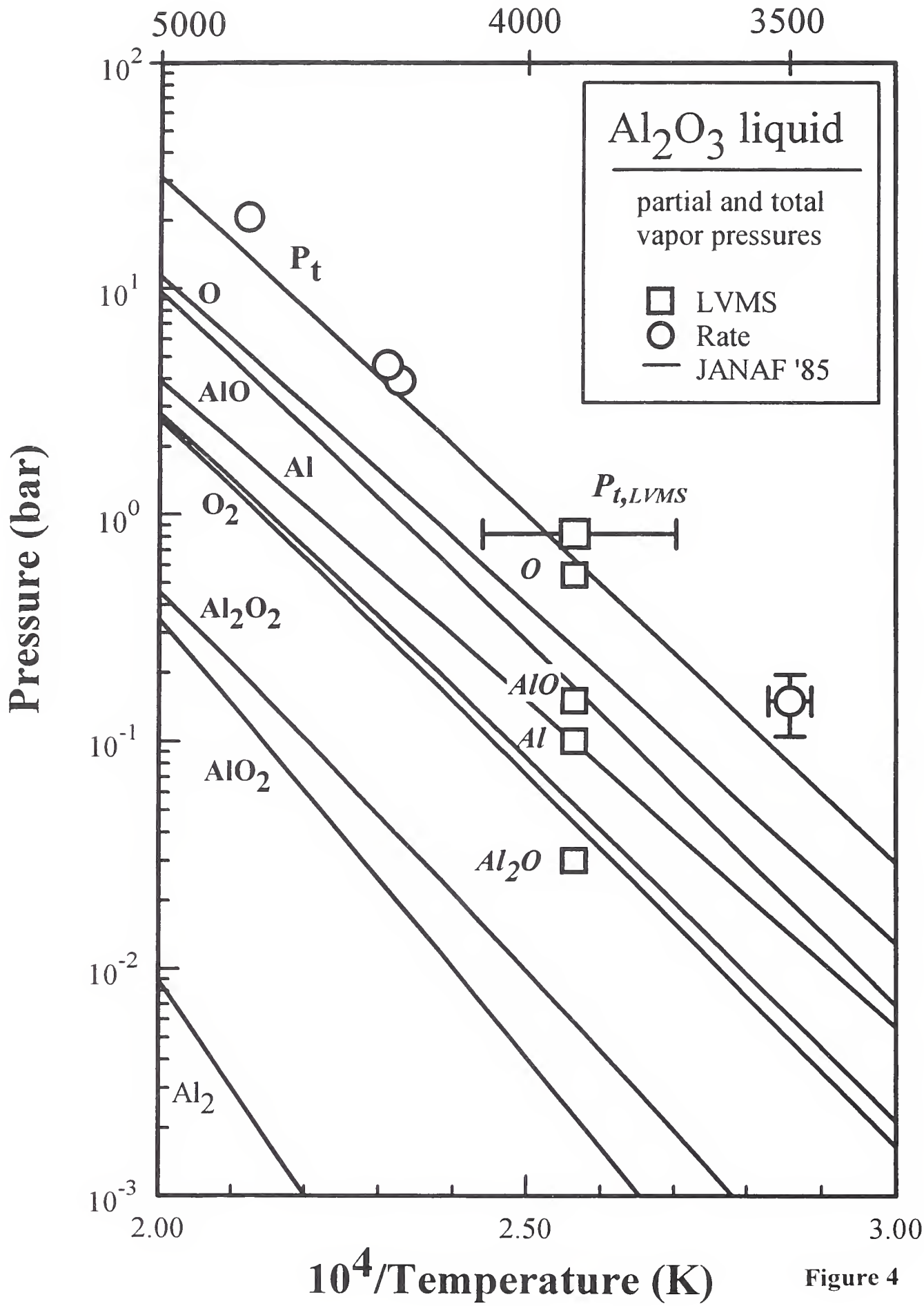
5000
4000
3500
10^2
10^1
10^0
10^{-1}
10^{-2}
10^{-3}
Pressure (bar)
Al_2O_3 liquid
partial and total vapor pressures
LVMS
Rate
JANAF '85
P_t
O
AlO
Al
O_2
Al_2O_2
AlO_2
Al_2
$P_{t,LVMS}$
O
AlO
Al
Al_2O
2.00
2.50
3.00
10^4/Temperature (K)

Figure 4

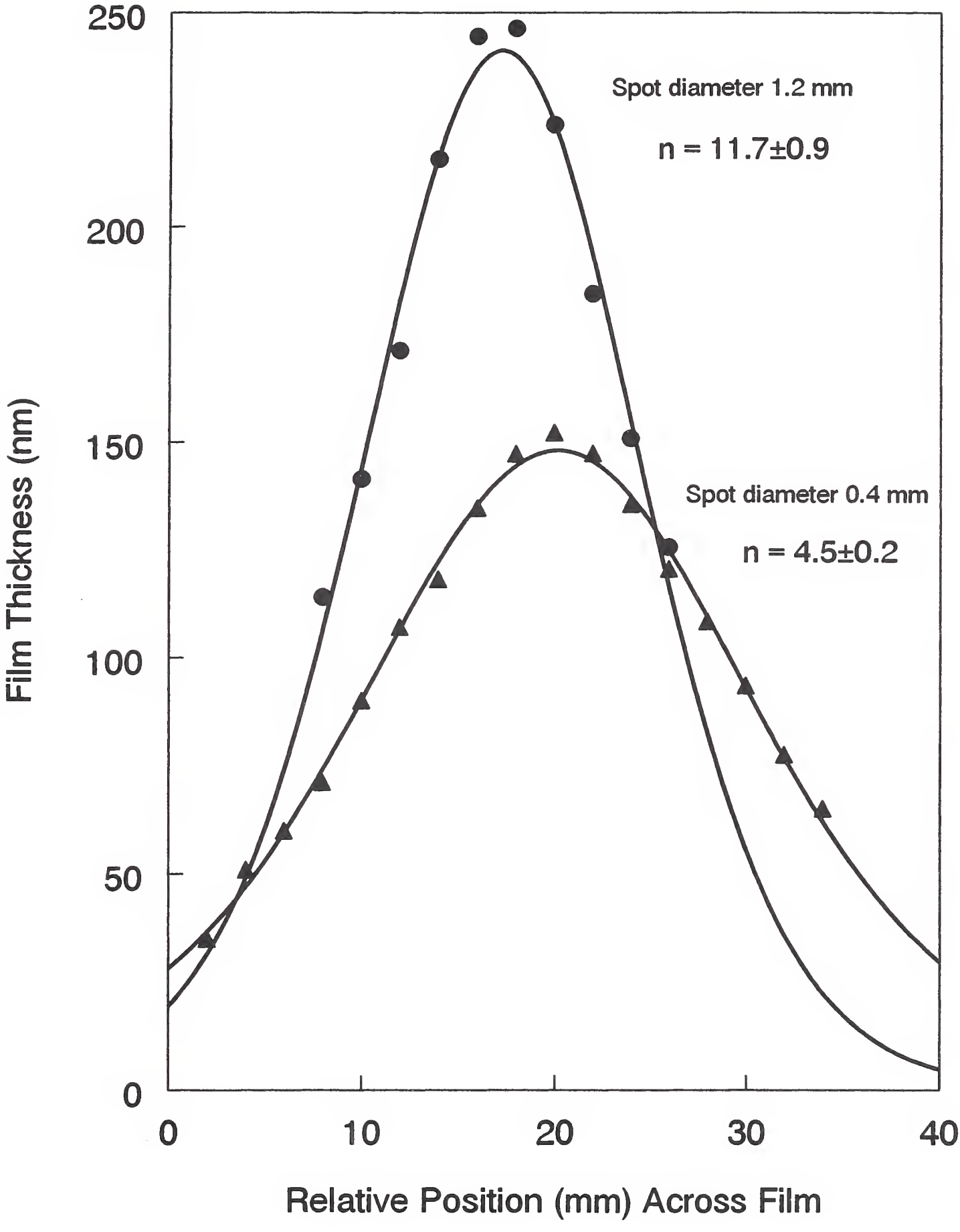
250
200
150
100
50
0
Film Thickness (nm)
Spot diameter 1.2 mm
n = 11.7±0.9
Spot diameter 0.4 mm
n = 4.5±0.2
0
10
20
30
40
Relative Position (mm) Across Film

Figure 5

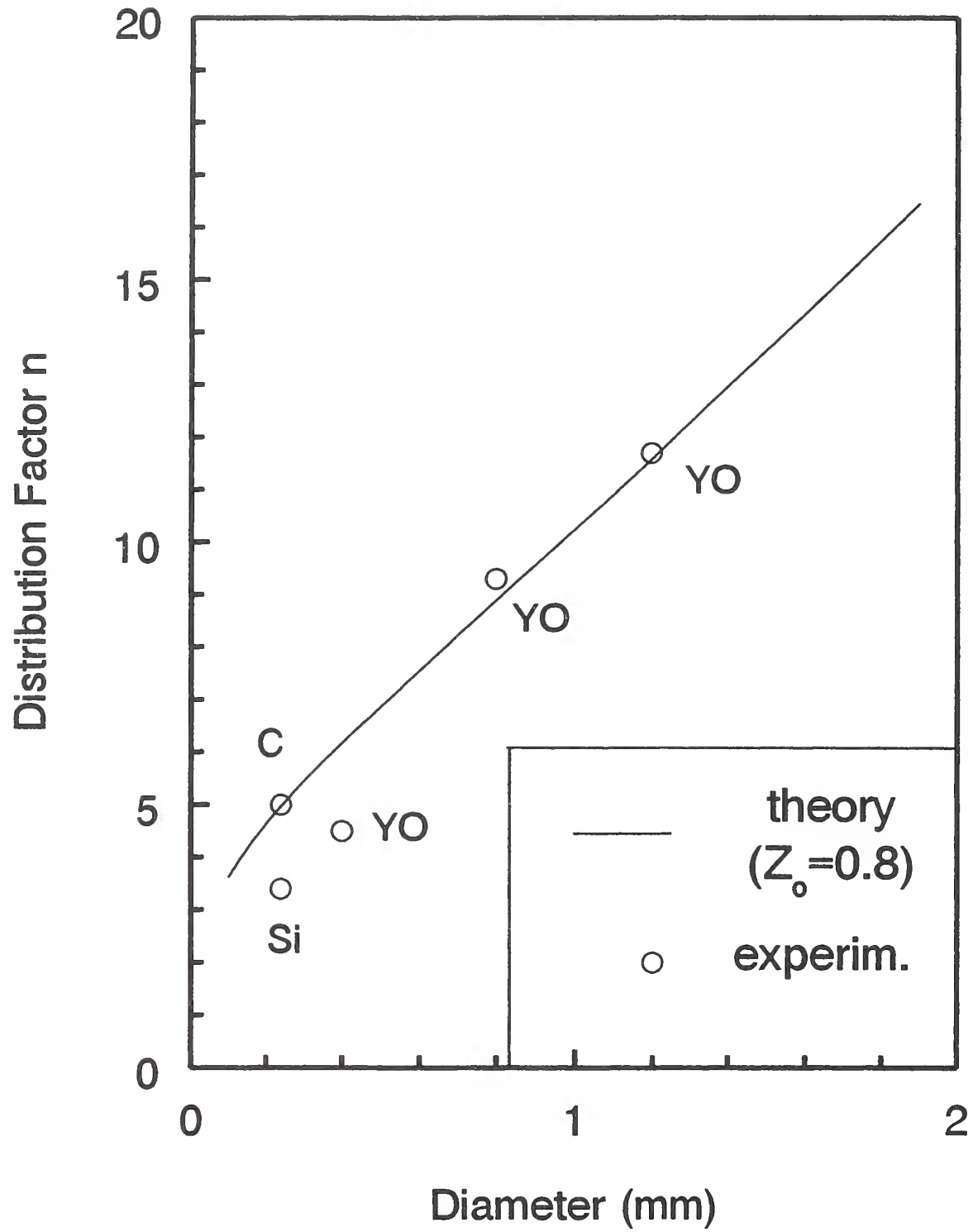
20
15
10
5
0
0
1
2
Distribution Factor n
Diameter (mm)
C
YO
YO
YO
Si
theory
(Z$_o$=0.8)
experim.

Figure 6

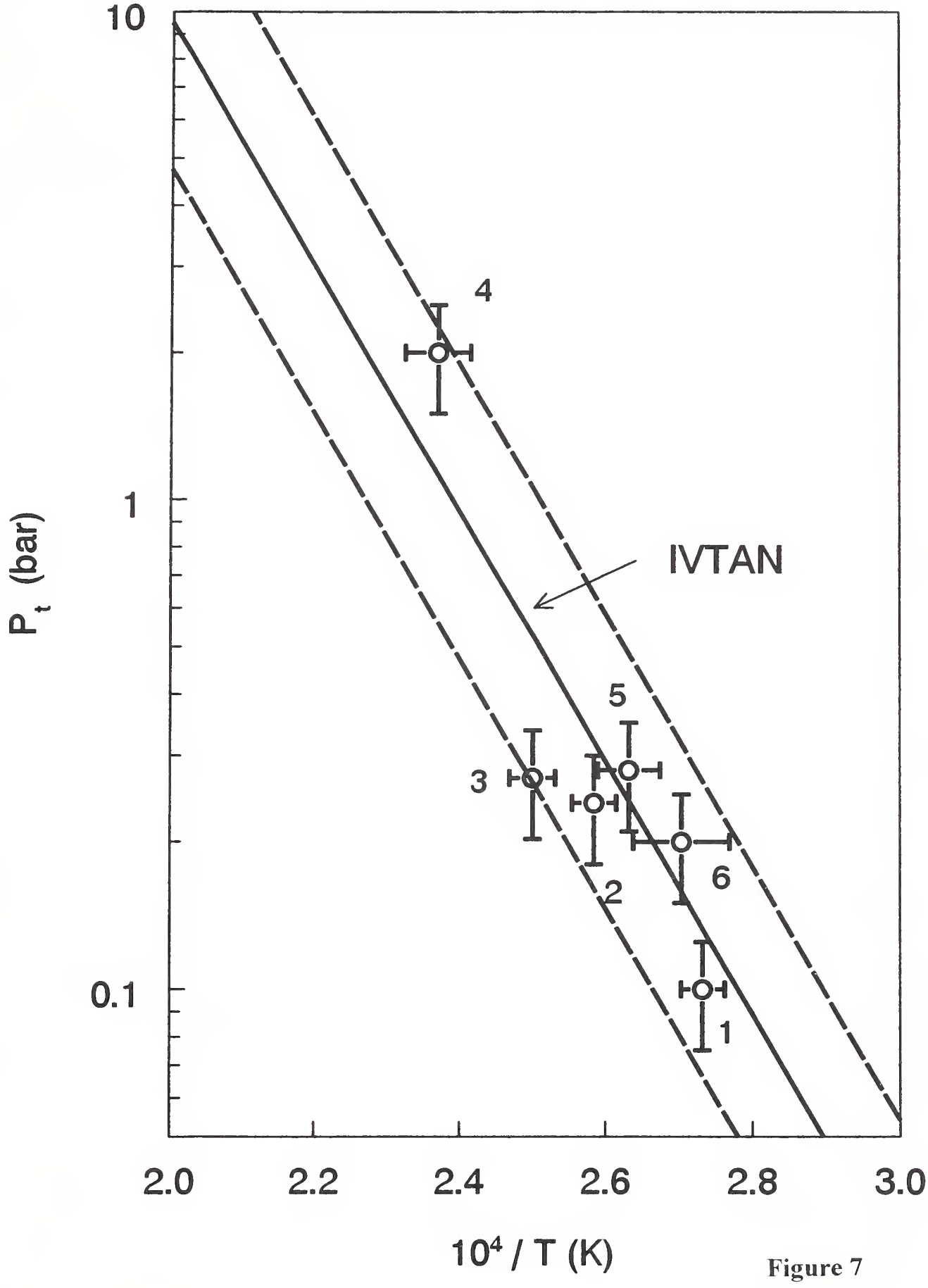

Figure 7

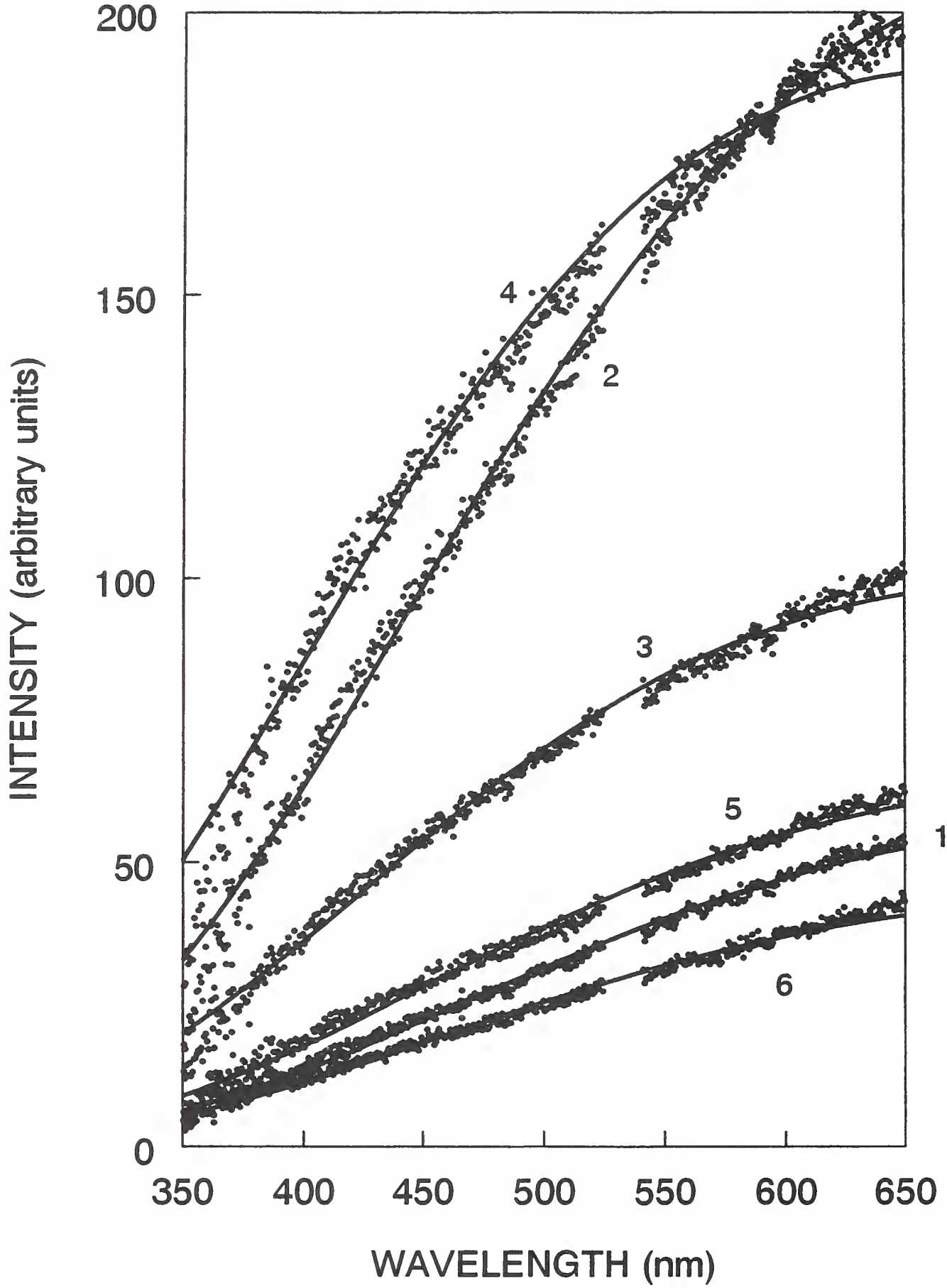
200
150
100
50
0
INTENSITY (arbitrary units)
350
400
450
500
550
600
650
WAVELENGTH (nm)
4
2
3
5
1
6

Figure 8

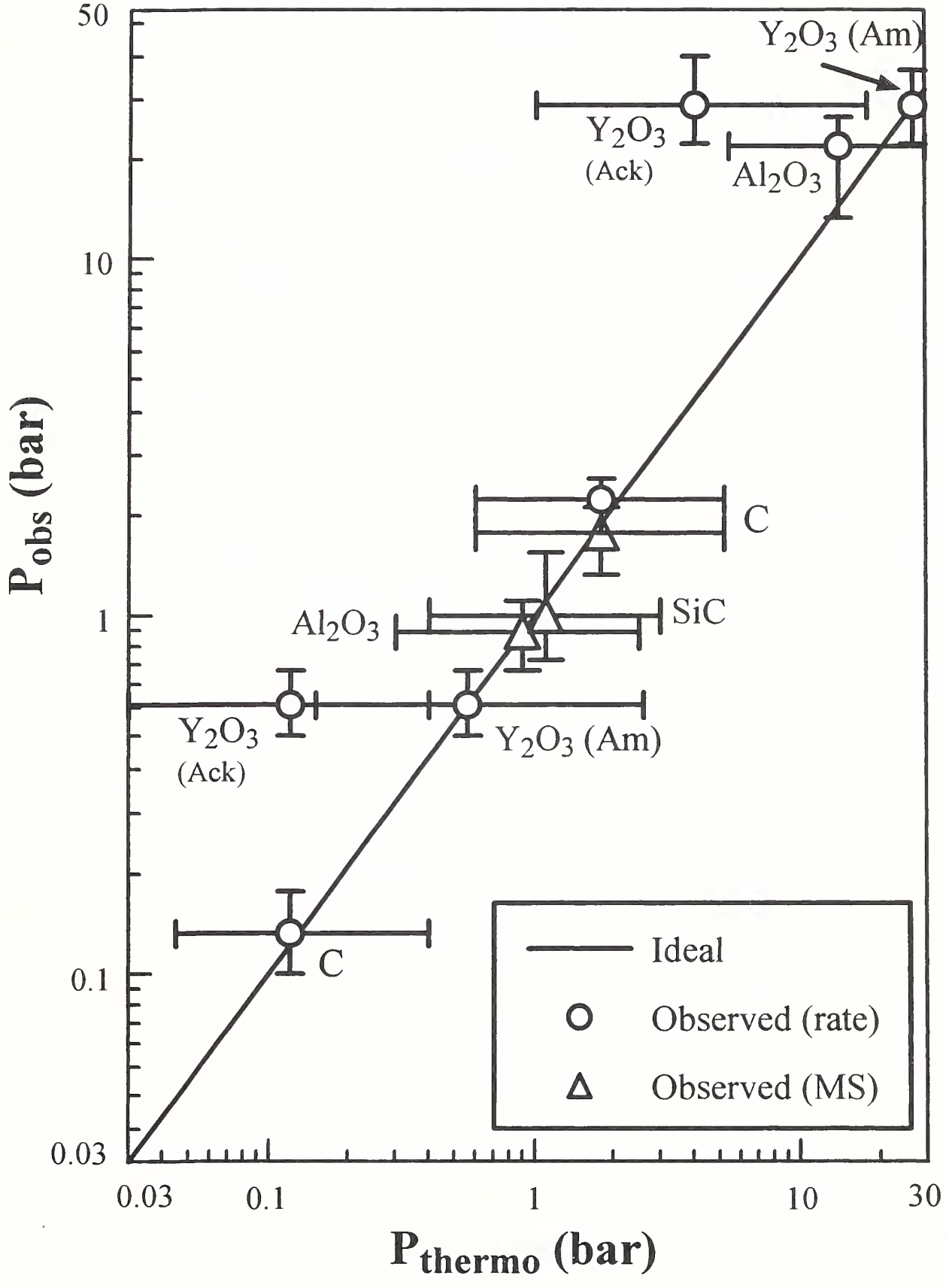
50
10
1
0.1
0.03
0.03
0.1
1
10
30
P_{obs} (bar)
P_{thermo} (bar)
Y_2O_3 (Am)
Y_2O_3 (Ack)
Al_2O_3
C
Al_2O_3
SiC
Y_2O_3 (Ack)
Y_2O_3 (Am)
C
Ideal
Observed (rate)
Observed (MS)

Figure 9

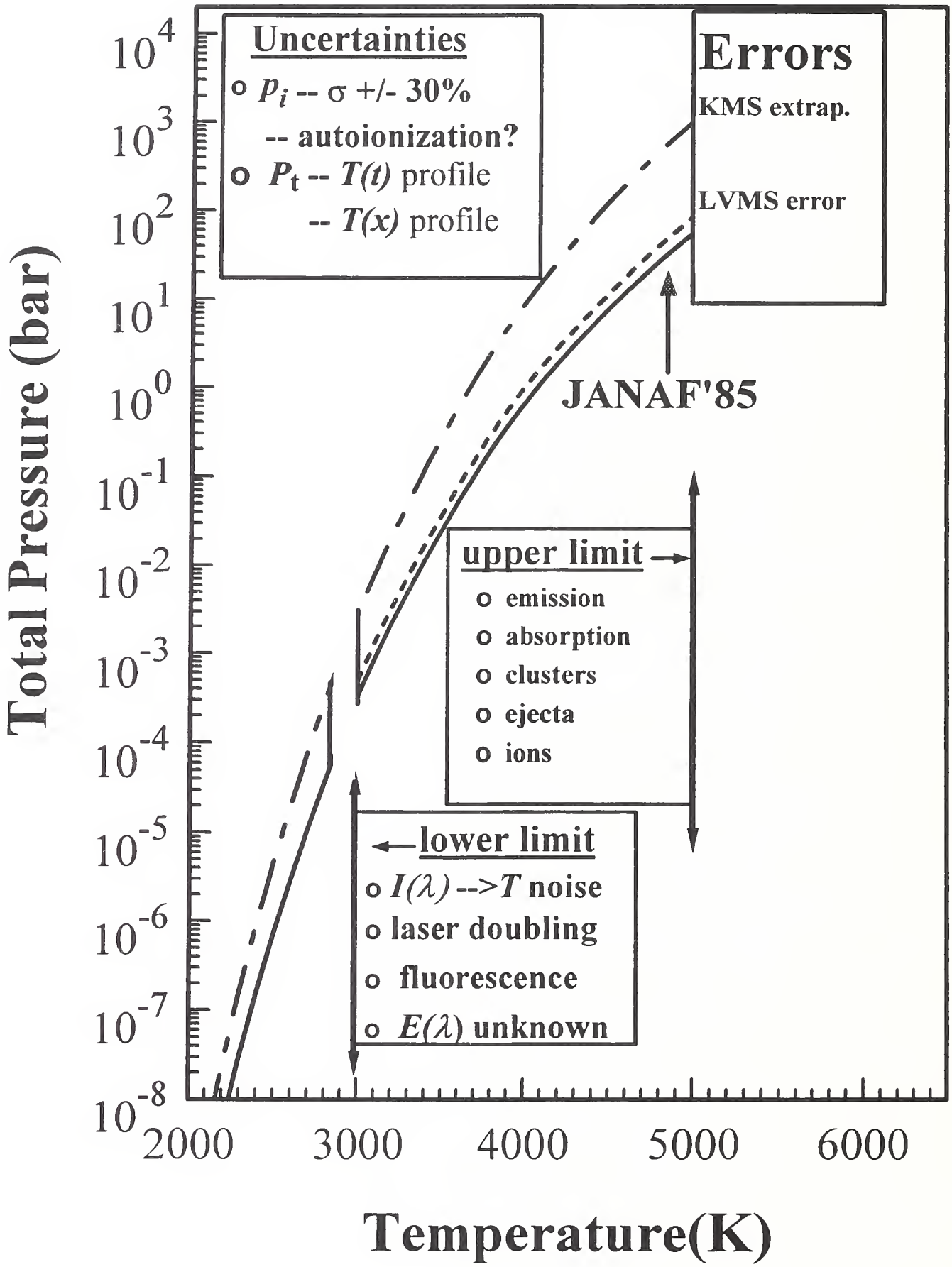
Uncertainties
o p_i -- σ +/- 30%
-- autoionization?
o P_t -- $T(t)$ profile
-- $T(x)$ profile
Errors
KMS extrap.
LVMS error
JANAF'85
upper limit
o emission
o absorption
o clusters
o ejecta
o ions
lower limit
o $I(\lambda)$ -->T noise
o laser doubling
o fluorescence
o $E(\lambda)$ unknown
Total Pressure (bar)
10^4
10^3
10^2
10^1
10^0
10^{-1}
10^{-2}
10^{-3}
10^{-4}
10^{-5}
10^{-6}
10^{-7}
10^{-8}
2000
3000
4000
5000
6000
Temperature(K)

Figure 10

APPENDIX A

Pure Appl. Chem., Vol. 72, No. 11, pp. 2111–2126, 2000.

Development and application of very high temperature mass spectrometry. Vapor pressure determinations over liquid refractories*

J. W. Hastie†, D. W. Bonnell, and P. K. Schenck

National Institute of Standards and Technology (NIST), Gaithersburg, Maryland 20899-8522, USA

Abstract: Existing thermodynamic and vaporization data for liquid refractories are based either on estimates or on data extrapolated from studies on the solids obtained at much lower temperatures. Previously, we have shown that pulsed laser heating, coupled with time-dependent mass spectrometry of the free-expansion vapor plume, can be used for semi-quantitative measurements of vaporization thermochemistry. The present work extends this approach with the development of (a) more direct, and more accurate, methods for determining the system temperature and pressure; (b) improved experimental and theoretical determinations of key parameters such as ionization cross sections; and (c) improved characterization of the gas dynamic expansion and thermal equilibration processes. Example material systems considered include C, SiC, Al_2O_3, ZrO_2–7%Y_2O_3, and Y_2O_3 at temperatures and total pressures typically in the range of 3000 to 5000 K and 0.01 to 10 bar, respectively (1 bar = 10^5 Nm^{-2}).

INTRODUCTION

The thermodynamic properties of inorganic materials at very high temperatures, and hence at high vapor pressures, are often required for processing or performance assessment. Examples of current technologies include those based on plasma spray of liquid particles and on electron beam and laser vaporization of liquid pools. The long-standing need for more accurate thermochemical data for nuclear reactor materials at very high temperatures continues. In the present context, we consider very high temperatures to include the range 2500 to 5500 K. The lower limit corresponds, approximately, to the practical upper limit of classical high-temperature thermochemistry techniques, particularly Knudsen effusion mass spectrometry (KMS). The upper limit is somewhat arbitrary but allows for inclusion of refractory liquids at vapor pressures up to at least 10 bar and without thermal ionization as a major contributor to the vapor composition. For this temperature range, thermochemical data, including partial pressures, are generally based on an extrapolation of data obtained from studies at much lower temperatures or from estimation procedures. Thus, thermochemical data presented in critically evaluated thermochemical reference tables (JANAF [1], IVTANTHERMO [2]) have significant uncertainty, which could be even greater than expected in the very high temperature range.

Because of the impracticality of containing reactive liquids and vapors at temperatures much beyond 2500 K, an essentially containerless approach, developed earlier, has been used [3,4]. This approach utilizes short time-scale (~20 ns) laser pulses as a directed, spatially constrained heat source as discussed in earlier work (see refs. 4, 5, and cited literature). An additional measurement complexity arises from the propensity of high-temperature materials to vaporize as a mixture of complex and simple species, with the former often increasing in importance with temperature [6]. In order to speci-

*Lecture presented at the 10th International Conference on High Temperature Materials Chemistry (HTMC-X), Jülich, Germany, 10–14 April 2000. Other presentations are published in this issue, pp. 2101–2186.

†Corresponding author;

fy the vapor molecular weight (e.g,. for use in mass transport–pressure relationships), the identity and relative concentrations of these species must first be established. Mass spectrometry (MS) is the most practical (if not the only) means of obtaining such information, and MS has been coupled with pulsed lasers to provide a technique we term laser vaporization mass spectrometry (LVMS). A distinction should be made between LVMS and other, nonthermal laser-MS coupled experiments such as laser microprobe mass analysis (LAMMA) and pulsed laser deposition (PLD) monitoring [7]. In these latter cases, highly nonthermal processes are present, and little or no thermochemical insight is usually gained under the higher laser powers utilized. Even for LVMS experiments, a serious high pressure limit arises from laser–vapor interaction, giving rise to nonthermal effects such as superheating, electronic excitation, and photo-dissociation. As these effects are readily identified, they can usually be avoided by adjusting the laser parameters of wavelength, fluence, and pulse width. Nonthermal modes of laser–solid (or liquid) interaction can also occur, particularly with shorter wavelengths, shorter pulses, or higher fluences.

The use of pulsed laser heating for vaporization thermochemistry studies has had a sporadic history over a period of about three decades. The early work of the groups of Ohse [8] and Olander [9] utilized relatively long pulse (~μs to ms) infrared lasers. A few non-mass spectrometric experiments were also carried out, e.g., by Covington *et al.* [10] and Tunney *et al.* [11]). In our laboratory, the technique was modified to include use of much shorter laser pulses [3]. Experimental difficulties and data accuracy limitations were present with each of these early studies. Accurate conversion of mass spectral ion intensities to partial pressures suffered from the need to measure, or calculate, gas dynamic factors not present in conventional KMS. In addition, the usual KMS limitations of electron impact fragmentation and unknown ionization cross-sections were also present. Temperature measurements were also difficult, relying on two-color pyrometry and assumed emissivity for longer pulse experiments and on indirect thermochemical and gas dynamic approaches for the short-pulse experiments. In the present study, these limitations have been overcome, and the accuracy of vapor pressure data is typically at least an order-of-magnitude better than the extrapolated/estimated literature data.

Olander recently reviewed and compared the general features of short- and long-pulse laser materials interaction for thermal vaporization measurements [9]. Advantages and disadvantages exist with each case. With the latter, a practical upper limit vapor density occurs with the onset of expansion nucleation and clustering. This onset is apparently very material-specific and can occur at pressures as low as ~10^{-4} bar for the case of UO_2. A similar restriction was found for ZrO_2 [9]. With the former short-pulse case, nonthermal interactions are more likely. However, these can usually be avoided or minimized for select conditions of laser wavelength, and for fluences not too far above the vaporization threshold. Also, no evidence has yet been found for a cluster-forming limitation, and total vapor pressures typically in the range ~0.01 bar to ~10 bar have been measured in the present study. This pressure range is characteristic for vaporization of liquid refractories, whereas at temperatures corresponding to pressures of 10^{-4} bar, such materials are usually solids. Hence, short-pulse lasers are the most appropriate choice for thermodynamic studies of liquid refractories or other materials at temperatures where vapor pressures are of the order of 1 bar. However, the short time-scale (typically 5 to 30 ns) associated with these lasers significantly increases the experimental difficulties, particularly the direct measurement of temperature. Also, the hydrodynamic nature of the pre-sampling vapor expansion process necessitates the use of special calibration procedures to convert mass spectral signals, or alternatively, deposition rates, to partial and total pressures. The necessity of demonstrating thermal vaporization on a case by case basis is also a special requirement of the present LVMS technique. In the current study, we have measured species partial and total pressures for several of the more well-established systems (i.e., C and Al_2O_3), in order to test the reliability of the lower temperature data and of the extrapolation procedures. Measurements have also been made on less well-established systems (i.e., SiC, Y_2O_3, and ZrO_2–7%Y_2O_3). These particular systems are present as high vapor pressure liquids in industrial physical vapor deposition and thermal spray processes. The SiC system, unlike C and Al_2O_3, may not vaporize congruently and melts by disproportionation to Si(ℓ) and C(s,solution) [12]. This

vaporization mode provides an additional test of the LVMS technique, where congruent vaporization can occur under nonthermal ablation conditions, such as are used for PLD; observation of noncongruent behavior would then be more consistent with a thermal rather than ablative process. Also, the presence of a Si(ℓ) phase allows one to use the well-established pressure data for Si(ℓ) to test the reliability of the LVMS measured pressures of Si and Si_2.

APPARATUS

In our earlier studies we described the basic apparatus used for short-pulse LVMS [4]. A schematic of this apparatus, including various modifications made for the present work, is given in Fig 1. The essential features of this apparatus are:

- high-power pulsed laser sources, with optics to control the beam diameter and angle of attack at the target surface. Lasers used include: (a) Nd:YAG, with wavelengths of 1064 nm and 532 nm; and (b) excimer at 248 nm. Other wavelengths available with these lasers were not used for these studies. Pulse widths were typically ~20 ns (Nd:YAG) and 10 ns (excimer).
- computer-controlled target-support x-y stage. The high-speed motion of the stage was programmed to assure a fresh target area was used with successive laser pulses. The stage could also be tilted *in situ* when necessary.
- deposition rate monitor, positioned 3 cm from target at $\theta = 0°$ and with remote positioning control to allow removal from the beam axis during MS detection and for angular distribution ($\cos^n \theta$, where $n \geq 1$) measurements. The rate and MS measurements are made sequentially, under essentially identical conditions.

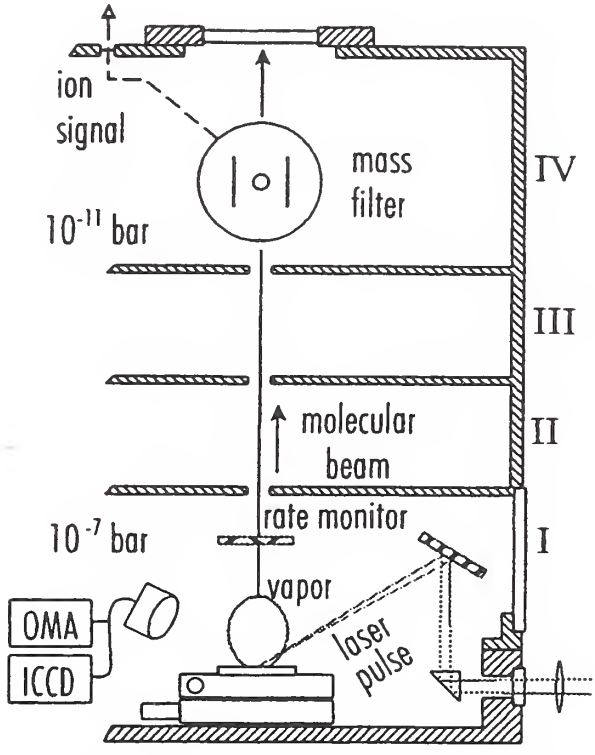

Fig. 1 Schematic of LVMS apparatus, together with *in situ* deposition rate monitor and OMA, ICCD optical detectors.

- four differentially pumped vacuum stages. For continuous beam calibration experiments [e.g., see ref. 5, a chopping wheel (not shown) was positioned in stage III (see Fig. 1)].
- a quadrupole mass filter, positioned in stage IV with a cross-beam electron impact ionizer. The distance of the ionizer from the target was nominally 47.4 ± 0.3 cm (targets were repeatedly positioned within ±0.05 cm). This separation allowed for relatively unrestricted high-speed pumping in all stages; it also provided for a time delay (relative to the laser pulse onset) suitable for time-of-flight measurements with good mass and velocity discrimination.
- both digital (pulse counting) and analog multichannel detection of mass spectral ion intensity signals. Use of digital detection avoided the need to consider multiplier mass and species-type discrimination factors usually coupled with the measurement or use of ionization cross sections.
- optical multichannel analyzer (OMA) spectrometer for monitoring light emission over the range λ = 185 nm to 1100 nm at successive times, with 5 ns time resolution. These data were used to reveal the presence of spectral emissions from vapor species that are usually indicative of the onset of laser–vapor plume interaction. By fitting the intensity-wavelength dependence to a Planck radiation function, the target hot spot temperature could be obtained, in addition to the cooling rate. These measurements were typically made simultaneously with deposition rate measurements.
- intensified charge-coupled device (ICCD) camera capable of 5 ns time resolution gating, which yielded data on the dimensions of the hot spot and relative temperatures. In addition, the onset of a visible laser-excited plume or the ejection of particulates could also be monitored with this device.

APPROACH

The general experimental and data analysis approach is as follows, with the discussion giving emphasis to those aspects not described elsewhere.

Laser-induced vaporization

In recent years we, and many others, have utilized laser materials interaction for the processing of thin films or coatings [13]. The usual requirement of a stoichiometric transport of target material to a substrate necessitates use of relatively short λ photons with sufficiently high fluence (energy density E, J cm^{-2}) to produce a high energy (~50 eV) luminous plasma with nonthermal properties. With LVMS, avoiding the onset of any laser–plume interaction is desirable, in so far as possible. In general, this condition requires use of a relatively low fluence near the threshold for detectable vaporization. Use of longer λ laser radiation (e.g., 1064 nm vs. 248 nm) also reduces the contribution of nonthermal interactions at the target. But, if the fluence is too far above threshold then inverse Bremstrahlung and other laser–vapor interactions can occur more readily at longer λ. The ideal fluence and λ conditions are specific to each target material and, to a lesser extent, its prepared density and microstructure. With increasing fluence, the transition from thermal vaporization to plasma formation and ablation can readily be monitored with a fast-gated ICCD camera (as increased light emission) or with the deposition rate monitor (as markedly increased rate of deposition). The dependence of deposition (and hence vaporization) rate on laser fluence was generally determined in order to identify the threshold for a markedly increased dependence where the onset of a luminous plasma was noted. The pressures were determined from rate measurements, and LVMS experiments were usually carried out below the plasma onset fluence. The mass spectrometer signals also reveal plasma effects in the form of additional, faster time-of-arrival (TOA) profiles (see below) and an increased abundance of ions not formed by electron impact in the MS ionizer.

Vapor expansion and beam formation

We have considered the vapor expansion-beam formation process in some detail elsewhere [14]. Monte-carlo [15,16], hydrodynamic flow [16], and chemical kinetic [5] models, together with ICCD imaging [17] and MS determination of velocity distributions [16], have indicated the essential features of this process. Basically, under the conditions used for LVMS, the vapor expands isentropically, and simple relationships exist between the pre- and post-expansion properties of temperature and pressure. The expansion to an effectively collisionless state is also sufficiently rapid (~100 ns) that the chemical composition of the pre-expansion vapor is essentially unchanged [5]. A collision-free vapor stream forms within a few mm of the target surface and is collimated to give a directed molecular beam by an aperture between stages I and II (see Fig. 1).

Mass spectral analysis

The mass spectral analysis procedure is similar to that for KMS, as is the relationship between partial pressure (p_i) and the ion intensity (I_i) produced by electron impact of species i:

$$p_i \simeq k_i I_i T_s \quad , \tag{1}$$

where T_s is the vapor temperature at the target prior to expansion and k_i a constant that contains factors dependent on species identity. Ionizing electron energies of 26 ± 0.5 eV (corrected for the MS work function using known species appearance potentials) were generally used, with checks being made at lower energies for cases where species fragmentation may be significant. At this nominal energy, fragmentation interference was generally found to be insignificant (for expansion-cooled beams) and, from appearance potential curves and model considerations, ionization cross-sections were expected to be near their maximum values. Routine determinations of the MS intensity-time profiles (TOA) and, in some cases, appearance potential curves, were used to monitor the possible contribution of electron impact fragmentation to the MS-selected ion signals. In practice it is desirable to sum I_i over the entire time-of-arrival peak of the molecular beam at the MS ionizer (i.e., I_i becomes the area of the time-of-arrival thermal intensity-time profile after base-line subtraction). The constant k_i can be expressed as

$$k_i = k \,/\, (\sigma_i S_i) \quad , \tag{2}$$

where k is an instrument geometry/sensitivity constant valid for all species; σ_i (discussed below) is the ionization cross-section; S_i contains quadrupole and multiplier, together with hydrodynamic beam-forming, dependencies on molecular weight. S_i is determined using a standard gas mixture, in the form of a hydrodynamic beam, as described elsewhere [18]. In contrast to KMS, where the vapor angular distribution is nominally $\cos\theta$, k also depends on the exponent n in the $\cos^n\theta$ distribution of the vapor plume, where n is typically in the range $4 \leq n \leq 20$ for the laser spot size and vapor pressures used in the present studies.

Several independent approaches are used for k determination. Materials with relatively well-established partial pressures may be used together with eqs. 1 and 2. For instance, we have used NaCl(ℓ), B(ℓ) (from BN), Si(ℓ) (from SiC), and C(s) for this purpose. A potentially more accurate approach, developed in the present study, is to determine total pressures from deposition rates, as discussed below, *in situ* with the mass spectrometric experiments. Thus, uncertainties associated with literature thermochemical data are avoided. In this study we compare results obtained by both approaches.

Ionization cross-sections

The significance of ionization cross-sections (σ) to high-temperature mass spectrometry has recently been considered in detail elsewhere [19]. In the present study, σ's for the elements were either those

measured by Freund *et al.* [20] or most often the calculated values of Mann [21]. In the absence of experimental values for the molecules encountered here we used a model described in detail elsewhere [22]. This predictive model has been shown to reproduce known experimental values, with the possible exception of one or two cases where autoionization, not accounted for by the model, may have been present. Notably, the model σ's for closed-shell electron configuration molecules are relatively low compared to other species or other estimates. We find, however, that such values are supported in these studies by equilibrium constant measurements, for example, for:

$$M + O_2 = MO + O,$$

where M = Mg, Ba, and by stoichiometric tests. For instance, from a stoichiometric (as confirmed by deposit analysis) vaporization of $BaTiO_3$, where BaO and TiO were the major MS-determined vapor species, we determined $\sigma(BaO) = 1.7 \pm 0.35$ ($\times 10^{-16}$ cm^2) at 26 eV. The model value is calculated as $2.0 \pm 0.6 \times 10^{-16}$ cm^2. Summation of element σ's, used in some estimations (e.g., as in ref. 1), would give a value of 18.6×10^{-16} cm^2.

The model is based on the viewpoint that heteronuclear high-temperature species generally are ionically rather than covalently bonded [23]. The model has the form

$$\sigma \simeq N/I_v \quad , \tag{3}$$

where I_v is the vertical ionization potential, either measured by MS or calculated using a coulombic model [24]; N is an *effective* number of electrons contributing to the ionization process. Values of N are obtained from the ionic bond assignment where in $M^+ X^-$, for example, values of N for M^+ or X^- are taken from the isoelectronic elements whose N's are obtained from the above equation using known σ's and I_v's.

Deposition rates

Deposition rate measurements were used to obtain values of n for the $\cos n\theta$ distribution of species in the expanded vapor and also to obtain values of total pressure (i.e., the aggregate of partial pressures). $\cos^n\theta$ distributions have been confirmed by two approaches. In addition, the values (given below) obtained by both approaches are consistent with values obtained earlier from a hydrodynamic model, from ICCD imaging (e.g., see ref. 16) and from MS-stage tilting angular distribution experiments. The two principal approaches used were: (a) we utilized the rate monitor (RM) *in situ* with the MS system. The RM (mounted on a 22-cm lever arm) was moved in an arc parallel to the plane of the target surface. By fitting the data to a $\cos^p\theta$ function, values of p were obtained, as shown by the example in Fig. 2. It can be shown that for this parallel RM system geometry, values of n, appropriate to an ideal detector positioned on a spherical surface, are given by: $n = p - 3$; *(b)* a spatially resolved optical interference film thickness measurement was made across the deposited film [25]. The film deposition and RM geometries are equivalent, and similar results were obtained with both approaches.

Determination of total pressure (P_t) from deposition rate is well known for Knudsen effusion conditions. However, to our knowledge, this approach has not previously been used under hydrodynamic flow conditions, for which we derive the following relationship:

$$P_t = 10^{-6}\left(\frac{R\left(\ell^2 + r^2\right)\pi\rho}{f\Delta t A}\left[\frac{2\pi R_g T_s}{M}\right]^{0.5}\right)\left\{\frac{2}{n+1}\right\}H \tag{4}$$

where P_t is in units of bar (= 10^5 Nm^{-2}); R is the (nominal) film thickness deposition rate in cm s^{-1}, calculated from the rate monitor scale reading given in Å (1Å = 10^{-10} m) and referenced to the total laboratory accumulation time; f is the laser repetition rate in Hz (s^{-1}), typically 20 Hz—note that $R/f\Delta t$ is the actual thickness deposition rate per laser pulse; A is the measured hot spot area (cm2); ℓ is the distance

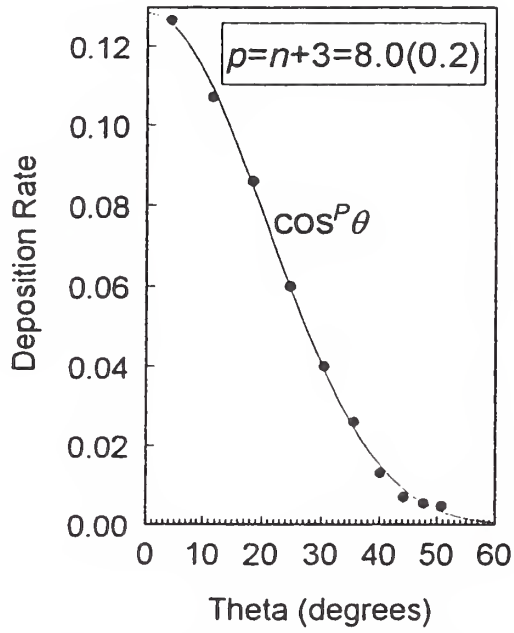

Fig. 2 Angular dependence of graphite deposition rate (symbols) fitted to a $\cos^p\theta$ ($n = p - 3$) dependence (curve).

(cm) from target to monitor, typically 3 cm here; r is the radius of the exposed area of the rate monitor crystal (cm), typically 0.4 cm; Δt is the measured effective hot spot time (s), typically 25 ns; ρ is the density (gm cm^{-3}) of the film (a nominal value used by the rate monitor to convert accumulated mass to thickness); M is the average gm-molecular weight of the depositing species; R_g is the gas constant (~8.314×10^7 erg K^{-1} mol^{-1})—the factor 10^{-6} has the units bar dyne^{-1} cm^2 (1 dyne cm^{-2} = 0.1 Pa), to convert pressure from cgs units; $H = (1 - 0.18)^{-1}$ $(2\pi/e)^{-0.5}$ and contains factors for relatively small hydrodynamic back-scattering [9] and beam-intensifying [26] effects.

It has been shown experimentally (see discussion in ref. 30) and also by model calculations that thermalization and melting occur on a time-scale shorter than 1 ns. Similarly, at the end of the laser pulse, cooling to a temperature level where the vaporization rate is negligible can be expected to occur within a few ns. In the present study, we monitored the thermal transient using the OMA and ICCD detectors and the T vs. t response, Δt, was close to that of the laser pulse duration itself (~20 ns). The laser pulse was comprised of three overlapping short pulses, effectively giving rise to a near-top-hat profile. For the materials considered here and the Nd:YAG laser used, we determined $\Delta t = 25 \pm 5$ ns to be the time that the hot spot was at its effective vaporizing temperature.

Values of P_t obtained by use of eq. 4 are considered to be accurate to ±25%. Contributing uncertainties [±percent], include A[10], R[10], n[5], M[5], Δt [20]. Other uncertainty factors, including T [1], are minimal. It is also noteworthy that the influence of σ (as $\sigma^{-0.5}$), in the determination of $M^{0.5}$, is significantly less than for the P_t method based on, for example, eq. 1, where $p_i \propto \sigma_i^{-1}$. Overall, however, the uncertainties associated with pressure determinations based on eqs. 1 and 4 are similar.

Temperature determinations

In our initial LVMS studies [4] it was not possible to measure temperature (T_s) directly on the short time scale of the laser pulse duration (~20 ns). Several indirect approaches were developed and are still used for cases where a direct approach is not possible. To reiterate, the indirect approaches are: (a) comparison of measured (LVMS) with known equilibrium reaction constants (K_p) e.g. for C_5/C_3 over C(s) and Si_2/Si over Si(ℓ); (b) use of pressures obtained from the deposition rate data, together with literature

P-T data; and (c) use of an established [5] direct relationship between T_s and beam temperature (T_b) obtained from velocity distributions or from time-of-arrival (TOA) versus $M^{1/2}$ dependancies. These approaches lead to temperatures (T_s) that appear to be accurate to better than about 3%.

In this study we have also used a more direct approach (see Apparatus section) based on the Planck radiation expression:

$$I(\lambda, T_s) = A\lambda^{-5} / \left[e^{\frac{c_2}{\lambda T_s}} - 1 \right] \tag{5}$$

where A is a fitted intensity (I) scale factor, and contains factors for both emissivity and optical losses; c_2 is the second radiation constant (= 1.438786×10^7 nm·K); A and T_s are the nonlinear fitting parameters. Data obtained by this approach are believed to be accurate to ±1%, depending on the material system. Statistical uncertainties are typically only ±5 K. Additional uncertainty arises from the presence of a temperature distribution across the hot spot. The observed temperature is then an effective ("average") value, weighted towards the maximum. As the observed vaporization time is also an effective average, uncertainties arising from the distribution of temperature and rate with the thermal pulse time and across the hot spot tend to be self-compensating.

RESULTS AND DISCUSSION

Table 1 summarizes representative results relating to total pressure determinations. Additional results and details are given in the figures and discussion. An overall excellent agreement between pressures obtained by the LVMS and rate methods is evident in Table 1. Good agreement is also found with the selected extrapolated literature values (i.e., certain, but not all, literature values show good agreement). These results rule out the presence of any significant, unaccounted for, higher-molecular-weight cluster species, as that case would lead to much higher calculated (with noncluster M-values) P_t - rate pressures than those determined by LVMS or from literature thermodynamic functions.

Table 1 Total pressures.

System	Temperature	Total pressure (bar = 10^5 Nm^{-2})				
	K	From rate[e]	n[d]	M[h]	LVMS[e]	Literature
C(s)	4100[c]	1.8	5	33	1.2[f],1.8[g]	1.8(2)[a], 1.1(11),
	4109	2.1	11.7			1.1(12), 1.0(1),
	3602	0.13	"			all at 4100 K;
	4237	5.6	"			see also Fig. 4
SiC→Si(ℓ) C(s)	3057	0.15	11.7	31		0.16(1)
	3300[c]	1.1	3.0	31	0.6[f], 0.9[g]	1.2(1)
Al_2O_3(ℓ)	3500[c]	0.15	4[b]	27	0.08[f], 0.13[g]	0.08(1); 0.09(2)
	3900[c]	–			0.6[f], 0.9[g]	0.9(1); 0.6(2)
	4300	3.9	4.5	26		3.4(1); 4.0(2)
	4332	4.6				4.2(1); 4.5(2)
	4719	20.7				14(1); 19(2)

[a]Corrected for C_5 (see text).
[b]Estimated from n vs. spot diameter correlation (±10%).
[c]From TOA data (all other T's from Planck method).
[d]Uncertainty ±6%; for n = 11.7, spot area = 1.13×10^{-2} cm^2, for 3,4,5, = 4.9×10^{-3} cm^2, and for 4.5, = 1.3×10^{-3} cm^2.
[e]Uncertainty ±25% for rate and LVMS.
[f]Based on P_{C_3} from ref. 1.
[g]Based on revised P_{C_3} = 1.3 bar, from Table 2.
[h]Average value for temperature range, based primarily on LVMS measurements.

An example of temperature measurement using the Planck radiation approach is given in Fig. 3. Based on the good agreement between observed intensities and the Planck curve over a wide range of λ, we assume a constant emissivity ("grey body" behavior). For graphite, and the other materials studied, we find that the cooling rate follows the time dependence of the laser pulse to a good approximation.

C (graphite)

Graphite has advantages as a reference or calibration system for LVMS as it remains solid up to relatively high pressures and has been extensively studied at lower temperatures. Nevertheless, the two main critically evaluated reference tables JANAF [1] and IVTANTHERMO [2] still have small but notable differences, as we discussed in our original work on this system [4]. The latter compilation [2] is more recent, and the spectroscopically based entropy functions are given higher precision. However, the enthalpy data of both compilations are based essentially on the same experimental data, with JANAF favoring the results obtained by a second law thermodynamic approach (i.e., relative P vs T data analysis) and IVTANTHERMO favoring the third law approach (i.e., absolute P data analysis). We find that the LVMS-determined partial pressures (LVMS + Rate column in Table 2) are consistent within the stated literature uncertainties, with both the JANAF and IVTANTHERMO values. The latter tables appear to significantly overemphasize the partial pressure of C_5—using our value for this species reduces the IVTANTHERMO total pressure to a value in good agreement with the present work. Using our rate-determined P_t value to obtain k for the LVMS data yields C_n partial and total pressures that are the most consistent with the available literature results. These pressures are also consistent with the temperatures obtained from *both* the indirect and direct approaches, provided the JANAF and IVTANTHERMO P_i ratios (C_5/C_3) are adjusted for the σ's used in Table 2. Thus, for instance, the JANAF values of C_5/C_3 are increased by a factor of 1.8. In addition, use of the LVMS-rate graphite pressures for k determination leads to much better agreement among P_t's obtained by the rate and LVMS methods, separately, and with the literature values for each of the systems studied.

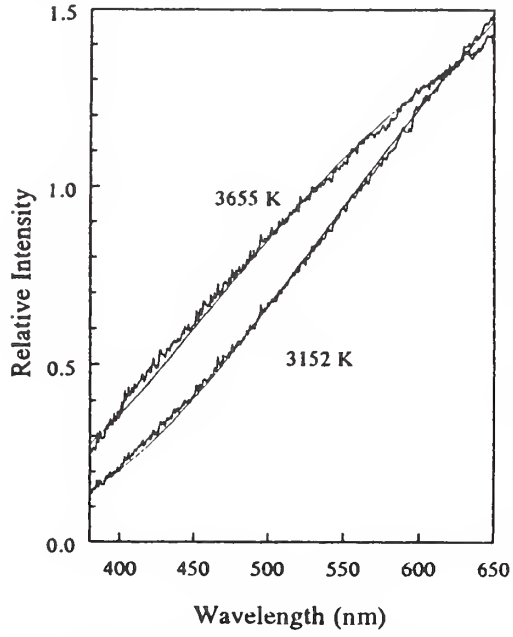

Fig. 3 Emission intensity vs. wavelength dependencies for laser-heated graphite, with two different fluences and an observation time of 100 ns; smooth curves are for Planck radiation model with T_s = 3655 K and 3152 ± 6 K.

Table 2 C(s) Partial pressures (bar = 10^5 Nm^{-2}), at 4100 K.

Species	LVMS[a]				LVMS+rate[f]	Literature	
	$I\Delta t$ (counts)	S	σ [b] ($\times 10^{-16} cm^2$)	P_i	P_i (1)	$P_i(1)$[d]	$P_i(2)$[e]
C_1	1100	0.77	1.6	0.082	0.12	0.104	0.103
C_2	3750	0.84	2.4	0.170	0.26	0.152	0.182
C_3	23420	0.88	3.0	(0.83)	1.3	0.83	1.45
C_4	940	0.94	3.6	0.025	0.04	0.11	0.050
C_5	1860	0.94	4.5	0.040	0.07	0.023	0.29
C_6	230	0.93	5.1	0.004	0.006	-	-[c]
C_7	560	0.92	5.8	0.010	0.015	-	-
C_8	35	0.88	6.5	0.0005	0.0007	-	-
C_9	230	0.80	7.2	0.003	0.0045		

[a]LVMS parameters: $k = 2.25 \times 10^{-8}$ atm K^{-1} $counts^{-1}$ t^{-1} (analog-to-digital averager), where σ units of 10^{-16} cm^2 are set to unity here and elsewhere; $n = 5$; $\lambda = 532$ nm; $E = 0.9$ J cm^{-2}.
[b]σ's; C_1 (Mann), $C_2 - C_4$ (models), $C_5 - C_9$ (est. from $C_1 - C_4$, C_{60})
[c]For $C_6 - C_9$, $\Sigma p_i \sim 0.02$ bar.
[d]Uncertainty = factor of 4.
[e]Uncertainty = factor of 3.
[f]From P_t rate (Table 1), $k = 3.37 \times 10^{-8}$ (units, see a.).

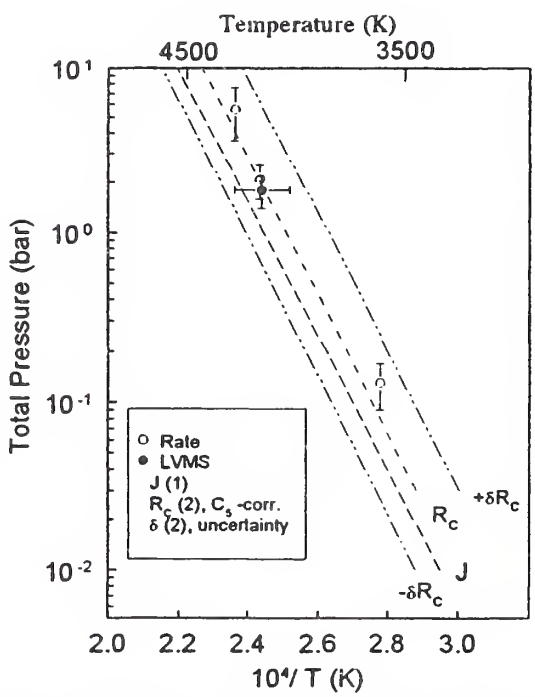

Fig. 4 Comparison of graphite LVMS and rate *P-T* data (symbols) with literature thermochemical values (curves). Size of data symbols for present work indicates experimental uncertainty.

Values of n (for $\cos^n\theta$) used for the pressure determinations based on eq. 4 are given in Table 1, and Fig. 2, above, shows a typical result, obtained using the *in situ* rate monitor. The partial and total pressure data are compared with evaluated literature values in Fig. 4 and in Tables 1 and 2.

SiC

Using similar procedures to those for graphite, *P-T* data were obtained as shown in Table 3 and Fig. 5. The indirect temperature (3300 K) was obtained by comparing T_b (from analysis of TOA data)

Table 3 SiC(ℓ,s) partial pressures (bar = 10^5 Nm^{-2}) at 3300 K.

Species	LVMS[a]				LVMS[c]	Literature[d]	
	$I\Delta t$ (counts)	S	σ ($\times 10^{-16}$ cm^2)	Pi	Pi	Pi(1)	Pi(2)
Si	100	0.88	5.1[b]	0.44	0.66	0.4	0.45
Si_2	5	0.95	5	0.02	0.03	0.02	0.06
SiC	4	0.9	4.0	0.02	0.03	0.003	0.004
Si_2C	8	0.9	4.0	0.04	0.06	0.23	0.94
SiC_2	13	0.9	3.3	0.08	0.12	0.6	1.55

[a] $k = 6.0 \times 10^{-6}$ atm K^{-1} $counts^{-1}$ t^{-1} (multichannel counter), based on P_{C_3} (1); λ = 532 nm, E = 0.9 J cm^{-2}.
[b] σ_{Si} = 6.6 (20),= 5.1 (21).
[c] Recommended values using $k = 9.0 \times 10^{-6}$ atm K^{-1} $counts^{-1}$ t^{-1}, based on revised P_{C_3} (see Table 2).
[d] For case SiC (cr,ℓ).

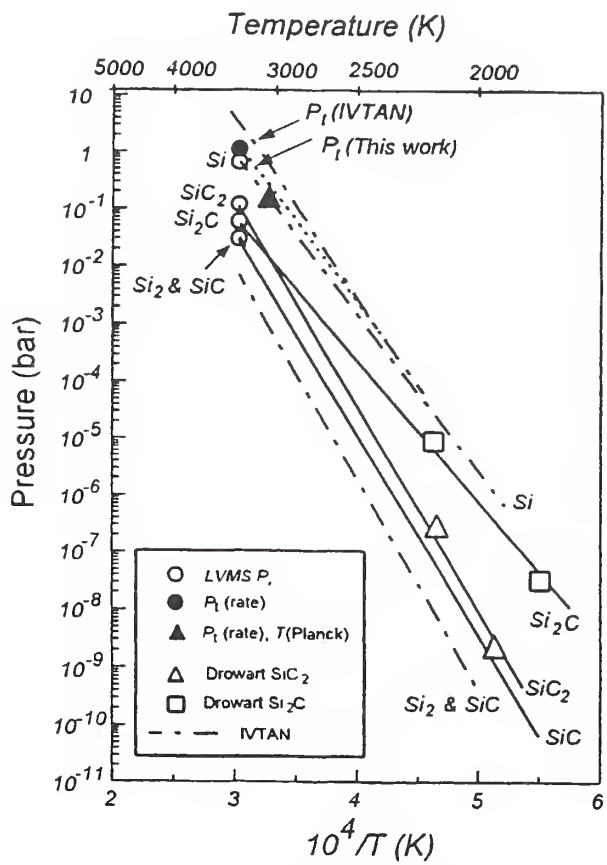

Fig. 5 Comparison of SiC LVMS P_i and deposition rate P_t vs T data with extrapolated selected literature values. Drowart [28]; Si, Si_2 [2]; SiC, IVTAN [2].

with that for C, where T_s(C) is known [i.e., T_s(SiC) = T_s(C) · T_b(SiC)/T_b(C)]. As was discussed in earlier studies [5], the shapes of the TOA profiles and their dependence on $M^{0.5}$ together with appearance potential curve analysis, were used to verify the ion-to-precursor assignments. Note in Table 3 and Fig. 5 that the partial pressures of SiC, SiC_2, and Si_2C differ significantly from the extrapolated lower pressure evaluated literature data. We also note that the present results differ from our earlier preliminary ones, owing to an incorrect assignment of hydrocarbon impurities to C_1 and C_2 [27]. For SiC_2 and Si_2C, the lower temperature data of Drowart and DeMaria [28], adjusted for our model σ's, are consistent with our results at higher temperatures.

Al_2O_3

Al_2O_3 is a relatively well-studied system, and the critically evaluated literature [1,2] may be used to further test the LVMS method and also the evaluation procedures. Because the target maintains a constant deposition rate over time (which was not always the case for other materials), this material is useful as a calibrant (e.g., for determining k for use in LVMS experiments with other materials). Tables 1 and 4 show very good agreement between the present results and the evaluated literature, with the main differences being related to use of different σ's.

ZrO_2–7% Y_2O_3

Relative abundances of ZrO and ZrO_2 were obtained by LVMS and the results used to calculate M, which, combined with deposition rate measurements, yielded values of P_t. Temperatures were obtained by the Planck radiation method. The results are compared with extrapolated literature data in Fig. 6. Upon heating under vacuum, ZrO_2 changes color, first to a gray then to a black form, due to preferential loss of oxygen. The two data sets in Fig. 6 represent the initial fully oxidized ZrO_2 form and a reduced form with approximate composition $ZrO_{1.75}$. For the selected literature curves (extrapolated from studies over solid ZrO_2) remarkable agreement is found with the IVTANTHERMO tables [2] for the ZrO_2 form and with the data of Hoch *et. al.* [29] for the reduced system. The small contribution of volatiles from Y_2O_3 can be neglected for these comparisons.

Y_2O_3

Figure 7 compares data obtained by the rate method with extrapolated literature curves. Based on the lower temperature literature MS observations [31] and bond energy arguments we expect YO and O as

Table 4 Al_2O_3 partial pressures (bar = 10^5 Nm^{-2}) at (A) 3500 K and (B) 3900 K.

Species	A					B			
	LVMS[a]			Literature		LVMS[a]		Literature	
	$I\Delta t$ (counts)	S	σ ($\times 10^{-16}$ cm^2)	P_i	P_i(2)	$I\Delta t$ (counts)	P_i	P_i (1)	P_i(2)
Al	3	0.83	6.1[b]	0.018	0.014	22	0.10	0.10	0.10
O	–	0.9	0.7		0.019	9.4	0.54	0.24	0.28
AlO	–	0.96	1.2		0.020	4.8	0.15	0.16	0.18
Al_2O	–	0.96	6.1		0.006	5.0	0.03	0.05	0.07
						P_t =	0.82	0.55	0.63

[a] $k = 9.0 \times 10^{-6}$ atm K^{-1} $counts^{-1}$ t^{-1} (from p_c, see Table 2), λ = 532 nm.
[b] 9.6 (20).

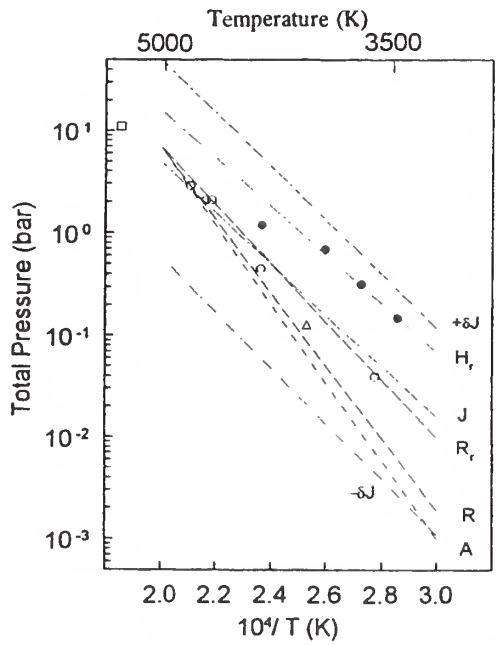

Fig. 6 Comparison of $ZrO_2 - 7\%Y_2O_3$ P_t vs. T data with extrapolated literature values (curves). Open symbols are for unrreduced (i.e., initial) material, and closed symbols are for the partially reduced system (see text). P_t obatined using $n = 11.7$, $M = 92$, and $P(ZrO)/P(ZrO_2) = 0.5$ (LVMS). Data uncertainty limits are similar to those indicated in Figs. 4 and 7. Curve A, extrapolation of Ackerman *et al.* [30] data for vaporization to ZrO_2 (g); curve R [2]; curve J [1], ± δJ uncertainty; curve H_r extrapolation of Hoch *et al.* [29] ZrO_2(s) + Zr(s) system; curve R_r calculated from [2] for ZrO_2 (ℓ) + Zr(ℓ) system.

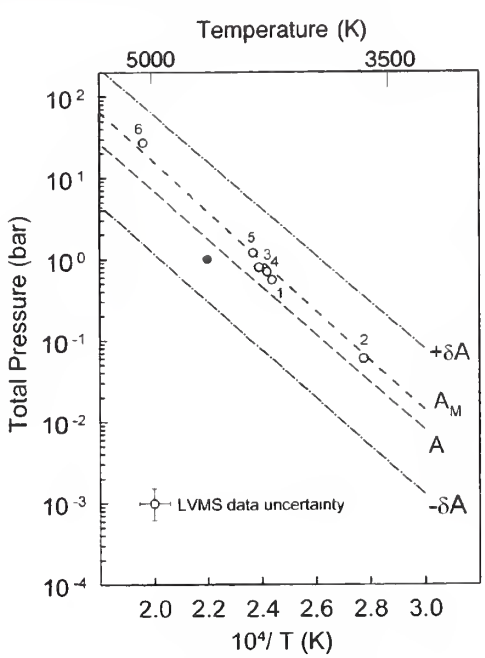

Fig. 7 Comparison of Y_2O_3 P_t vs. T data with extrapolated literature values (curves) $n = 11.7$, $M = 90$. Data points (open circles) are numbered in chronological order. Curve A is extrapolated from solid-phase data of Ackerman *et al.* [31] with an estimated enthalpy of melting; ±δA are uncertainties of [31]; curve A_M is extrapolated from Ames *et al.* [32]; filled circle point is 1 bar (10^5 Nm^{-2}) P at T cited by Schick [33].

the significant vapor species, from which M may be calculated. Good agreement is found with the extrapolated data of Ackermann *et. al.* [31] and particularly that of Ames *et. al.* [32].

SUMMARY AND CONCLUSIONS

Previous limitations associated with the application of laser vaporization mass spectrometry to thermochemical studies at very high temperatures have been resolved to the extent that new, more accurate vapor pressure and related thermodynamic properties can now be determined. In particular, the measurement of time-resolved thermal emission intensities over a wide range of wavelength has allowed for direct temperature determinations. Significant improvements in the ease of measurement, and in data accuracy, have been made for the determination of total and partial pressures. A key development in this respect has been the use of *in situ* deposition rate measurements, concomitant with the mass spectrometric and temperature measurements. Also, the ability to sweep the position of the rate monitor across the vapor plume now allows for *in situ* measurement of the $\cos^n\theta$ spatial distribution which can differ appreciably ($n \sim 4$ to 12 or more, typical) relative to the usual effusive behavior where $n = 1$. With a knowledge of this distribution, one can readily relate the measured deposition rate to the vaporization rate of the sample. Then the classical Hertz–Langmuir gas–kinetic relationship, modified for hydrodynamic conditions, can be used to determine pressure from vaporization rate provided the vapor molecular weight (M) is known, where M is typically an abundance-weighted average of the various species present. To obtain M, the MS analysis of ions must yield the correct molecular precursors and their relative abundance. The precursor assignment is greatly enhanced by the use of velocity or time-of-arrival information, readily obtained by LVMS. Also, the order-of-magnitude cooling associated with the vapor expansion process appears, in most cases, to reduce the degree of electron impact fragmentation normally present in high-temperature (KMS) beams.

The LVMS technique should be applicable to most inorganic materials with the following limitations. The material must be absorbing (even if only to a limited extent) at the available laser wavelength, although materials with a small extinction coefficient (e.g., Al_2O_3) can be heated by short-pulse lasers. Fortunately, laser wavelengths are available over a wide spectral range. The total pressure range appears to be limited typically to about 0.01 to 10 bar for short-pulse lasers and to about 10^{-6} to 10^{-4} bar for long-pulse lasers. The useful temperature range appears to be limited to about 3000 to 5500 K, depending on the system, and to where Planck radiation behavior can be used to measure temperature. The range can be expanded if indirect temperature measurements, based on velocity distribution analysis and known chemical equilibria, are used. We can expect the accuracy of the LVMS method to decrease at some upper level temperature and pressure. A limiting condition can be expected as light absorption (and emission) by the high density vapor or ionization (expect low T_s determination) becomes important. Also, onset of cluster formation during expansion would affect M determination for P-rate, leading to a high P_t determination.

With respect to the systems considered here, it appears that new critical evaluations may be warranted for the candidate reference systems of C and Al_2O_3. Likewise, for the other systems studied, the partial and total pressures obtained by LVMS can be used to refine existing (estimated), or to generate new, thermodynamic functions and bond dissociation energies. More reliable estimates of the critical point T,P should also be possible using the present data. We note that the strong preference given to third law versus second law critical evaluations of the lower temperature vaporization data (e.g., see ref. 2) may not always be warranted. From the LVMS results obtained to date, it appears that the extrapolated KMS data, where available, are sometimes more reliable than one might expect, given the dependence on estimated enthalpies of melting and many other thermal and spectroscopic parameters.

A discussion of the need for measurements in the "kilodegree" temperature range, given by Beckett in 1967 [34], is still pertinent. Similarly, in the context of predictions of T, P conditions under which metal dimers could be seen by high-temperature mass spectrometry Verhaegen *et al.* [35] noted in 1962, "...conventional mass spectrometric techniques (KMS) will have to be greatly improved to per-

mit one either to reach the temperatures (~4000 K) or to handle the pressures (~1 bar) in the extreme cases". The LVMS technique appears to meet this need.

REFERENCES

1. M. W. Chase, Jr., C. A. Davies, J. R. Downey, Jr., D. J. Frurip, R. A. McDonald, A. N. Syverud. *JANAF Thermochemical Tables,* 3rd ed., *J. Phys. Chem. Ref. Data* **14**, Suppl. No. 1, ACS, Washington, DC (1985).
2. L. V. Gurvich, I. V. Veyts, C. B. Alcock. *Thermochemical Properties of Individual Substances,* 4th ed., Vols. 1–3, Hemisphere Pub. Corp. New York (1989). Also see original Russian editions *loc. cit.*, and *NIST Special Database 5*, "IVTANTHERMO" (L.V. Gurvich, V. S. lorish, D. V. Chekhovsioi, V. S. Yungman. CRC Press, Boca Raton, Florida, 1993), a program that incorporates the above tabulations to ~1992, and can compute multicomponent equilibria based on the database.
3. J. W. Hastie, D. W. Bonnell, P. K. Schenck. *High Temp. High Press* **20**, 73 (1988).
4. J. W. Hastie, D. W. Bonnell, P. K. Schenck. *High Temp. Sci.* **25**, 117 (1988).
5. J. W. Hastie, D. W. Bonnell, A. J. Paul, J. Yeheskel, P. K. Schenck. *High Temp. Sci.* **33**, 135 (1995).
6. J. W. Hastie. *High Temperature Vapors-Science and Technology*, Academic Press, New York (1975).
7. J. W. Hastie, A. J. Paul, D. W. Bonnell, P. K. Schenck. *High Temperature Synthesis of Materials*, ACS Symposium Series 681, D. Gruen and M. Serio (Eds.), p. 39, ACS, Washington, DC (1998).
8. R. W. Ohse, J. F. Babelot, C. Cercignani, P. R. Kinsman, K. A. Long, J. Magill, A. Scotti. ln *Proc. 10th Materials Research Symp. Characterization of High Temperature Vapors and Gases*, J. W. Hastie (Ed.), p. 83, NBS SP 561, NTIS, Washington, DC (1979).
9. D. Olander. Page 411 in *Materials Chemistry at High Temperatures 2*, J. W. Hastie, (Ed.), Humana Press, New Jersey (1990).
10. a) R. L. Baker, M. A. Covington, G. M. Rosenblatt. Page 143 in *High Temp. Materials II*, Z. A. Munir, D. Cubicciotti (Eds.), Electrochem. Soc., Pennington, New Jersey (1983); b) M. A. Covington, G. N. Liu, K. A. Lincoln. *AIAA Journal*, **15**, 1174 (1977).
11. J. H. Lundell and R. R. Dickey. "Response of Heat-Shield Materials to Intense Laser Radiation," p. 193, *AIAA 16th Aerospace Sciences Meeting*, Huntsville, Alabama, Jan. 16, AIAA, New York (1978).
12. *Phase Diagrams for Ceramists*, a continuing series published by The American Ceramic Society, Westerville, Ohio.
13. D. B. Chrisey and G. K. Hubler (Eds.). *Pulsed Laser Deposition of Thin Films*, Wiley, New York (1994).
14. A. J. Paul, P. K. Schenck, D. W. Bonnell, J. W. Hastie. In *Proc. MRS Symp. Film Synthesis and Growth Using Energetic Beams*, **388**, 45, MRS, Warrendale, Pennsylvania (1995).
15. A. Ranjin, S. Sinha, P. K. Ghosh, J. W. Hastie, D. W. Bonnell, A. J. Paul, P. K. Schenck. *J. Chem. Phys. Lett.* **277**, 545 (1997).
16. J. Paul, J. W. Hastie, P. K. Schenck, D. W. Bonnell, M. D. Vaudin. *Proc. MRS Symp.* Vol. 526, p. 243, MRS, Warrendale, Pennsylvania (1998).
17. P. K. Schenck, J. W. Hastie, A. J. Paul, D. W. Bonnell. *Opt. Eng.* **35**, 3199 (1996).
18. D. W. Bonnell and J. W. Hastie. In "Characterization of High Temperature Vapors and Gases," NBS SP 561, **1**, 357 (1979).
19. J. Drowart, C. Chatillon, J. W. Hastie, D. W. Bonnell. "High Temperature Mass Spectrometry: Accuracy of the Method and Influence of Ionization Cross Sections," *Pure Appl. Chem.* (2001), to be published.
20. R. S. Freund, R. C. Wetzel, R. J. Shul, T. R. Hayes. *Phys. Rev. A*, **41**, 3575 (1990).

21. J. B. Mann, Page 814 in *Recent Developments in Mass Spectrometry*, K. Ogata and T. Hayakawa (Eds.), Univ. Park Press, London (1969). See also ref. 19.
22. J. W. Hastie. "A Model for Ionization Cross Sections of High Temperature Molecules," to be published (2000).
23. J. W. Hastie and J. L. Margrave. *J. Phys. Chem.* **73**, 1105 (1969).
24. J. W. Hastie and J. L. Margrave. *Fluorine Chem. Rev.* **2**, 77 (1968).
25. P. K. Schenck, unpublished observations (2000).
26. a) K. D. Carlson, P. W. Gilles and R. J. Thorn, *J. Chem. Phys.* **38**, 2725 (1963); b) F. Tehranian, *The Kinetics of Laser Pulse Vaporization of Uranium Carbide by Mass Spectrometry*, (LBL-15982 Univ. Calif., Berkeley, CA, 1982).
27. D. W. Bonnell, P. K. Schenck, J. W. Hastie, M. Joseph. *Proc. Electr. Chem. Soc. Symp. High Temp. Chem*, ECS, Pennington, New Jersey (1990).
28. J. Drowart and G. DeMaria. *Silicon Carbide*, J. R. O'Conner and J. Smiltens. (Eds.), pp. 16–23, Pergamon, New York (1960).
29. M. Hoch, M. Nakata, H. L. Johnston. *J. Amer. Chem. Soc.* **76**, 2651 (1954).
30. R. J. Ackermann, E. G. Rauh, C. A. Alexander. *High Temp. Science* **7**, 304 (1975).
31. R. J. Ackermann, E. G. Rauh, R. J. Thorn. *J. Chem. Phys.* **40**, 883 (1964).
32. L. L. Ames, P. N. Walsh, and O. White. *J. Phys. Chem.* **71**, 2707 (1967).
33. H. L. Schick. *Thermodynamics of Certain Refractory Compounds*, Vol 1, Academic Press, New York (1966).
34. W. Beckett. *The Characterization of High Temperature Vapors*, J. L. Margrave (Ed.), p. 3, Wiley, New York (1967).
35. G. Verhaegen, F. E. Stafford, P. Goldfinger, M. Ackerman. *Trans. Far. Soc.* **58**, 1926 (1962).

APPENDIX B

1080–1278/95/3302-3–0135 $11.00

High Temperature Chemistry in Laser-Generated Plumes**

J. W. HASTIE,* D. W. BONNELL, A. J. PAUL, J. YEHESKEL,† AND P. K. SCHENCK

Materials Science and Engineering Laboratory
National Institute of Science and Technology,
Gaithersburg, MD 20899

ABSTRACT

Plumes of high- and ultra-high (>3000 K) temperature vapor species may be conveniently generated from any material of interest by pulsed laser-surface interactions that lead to vaporization, ablation, or other vapor generation processes. The characterization of these plumes, and their application in new areas of science and technology, has been the subject of considerable study in recent years as evidenced by the numerous international symposia, books, and papers published (e.g., *see* ref. *(1)*). On the occasion of this special symposium, held in recognition of the scientific achievements of John L. Margrave, we *summarize* recent results and extend interpretation of earlier studies on the high temperature chemistry aspects of laser plumes derived from inorganic and ceramic materials. The chemical environment can be considered as extreme—a condition characteristic of many of the investigations of John Margrave.

Particular attention is given to determination of vapor species identities and measurement of their concentrations, velocity distributions, and temperatures. We find that a significant window of laser conditions exist whereby the plume neutral species exhibit local thermodynamic equilibrium. One can therefore utilize these plumes for determination of high temperature thermochemical stabilities or use thermochemical models to describe the chemical condition of many laser-generated plumes.

**This article is based on a talk given by J. W. Hastie at Rice University as part of the John L. Margrave Research Symposium, April 29, 1994.

†NIST Guest Scientist: Permanent address: NRCN, POBox 9001, Beer-Sheva, Israel

*Author to whom all correspondence and reprint requests should be addressed.

Index Entries: Ceramic thin films; gas kinetics; gasdynamics; high temperature chemistry; imaging; laser-materials interaction; mass spectrometry; plasmas; pulsed laser deposition; spectroscopy; thermodynamic equilibrium.

INTRODUCTION

Application to Classical High Temperature Chemistry

In our laser-materials interaction studies, the main applications to high temperature chemistry generally have comprised:

1. The utility of pulsed high energy lasers, particularly of the Nd/YAG and excimer variety, for the production of ultra-high temperatures; typical surface-vapor interface temperatures attained are 3,000–8,000 K.
2. The use of focused laser beams to avoid material containment problems; typical application spot diameters are 0.1–5 mm with laser pulse durations of 10–40 ns.
3. The production and characterization of diverse modes of interaction involving high temperature species; interactions include thermodynamic, photochemical, thermomechanical, chemical kinetic, and gasdynamic processes.

The need for these applications arises from limitations inherent with the classical measurement methods of high temperature chemistry. For instance, with molecular-level studies of high temperature vaporization, the Knudsen mass spectrometric method is limited to temperatures generally less than about 3000 K and to pressures of less than about 10^{-4} bar*. Likewise, the newer transpiration mass spectrometric (TMS) method, although capable of sampling higher pressures (~0.1–10 bar), is also temperature-limited by container reactions *(2,3)*. The utility of pulsed laser vaporization (PLV) as a research tool and for technological applications requires an understanding and control of the conditions whereby the various modes of interaction listed above occur. In the discussion that follows, emphasis is given to work carried out in our laboratory that addresses this state of understanding.

*1 bar = 10^5 Pa. The bar is used in this manuscript for purposes of clarity and continuity with earlier work upon which this article depends. The bar is the current reference pressure for the bulk of the thermodynamic literature, is an accepted unit with a simple metric conversion to the SI pascal for limited applications, and is appropriately used where a convenient unit with the value of unity at common conditions is advantageous.

Application to Thin Films

The commercial production of compositionally complex thin films deposited from laser-generated vapor plumes is of current high interest *(4,5)*. A catalyst for the recent expanded research and development activity resulted from the early success, around 1987 (*see* p. 5 of ref. *1*), of pulsed laser deposition (PLD) in the production of "high temperature" (high T_c) superconducting thin films of YBaCuO phases, where other established deposition technologies had failed, at least initially. Among the important advantages of PLD, over other vapor deposition methods, is the relative ease of maintaining the compositional stoichiometry of the target in the deposited film at relatively low substrate temperatures. All material classes appear to gain this advantage. Also, the wide range of species deposition energies available (typically 0.1–100 eV) allows for tailored production of desired phases at reduced substrate temperatures. Recent advances in PLD can be attributed to the ongoing progress in understanding the chemistry and dynamics of the laser-target interaction, plume formation, expansion, and, to a lesser extent, deposition processes. In the discussion that follows, we will not consider, explicitly, the PLD process, but rather focus on the underlying aspect of plume chemistry.

The laser variables that control the plume chemistry and, ultimately, film quality include the fluence (E, J/cm^2), wavelength (λ, nm), and pulse time (τ, ns), together with the spot area (cm^2) and shape at the target surface. Ambient gas pressure and composition, target composition, morphology, and intrinsic properties, such as optical absorptivity, thermal conductivity, and so forth, together with the morphology and crystallographic character of the substrate, are other important system variables, as are the relative spatial orientations of the laser beam, target surface, plume, and substrate.

Nature of Laser Plumes

In principle, modern pulsed lasers have sufficient power to directly heat the impact point on any surface to that material's critical temperature (T_{crt}); the vapor pressure (P_{crt}) developed could therefore be as high as several hundred bar, or more (e.g., *see* p. 155 of ref. *(1)*). Significant development of the vapor phase occurs on a time scale (~1 ns) much shorter than the typical laser pulse envelope time (10–30 ns) used for PLV and PLD. Also, the presence of high photon fluxes, together with high temperatures and vapor densities, favors an initial production of ions and free electrons, leading to plasma conditions very near (μm) the surface. Such conditions can render the developing plume opaque to the laser, and affect the degree of laser-surface interaction. Hence, it is generally not possible to accurately predict the surface thermal state with simple energy balance arguments that do not account for difficult-to-quantify laser-plume interaction effects. In the discussion that follows,

we have intentionally limited any detailed consideration of laser-surface and laser-plasma interactions, for which there exists a significant body of physical evidence (e.g., *see* pp. 55 and 115 of ref. *1* and p. 61 of ref. *5*). The discussion will focus more on the chemical consequences of such interactions.

We adopt the following terminology: *plume* is used in general, or where the neutral components are the major material transport constituents of the laser-generated vapor; *plasma* is used where the electron and ion constituents of a plume are to be emphasized; *visible plume* is used where emission features are visually observable and/or characteristics of emitting regions are pertinent to the discussion. With respect to discussions here regarding laser energy or fluence used for PLV, we define the following conditions: *low* = <2 J/cm^2; *moderate* = 2–8 J/cm^2; and *high* = >8 J/cm^2. In other contexts not considered here (desorption, cutting and welding, and so forth), different definitions might be chosen. It should be noted that the effectiveness of energy coupling to the target depends on λ, and on the target material's optical constants (absorption coefficient, emissivity, reflectivity, and so forth), and includes empirical factors related to surface conditions, such as oxidation, grain morphology, extent of target "damage" by prior laser pulses, and redeposited material.

The energy utilized to form laser plumes is generally well in excess of that needed to establish a vaporization threshold. Hence, the plumes characteristically contain some excess energy, a portion of which often reveals itself in the form of spectral and continuum emissions over a broad wavelength span, from the infrared to the ultraviolet. This visualization feature has proven to be useful in monitoring and understanding the processes present in these plumes, as shown by the example of Fig. 1. The visible plume is a result, for the most part, of the highly energetic collisional conditions present during the expansion process. As such, the visible plume does not necessarily represent the nature of the more abundant, nonluminous, lower energy plume components, but some correlation is possible, and the structure and dynamics of the emitting regions can provide extremely useful insight into general plume dynamics *(6,7)*.

The stylized schematic of Fig. 2 emphasizes three main structural regions of laser plumes. Beyond the highly localized, near-surface, transition interface between the "stagnation zone" and the "adiabatic expansion" region, a rapid (<1 μs), supersonic, unsteady adiabatic expansion dominates the gasdynamics. Depending on the vacuum conditions (background pressure, system conductance, and so forth), the entire expansion process can result in a pressure reduction, typically, from $P_s \gtrsim 1$–10 bar near the surface to a value near the background pressure (10^{-6}–10^{-10} bar for these studies) present a few mm to cm distance above the target surface.

It should be noted that some PLV or PLD conditions are even more complex than those considered here. For instance, the visible plume images of Fig. 1 show the development, over time, of the usual axisym-

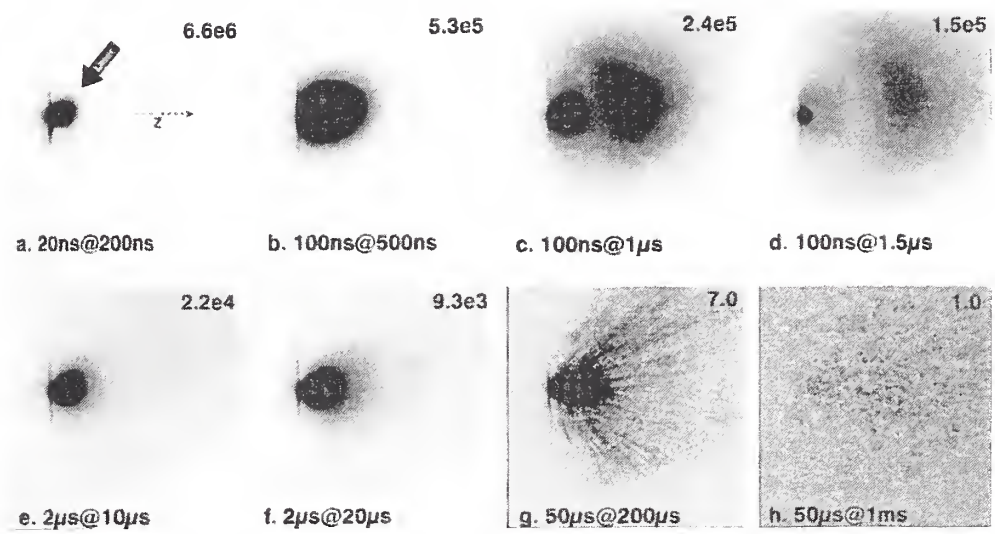

Fig. 1. Plume ICCD (Intensified Charge Coupled Device) camera images (negative representation) of emission from a BN target as a function of time (~ 0.1 Pa ambient pressure). Pulsed KrF excimer laser, λ = 248 nm, E ~ 25 J/cm^2, τ ~ 34 ns. The gate integration and delay times, respectively, are indicated for each frame. The intensity span displayed in each frame is scaled to the frame maximum; an indicator of the maximum intensity in each frame is given in the top right-hand corner. Estimated timing uncertainty < ± 5 ns absolute; frame to frame (relative) intensity uncertainty is limited by image reproduction quality.

metric plume structure. But, at 1 μs (frame c), two separated plume regions formed, followed at longer times (200 μs, frame g) by evidence of particulate release from the target. The longer times associated with *observation* of plume particulates is consistent with their relatively low velocities ($\gtrsim 10^4$ cm/s). Thus their time of origin at the surface may well coincide with that for the other plume species, with their presence concealed by the plume emission (*see* p. 14, 71, and 160 of ref. *1*). We have recently observed *(8)* that a major factor leading to particulate ejection is the mechanical condition of the target's surface, which can undergo damage enhanced by repeated laser impacts at the same point(s), promoting particulate release. In the case shown in Fig. 1, it is also noteworthy that the plume axis deviated from the usual surface normal, tracking toward the angle of the incoming laser beam (frame c). This observation is direct evidence for laser-plume interaction effects, particularly for elevated fluence conditions *(7)*.

Not considered explicitly here, but also pertinent to chemical transformations in laser plumes, is the effect of the presence of a downstream deposition surface on increasing the downstream plume density. Our image analysis work has indicated an enhancement of the plume emission as it reaches the substrate, apparently by collisions with a higher

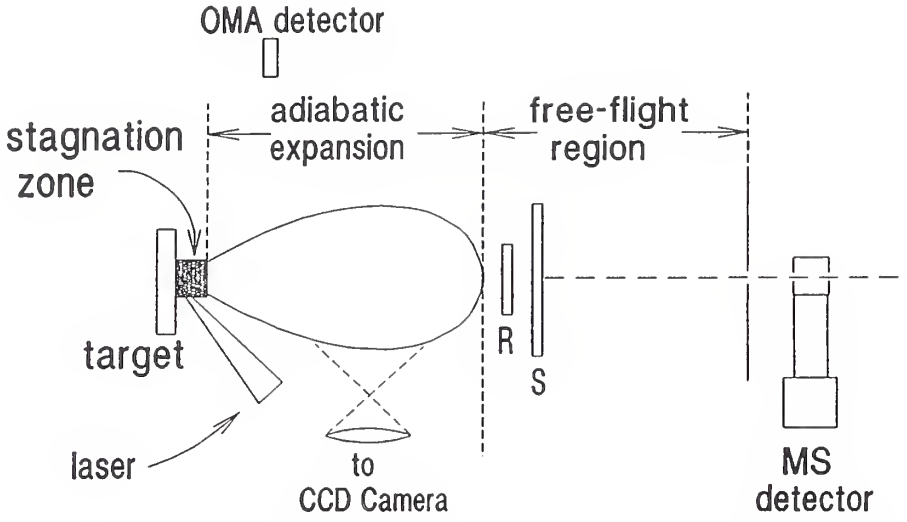

Fig. 2. Schematic of laser plume and various *in situ* probes. R is a deposition monitor and S is a (removable) substrate. Optical detection devices indicated are Charge-Coupled Device (CCD) and PhotoDiode Array (PDA) with wide-band gated intensifiers, incorporated into Optical Multichannel Analyzer (OMA) systems. The MS detector is a quadrupole mass filter with a cross-beam electron impact ion source.

vapor density stagnation zone *(9)*. This emission enhancement has been considered in more detail by Predtechensky et al. *(10)*, who have shown, experimentally and theoretically, the presence of shock and clustering effects at deposition surfaces. Also, in many PLD applications, the ambient condition is not vacuum but some controlled partial pressure of a background buffer or reactive gas (e.g., N_2, O_2, and so forth, at pressures typically in the range 0.1–15 Pa) The presence of a background gas introduces additional opportunities for plume–ambient gas chemical reactions, in addition to self-induced gasdynamic effects. Elsewhere, we have presented work on the effects of ambient gas pressure on plume macrostructure *(11)*.

APPARATUS AND EXPERIMENTAL PROCEDURE

All components of laser-produced plumes are strongly space- and time-dependent. Hence, efforts to characterize the plume physical–chemical dynamics require a multifaceted approach that utilizes special measurement systems.

Figure 2 schematically shows our general measurement approach, incorporating *in situ* intensified charge-coupled device (ICCD)-based imaging *(6)*, optical multichannel spectroscopy (OMA) *(12)*, and time-

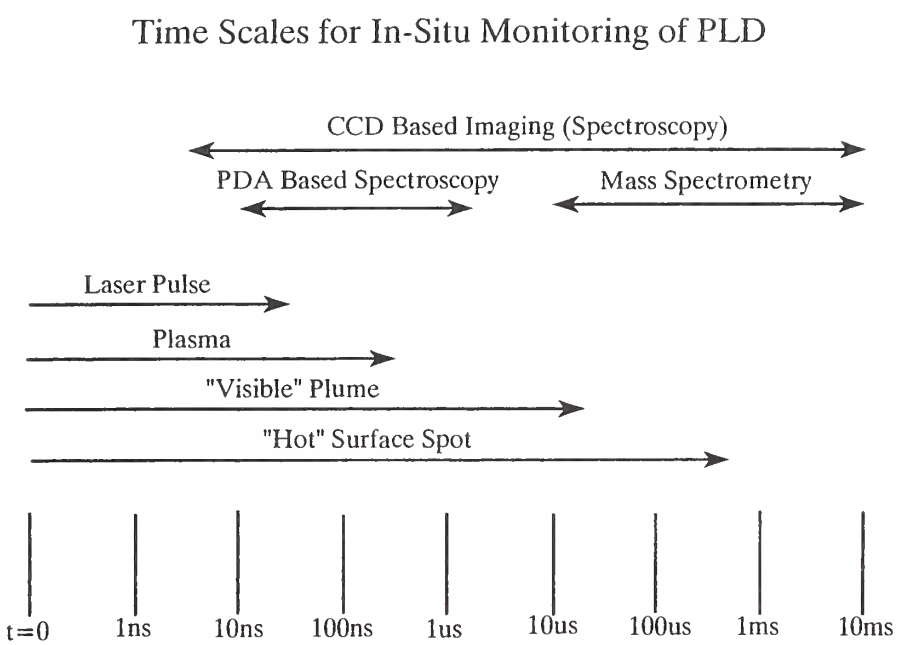

Fig. 3. Representative time-scale for characteristic events and for *in situ* monitoring of laser plumes.

resolved molecular beam mass spectrometry (MBMS) *(13,14)* as plume diagnostics. The time-scale relationships between the various measurement approaches effectively encompass the characteristic times of various phases of plume formation, as illustrated in Fig. 3. Recent, updated descriptions of the experimental facilities may be found elsewhere *(7,15)*.

The laser sources used include: (1) a Q-switched flashlamp-pumped Nd/YAG laser, operated at λ = 1064 or doubled to λ = 532 nm, with $\tau \lesssim$ 10 ns; (2) a recirculated, energy-stabilized excimer laser with unstable resonator optics, operated at λ = 248 nm (KrF) with $\tau \sim$ 34 ns. Laser fluence is a difficult parameter to detemine accurately, particularly where tightly focused beams are used. Under some conditions (e.g., spot sizes <0.002 cm^2), the measured spot size changed with laser energy even for fixed beam cross-section. Where possible, we avoided this condition. Spot sizes were measured *via* traveling microscope from spots burned into copper foil or ablative "beam marker" material, or, in some cases, from SEM photographs of actual craters. Fluence was typically varied by adjusting and measuring the laser energy for a fixed spot size. Optical losses were measured and corrections applied for each element in the beam path, with care taken to minimize losses resulting from deposition coating and damaged elements.

For these studies, laser and target conditions were generally selected to minimize mechanical effects, such as particulate ejection and splashing. Targets were rastered to utilize nearly the entire available surface

and to minimize the effects of laser-induced surface damage. When present, excessive surface damage effects were evident from visual observation of the plume and microscopic analysis of post-run target surfaces.

Molecular Beam Mass Spectrometry

Because much of the discussion to follow is based on results obtained using MBMS, the essential features of the method are given here. For MBMS analysis, once the plume had fully expanded to an essentially collision-free molecular flow in a high vacuum, high conductance region, a representative beam was extracted by a series of differentially-pumped collimation orifices located in the free-flight region (*see* Fig. 2). The quadrupole-based MBMS system used a mutually perpendicular neutral-electron-ion beam geometry with electron-impact ionization for MS analysis of the neutral species. Low energy ($\lesssim$ 20 eV) plume ions can also be detected, simultaneously or separately. The pulsed nature of the laser heating/vaporization process allows for time-resolved MS detection.

In a typical experiment, the quadrupole mass filter was tuned to a specific mass of interest and the ion signals were collected as a function of time, t, referenced to the laser pulse. Using signal averaging (ion current detection) and, more recently, multichannel scaler pulse collection, the MS signals were averaged with time resolution as short as 1.28 μs. Although higher time resolution is available, this time resolution was chosen for counting as the best trade-off between maximum detectable beam velocity (currently limited to $\lesssim 5 \times 10^6$ cm/s) and number of laser shots required (~ 1000, typically) to collect statistically significant count levels in each bin. Peak count rates were typically <1–6 $\times 10^5$ count/s.

We denote the raw MS data as time-of-arrival (TOA) mass-filtered intensities, $I(t)$. Plots of $I(t)$ vs TOA (t) are essentially time transformations of velocity distributions *(12,14,15)*. The MS ion source is a species number density detector; multiplying $I(t)$ by the velocity, v ($=\ell/t$, where ℓ is the flight distance, currently 47.4 ± 0.1 cm), converts the observed signal to abundance ($I \times v$, a flux), appropriate for velocity distribution analysis and direct comparison with the optically determined data *(6,7)*.

Species Concentrations/Partial Pressures

The mass spectral intensities can be converted to relative or, in some instances, absolute species concentrations and partial pressures *(13,14)*. Partial pressures, P_i, are determined from the mass spectral ion intensities, I_i, that result from electron impact ionization of the corresponding parent neutral (species i) in the MS ion source using the relationship:

$$P_i = k_i I_i T_s \tag{1}$$

where k_i is an instrumental electronic and geometric sensitivity parameter (*see also* procedure 5, below). T_S is the source temperature that, for the present studies, was taken as the value at the surface or in the near-

surface pre-expansion plume. Equation 1 is based on the following assumptions and data treatment procedures:

1. The establishment of a Maxwellian velocity distribution among various molecular species, i.e., the existence of a thermodynamic temperature and pressure, at least in terms of kinetic energy.
2. The validity of the Hertz-Langmuir relationship between vaporization flux, molecular weight, surface pressure, and temperature.
3. The approximation of the Ideal Gas Law relationship among pressure, number density, and temperature.
4. The number density detection nature of the MS ion source.
5. Inclusion in the sensitivity constant, k_i, of species- and mol-wt-specific factors for gasdynamic mass separation effects (mass and species dependence of n in the $\cos^n$ dispersion of the material flux), ionization cross-sections, and mass filter transmission and multiplier efficiencies.
6. Correction of the observed intensity signal for response time (analog) or counting discrimination, together with background gas inclusion and/or scattering effects, geometric sampling restrictions, and accommodation coefficient and electron impact fragmentation contributions/losses.

Values of k_i are difficult to determine under actual laser plume mass spectrometric sampling conditions. Therefore, we separately simulated the plume density and gasdynamic expansion conditions using a transpiration supersonic beam source *(3,14)* in the same vacuum system. Known mixtures of NaCl, $(NaCl)_2$ in Ar, a mixture of the stable inert gases (1% of each of He, Ne, Ar, Kr, and Xe in normal isotopic abundance) in N_2, and perfluorotributylamine in N_2 were each used as partial pressure calibrants for determining gasdynamic effects, mass filter transmission and multiplier efficiencies, general ionization cross-section behavior, and the overall geometric sensitivity of the MS system for supersonic sampling. Because of the high surface temperature present during laser heating, we can expect the overall vaporization accommodation coefficient to be near unity. However, for the partial pressure ratios reported here, only the weaker assumption that the observed individual species have the same accommodation coefficient was required in the data analysis.

RESULTS AND DISCUSSION

Species Identities

Using the approach outlined above, we have identified the atomic, molecular, and positive ion species present in plumes for a wide variety of materials, as shown in Table 1 *(9)*. In principle, negative ions could

Table 1
Species Identified in Laser Ablation Plumes

Material	Application	Atoms	Ions, M^+	Molecules
Nd/YAG laser				
C	Thermo at 4000 K	C	C_{1-3}	C_2–C_9
BN	Thermo at 2800 K	B, N	—	B_2, B_3, BN, N_2
SiC	Thermo at 3500 K	Si, C	—	SiC, Si_2C, SiC_2, Si_2, Si_3, C_2, C_3
HfO_2	Thermo at 4900 K	Hf, O	Hf, HfO, HfO_2	HfO, HfO_2
MgO	Thermo at ~3300 K	Mg, O	—	MgO
$BaYCuO_x$	High T_c films	Ba, Cu, O	Ba, Cu	CuO, O_2, BaY
Ag/Fe_3O_4	Plasma study	Ag, Fe, O	Ag, Fe, O	—
$BiPbCaCuSrO_x$	Plasma study	O, Cu, Pb, Ca, Sr	Cu, Ca, Sr	CuO, SrO, CaO
Al_2O_3	Thermo at 4300 K	Al, O	Al	AlO, Al_2O
Pb_2ZrTiO_6 (PZT)	Ferroelectric films	Pb, Zr, Ti, O	Pb, Zr, Ti	PbO, ZrO, TiO, ZrO_2, TiO_2
Ag	Thermo at 2500 K	Ag	Ag	—
Eximer laser				
Ag/Fe_3O_4	Nanostr. mag. films	Ag, Fe, O	Ag, Fe	—
Pb_2ZrTiO_6	Ferroelectric films	Pb, Zr, Ti	Pb, Zr, Ti	ZrO, TiO
$BaTiO_3$	Dielectric films	Ba, Ti, O	Ba, Ti	BaO, TiO, TiO_2
$BaYCuO_x$	High T_c films	Ba, Y, Cu	Ba, Y, Cu	YO
$BiPbCaCuSrO_x$	High T_c films	Pb, Bi, Ca, Cu	Ca, Cu, Sr	CuO, SrO, CaO
AlN	Thermal films	Al, N	AlN, N	AlN
Al_2O_3	Dielectric films	Al, O	Al	AlO, Al_2O

also have been monitored, however they are likely to be of lesser significance, since the free electron concentrations are generally believed to be comparable with those of the positive ions *(16)*. Generally, the positive ions were observed with lower MS intensities and much faster velocities than for neutral species. Hence, based on the low efficiency of electron impact ionization, particularly in the cross-beam orientation used, we estimate that the postexpansion plume ion concentration levels were typically $\lesssim 10^{-4}$ of the neutrals. Pre-expansion ion levels are often much greater, however.

Where the focus of the investigation was to obtain thermodynamic ultra-high temperature vaporization data ("Thermo" in Table 1), particular attention was given to the attainment of local thermodynamic equilibrium conditions. (e.g. *see* refs. *13,14,17*). Under the moderate fluence, high mass flow (corresponding to $P_s \sim 1$–10 bar), short pulse time (10–30 ns), and reasonably low background pressure (10^{-6}–10^{-10} bar) conditions used, which are typical for vacuum PLV and PLD, no mass or TOA evidence was found for nonequilibrium cluster species. Such species, with molecular weights greater than about 2000 u (1 u = $1/N_A$=1.660566 X 10^{-24} g), have been suggested as precursors to the observed atomic and small molecular plume species (e.g., *see* p. 101 of ref. *5*). Apparently, if such cluster intermediates form under our conditions, they are very short-lived and do not survive the plume evolution process. An important observation is that the atomic and molecular species found, as summarized in Table 1, are quite consistent with what one expects from extrapolation of lower temperature vaporization thermochemical data found in the literature *(18)*.

Species Velocity Distributions

Species velocity data have been obtained from analyses of our time-dependence optical emission spectra *(12)*, ICCD images *(6,7)*, and mass selected TOA mass spectral intensities *(6,12–15,17)*. For present purposes, we will consider the $I(t)$ vs t mass spectral form of these data, which provide, by velocity distribution analysis, information on post-expansion flow velocity and internal beam temperature (T_b). The structure of the TOA ($I(t)$ vs t) profiles or peaks and the derived values of T_b provide insight into the thermal state of the pre-expansion plume and the target.

In some instances (dependent on E, λ, and so forth), one finds evidence of apparently independent multiple processes preceding the formation of the molecular beam selected for MS investigation. While single peak TOA profiles, obeying Maxwell-Boltzmann distributions, are typical *(7,14,21)*, we give emphasis here to cases representing multipeak TOA behavior. As we will show, such behavior is more likely to occur when conditions favor the plasma nature of the plume. A representative example is shown in Fig. 4, where the multiple TOA peaks for Al atoms apparently indicate the presence of several quite distinct velocity distributions.

An alternative explanation, less likely in this case, for observing multiple TOA peaks at a single mass position is that the slower peaks

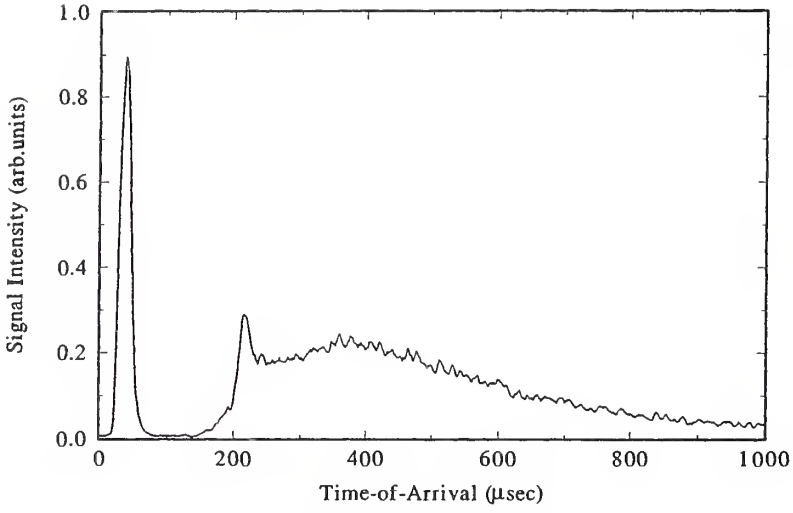

Fig. 4. Dependence of Al^+ (Al and Al^+ precursor) mass spectral intensity, I, on molecular beam arrival time at the mass filter. The plume-to-mass-filter distance was 47.4 ± 0.1 cm. Al_2O_3 target (98 + % purity); Nd/YAG laser, λ = 1064 nm, τ = 10 ns, E = 9 J/cm^2; spot size ~ 0.005 ± 25% cm^2. Estimated uncertainties are: E ± 30% (absolute); Δt = ±5 μs, and I < ± 5%.

arise from MS fragmentation of different, higher molecular weight species. This possibility can be ruled out because, as the TOA profiles show, only a few, extremely massive cluster moieties (with mol wt M ~ 5000 u) would have to exist, and with no clusters or fragments existing below ~ 1500 u. Such a cluster MS pattern would be extremely atypical. Analysis, with the assumption that these TOA peaks were caused by very heavy molecules, resulted in inconsistent fits to the velocity distributions. Thus, in the case of Fig. 4, the fastest peak cannot be a fragment and the other peaks do not correspond to higher molecular weight precursors. Hence, the TOA multiple peaks must result from species of a single mass (Al in Fig. 4) undergoing collisionally separate processes during the vaporization/ablation/plume-forming stage. The discussion of Figs. 5 and 6 (*see* "Laser-Plume Interactions" and "Cause of Laser-Plume Interaction") further supports this interpretation.

Thermal Interaction

The slow TOA peak found here (at ~ 380 μs in Fig. 4), and in earlier studies on other materials *(14)*, can generally be attributed to a predominately thermal vaporization-type process. Such a process (favored at longer λ) involves direct laser heating of the target surface and generation of a predominately neutral vapor having a composition thermodynamically determined by the peak surface temperature.

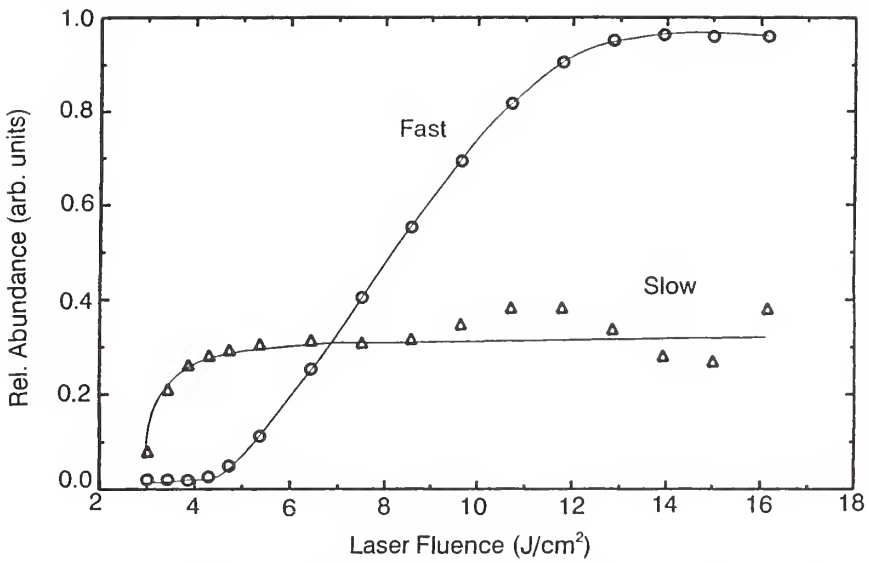

Fig. 5. Dependence of time-integrated, velocity-corrected intensities (abundance= $\int$ (I X v)dt) of fast (< 100 μs TOA) and slow (>100 μs TOA) Al TOA peaks, as depicted in Fig. 4, on laser fluence; spot size ~ 0.005 ± 25% cm^2. Estimated uncertainties are: E ~ ± 10% (relative), ±30% (absolute); relative abundance, ±5%. Note that the abundance scales for fast and slow signals are not necessarily directly related because of uncertainty in relative transmission and sensitivities of ions or fast neutrals vs. slow neutrals. Also, Al (slow) has a weaker *E* dependence than for observed deposition rates. Based on our observed deposition rates and arguments given in the text, Al source (near-surface) parameters are approximated as:

Number density, cm^{-3}	Pressure, bar	E, J/cm^2
10^{17}	0.05	3.0
10^{18}	0.5	3.8
$\gtrsim 10^{19}$	$\gtrsim 5$	12

See also ref. *(28)* for comparable number densities obtained from spectral absorbance measurements, and *(19)* for comparable pressures derived from weight loss measurements, and (*31*) for model plasma threshold number densities for Al.

A knowledge of the conditions required for thermal vaporization is particularly important for PLV application to thermochemical studies. Figure 5 shows the effect of fluence on the thermal (slow) TOA peak and the relationship between the slow and fast TOA peaks (TOA ~ 380 and ~ 30 μs, respectively, in Fig. 4). Note that the thermal component is the dominant feature over the fluence range, E = 3–5 J/cm^2. Also, we found that T_b for the slow peak decreases from ~ 3000 to $\lesssim$ 1000 K over this fluence range, and then is essentially unchanged (±250 K) out to E = 12 J/cm^2. This initial decrease in T_b with E is an indication that the degree

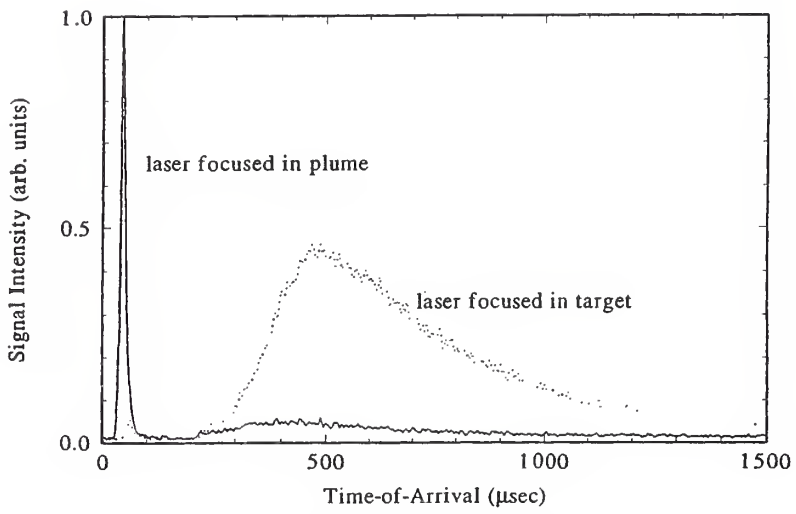

Fig. 6. Effect of laser focus position (in plume vs. at target) on plume Al MS abundance. Al_2O_3 target, excimer laser, λ = 248 nm, τ ~ 34 ns, E = 9 J/cm^2, spot size ~ 0.005 ± 25% cm^2. Note: shorter λ used than for study in Figs. 4 and 5. Estimated uncertainties similar to Fig. 4.

of expansion cooling (*see* "Gasdynamic Expansion") increases much more strongly than T_S increases. A decrease in beam temperature is generally a clear indication of a source pressure increase, in agreement with the relative abundance trend in Fig. 5. This range of T_b values is also consistent with relatively low values of T_S (~ 3500–4500 K) and P_S (~ 10^{-2}–1 bar).

Nonthermal Laser-Plume Interaction

The fast peak behavior, represented in Figs. 4 and 5, apparently results from an independent, in time/space, nonthermal process that imparts excess energy to the observed species at some early stage of the plume history. Onset of this particular fast peak feature also coincided with the appearance of a visible plume. It is important to note that both the slow and fast peaks (when present) generally exhibit *independent* local Maxwellian velocity distributions. Each distribution must therefore arise from separate regions (time/space) of the plume that are not in significant collisional interaction.

A clue to the nature of the so-called nonthermal interaction is given by noting the differing dependence of the fast and slow TOA peaks on laser fluence, as shown in Fig. 5. At E > 4 J/cm^2, growth of the slow thermal peak is clearly limited by some process and only the fast peak abundance continues to increase with added fluence. Maxwell velocity distribution analysis revealed that the fast peak represented a population of very high temperature or kinetic energy species *(15)*. Furthermore, val-

ues of T_b forthis population increased concomitantly with fluence from ~ 5000 K at 4 J/cm^2 to ~70,000 K at 16 J/cm^2.

Two alternative processes for the laser-surface interaction require consideration: either (1) the surface pressure/temperature continues to increase exponentially with fluence up to perhaps near the material's critical point (where the distinction between condensed and vapor phase vanishes), estimated as ~ 200 bar and ~ 8000 K for Al_2O_3; or (2) some process restricts the degree of surface heating above a certain limiting fluence level. The first possibility appears to be eliminated by the values of T_b(fast) being far too high to be related merely to an increase in surface temperature, even if no expansion cooling occurred. Support for the second possibility is provided by the observation that the slow thermal peak, which we identify as being directly produced at the surface and also gasdynamically linked to the surface pressure/temperature condition, is strongly limited in both its abundance and its postexpansion temperature above about 4 J/cm^2. The separate Maxwellian behavior noted for the fast peak indicates that it must arise from a process divorced from the overall thermal process yielding the slow peak. The fact that the fast peak becomes significant at the onset of the limiting process for the thermal peak suggests a linkage between the processes. The two most likely sources for the fast peak are either that it represents a short-lived transient of "temperature" and "pressure" early in the laser pulse, or that the fast peak arises from laser interaction with the developing plume front. The first possibility could be significant, but offers no explanation of the apparent link between the two populations. The second possibility is reasonably well known at moderate fluence, although there appear to be no detailed investigations reported.

Selfregulation of PLV

If we consider a case where the laser-plume interaction resulted in the plume becoming increasingly opaque/absorptive/reflective to the excess laser energy, then a self-regulating mechanism could arise as the surface becomes increasingly shielded from the laser beam with increasing fluence, thereby limiting the vapor-forming process. Observed optical emission intensity and plume temperature continued to increase with fluence beyond onset of the process that halts the increase of the slow peak abundance, consistent with the behavior of the fast TOA peak and with a mechanism whereby the plume increasingly absorbs laser radiation above some minimum pressure/number density. Also, ICCD images show the plume luminosity tracking along the laser path—a characteristic clearly indicative of laser-plume interactions.

We believe that the concept of a plasma-controlled self-regulating regimen close to the target applies here (e.g., *see* p. 281 of ref. 5). Similar nonlinear fluence-limiting deposition rate (≈target vaporization) behavior at 1064 nm and 5 J/cm^2 has been attributed (*see* p. 325 of ref. 5) to plasma

formation early in the pulse and consequent "reflection" of the remaining part of the laser pulse's energy. Optical depth limitations in laser–target interaction with increased fluence, likely for high optical absorbance materials and short wavelengths (*see* ref. *30a*) are considered to be secondary controlling mechanisms in the present case.

Above about 12 J/cm^2, another, more global, manifestation of the self-limiting process becomes apparent in Fig. 5, constraining the fast-peak species abundance as well. The possibility that the observed fast-peak signal is rolled off as the result of an MS detection limitation for faster species has not been completely eliminated, although such a limitation would require the fast peak to be dominated by species with post-expansion translational energies of 15 eV or more. However, the observed fastest distribution (earliest TOA peak) of Fig. 6 (*see* "Cause of Laser-Plume Interaction") suggests that the fast peak data in Fig. 5 are not yet sufficiently energetic for detection to be substantially limited by the MS ion source draw-out potentials. Other potential signal detector limitations (frequency limitations, scaler pulse-pile-up loss, and so forth) have been eliminated. Thus, the cause of the effect limiting the fast peak is attributed to a change in the detailed nature of the laser-plasma interaction. For the present discussion, the pertinent observation about this second limit for the higher fluence range is that the laser interaction process producing the fast, high-energy peak appears to be dominating the gasdynamics as well at the thermal portion of the laser-induced vapor.

The suggestion that the surface is shielded from the laser by the plasma component of the plume is further supported by Al_2O_3 target weight loss measurements, made under similar fluence conditions at $\lambda = 1.06 \times 10^4$ nm *(19)*. Those observations parallel the results of Fig. 5, and clearly show the presence of a limiting process, manifested both as a relatively low dependence of rate-of-weight loss on fluence and as a peaking in the material flux at ~ 13 J/cm^2. In the absence of a surface shielding effect that limited laser access to the surface, the surface temperature/pressure expected from heat balance estimates should cause both the target rate-of-weight loss and the MS relative abundance data of Fig. 5 to show more than an order of magnitude increase as the fluence changes from 4 to 12 J/cm^2 (e.g., *see* pp. 126 and 256 of ref. *1*). However, in each case, only a factor of 4× increase was found. This reduced rate of surface material transport is characteristic of a much weaker plasma-surface, as opposed to a laser-surface, interaction. We have noted similar weak fluence dependencies, under plasma-limited conditions, for $BaTiO_3$ film deposition rates *(6)*.

The above arguments all support our conclusion that the fast TOA peak, represented in Figs. 4 and 5, arises primarily from a direct laser-plume interaction process. Over the 4–8 J/cm^2 fluence region, apparently, the major effect of the interaction is to produce a self-regulating limitation of the surface pressure/temperature. The excess laser energy is partitioned between being scattered by the plume/plasma front and

coupling with it, producing a relatively slow increase in highly energetic species and slowly increasing the contribution of charged plasma to the plume. Under the higher fluence conditions, the velocity analyses show that at least a portion of the plume's internal energy increases to a level substantially above the thermal energy imparted at the target surface. The plasma-plume and plasma-surface energy exchange processes, at least for moderate fluences, appear to be much weaker than the direct laser-surface interaction, as evidenced by the very small change in post-expansion beam temperatures generally observed during the early portion of the self-regulated thermal region.

The limitation of the MS intensity observed for the slow peak is believed to mirror a limitation of the surface temperature and consequent *thermally-produced* material evolution. However, further work is needed to completely eliminate collisional effects, such as clustering, from being an atom-limiting factor at higher fluence. The dramatic separation from the faster TOA species indicates that, as long as the thermal process dominates (roughly over the 4–8 J/cm^2 fluence region in the case of Al_2O_3), the laser-plume/plasma interaction should cause only minor perturbations in the thermal portion of the plume. Thus, for the thermal plume and target thermochemical studies discussed below, the fluence should ideally be below the laser-plume interaction threshold, i.e., below about 4 J/cm^2 for the case of Fig. 5. However, the apparent insensitivity of the thermal plume component to excess fluence indicates that this restriction is not essential for most studies.

Cause of Laser-Plume Interaction

The main laser-plume interaction mechanism most likely involves a transfer of photon energy to plasma electrons, Al^+, and Al, via inverse Bremsstrahlung (IB) and electron-ion recombination processes (e.g., *see* pp. 275 and 285 of ref. *29*). At the longer wavelengths used for this study, species number densities required for significant IB interaction are generally believed (p. 118 of ref. *1* and p. 61 of ref. *5*) to be ~ 10^{18}/cm^3. At shorter λ, the minimum number density for significant IB interaction is expected to increase, although other high-photon energy interaction mechanisms may offset the reduced IB effectiveness. Thus, the fast Al+ component, apparently, is generated in the plume and accelerated by plasma coulombic forces. This ion assignment is also supported by the absence of fast TOA peaks for the much higher ionization potential species, AlO, Al_2O, and O. As was the case for the slow Al component, the abundance of AlO remained basically constant over the 4–16 J/cm^2 fluence range. This constancy suggests that AlO also originates at, or near, the surface as a thermal-like species. On the other hand, the Al_2O abundance showed a continued increase with fluence over the same range, perhaps indicating that the Al_2O enhancement is a result of plasma sputtering of the target, or, alternatively, cluster initiation. Moreover, the slow TOA values for these two species indicate that they orig-

inate as neutrals rather than ions, in contrast to the fast Al TOA component. The intermediate TOA feature at 220 μs in Fig. 3, not considered in detail at this time, is tentatively identified as arising from $Al^+ + e^-$ recombination during plume expansion.

A further demonstration of the laser-plume interaction phenomenon is shown in Fig. 6, where enhancement of the fast TOA peak occurs when the laser beam is focused within the plume (above the target) as opposed to at the target surface. Note, however, that the relative intensity of the fast-to-slow peaks is less than for the case of Fig. 4. This observation is consistent with the use of a much shorter wavelength laser than was used in the study of Fig. 5. Use of shorter wavelength photons should reduce the IB plasma absorption coefficient by ~ 70×, from 1064 to 248 nm (*see* p. 118 of ref. *1*). The actual reduction in absorption/ionization is less, because, as the wavelength moves into the UV, direct electronic excitation, molecular absorption, and multiphoton interactions begin to dominate as laser-plume interaction mechanisms.

In addition to plasma-controlled kinetic and internal energy-enhancement effects, laser-plume interactions can lead to photochemical dissociation of molecular species. Compared to the atom concentrations in the plume, we have noted reduced concentrations of certain diatomic species, C_2 (from graphite), BaO ($BaTiO_3$), and AlO (Al_2O_3), for example, at relatively short λ and high E conditions.

Thermal Equilibration

In considering the high temperature chemistry aspects of these plumes, a key question arises: Are there regions, both spatial and temporal, of local equilibrium? A necessary first condition to obtaining, or utilizing, thermodynamic data is the establishment of local thermal equilibration among the various molecular weight (M) species observed *(13)*. This condition is reflected in a linear relationship between the most probable time-of-arrival (TOA), t_{mp}, and $M^{1/2}$, as was found in the MS studies listed in Table 1 (*see also* refs. *14,15*). The slopes of curves showing such a relationship also provided values of T_b *(15)* that were in agreement with those obtained from the Maxwellian probability distribution function fits to the TOA data, further indicating the establishment of translational equilibrium *(6,12,15)*.

For conditions favoring formation of distinctly separate TOA populations of laser-heated and/or plasma-excited plume species (*see* previous section) and slower, thermal-source species of the same mass, there is a clear dichotomy in the velocity distributions. Thus, the different populations must arise from regions not in global thermal (translational) equilibrium. Since even a few collisions are sufficient to establish translational equilibrium, these regions must be separate in space and/or time. Our ability to fit separately each velocity distribution peak to a Maxwell-Boltzmann function implies establishment of *local* collisional (thermal) equilibrium within each of the distinct populations.

Internal Energy States

Because the hierarchy of relaxation times generally follows the sequence:

$$\text{translation} \sim \text{rotation} < \text{vibration} < \text{electronic},$$

the question arises as to the extent of equilibration of the degrees of freedom other than translation. In studies using the TMS technique *(2,3)* to simulate the collisional history and expansion times present in laser plumes, we found evidence in the TMS beam of incomplete relaxation of vibrationally excited states via simultaneous microwave spectroscopy and from analysis of MS measurements of changing fragmentation ratios. More direct evidence for incomplete vibrational relaxation in laser plumes is provided by our observations of the C_2 Swan system ($A\ ^3\Pi_g \rightarrow X^1{}^3\Pi_u$) for laser plumes from graphite. The vibronic structure of this electronic transition showed evidence of incomplete thermalization of vibrational states: vibrational temperatures were 6000–8000 K, whereas rotational temperatures were ~ 4000 K (approximately the translational value) *(20)*. With regard to electronic temperatures, measurements of atomic (e.g., Ag from laser-irradiated Ag targets) resonance line intensity ratios exhibited electronic temperatures > 11,000 K; population inversion limited measurements of higher temperatures in the Ag case.

Chemical Equilibration—Species Concentration and Temperature Determinations

In addition to the demonstration of local thermal equilibration, a second key question involves the extent of chemical, or species concentration, equilibration.

Species Concentrations/Partial Pressures

For systems where the high temperature thermochemical stabilities are reasonably well known, e.g., graphite and boron nitride, we have shown that the species relative and absolute concentrations are consistent with chemical equilibration, at or very near a hot surface, for moderate fluence conditions *(14,21)*. It should be noted that it is generally not possible, based on current experimental approaches and information, to distinguish between surface and "near-surface" chemical or temperature conditions. In fact, the initial process of laser-surface interaction may well be a nonequilibrium one, particularly in view of the ease of transporting stoichiometric vapor for normally non-congruently vaporizing systems. With high fluence conditions (e.g., $\geq$ 10 J/cm^2, for AlN), an explosive release of material appears possible *(11)*. However, for the present cases, with E < 8 J/cm^2, the conditions of temperature, pressure, and chemical reactivity appear to be such as to ensure a very rapid approach to near-equilibrium gas phase conditions close to the surface, at least for the case where laser-plume interactions do not dominate and the laser interacts primarily with the lattice, rather than directly disrupting individual bonds.

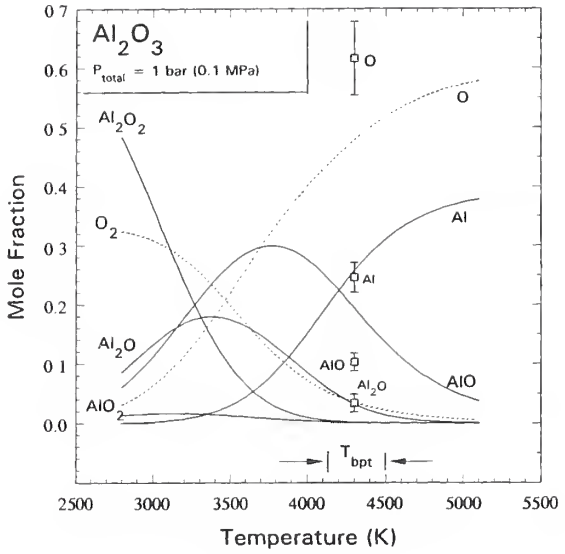

Fig. 7. Comparison of experimental (■) and calculated equilibrium mole fractions (at 1 bar, independent of condensed phase) for vapor species from Al_2O_3 as a function of temperature. The T_{bpt} lines encompass the calculated temperature interval in which the literature normal "boiling" point should fall, based on the thermodynamic data uncertainties. Experimental mole fractions (mf) (■) for Al_2O_3 target (98 + % purity), Nd/YAG laser, λ = 1064 nm, E = 3.8 J/cm^2. Uncertainties in mf result mainly from the estimation of relative ionization cross sections.

Thermodynamic Models

Under so-called chemical equilibrium PLV conditions, we consider the following thermodynamic model to apply: The vapor and condensed phase stoichiometry, on an elemental basis, was constrained to be the same. Thus, for Al_2O_3, the vapor content, regardless of species identities, should be equivalent to 40 mol% Al and 60 mol% O. This stoichiometric constraint was confirmed by MS analysis. With this constraint, we calculated, using literature standard thermodynamic functions *(18a)*, the molar distribution of the various vapor species as a function of temperature at assigned total pressures. Such an approach bypasses consideration of equilibria between the condensed and vapor phase.

An example of this model calculation for Al_2O_3, at an assigned total pressure of one bar, is given in Fig. 7, together with experimental MS results. Note that the MS-based data compare well with the model equilibrium composition when the comparison temperature is taken as 4300 (±200) K. This temperature represents the value where the experimental

mole fraction ratios, AlO/Al_2O, Al/AlO, and so forth, are in agreement with the model values. The expected normal "boiling" point, T_{bpt} (i.e., the temperature where P_{total} = 1 bar) for Al_2O_3 lies in the interval 4150–4500 K, based on the JANAF thermochemical functions for Al_2O_3 vaporization *(18a)*. It appears, given the experimental and literature data uncertainties, that the observed relative partial pressures of species in this system are consistent with a temperature at or near the normal "boiling" point of alumina. This interpretation of equilibrium species molar ratios at the material's normal "boiling" point is consistent with that noted earlier for laser-vaporized graphite and boron nitride *(14,21)*. It is also pertinent that target weight loss measurements *(19)*, obtained at a similar fluence (with allowance made for a difference in laser pulse time), are consistent with a total pressure in the range of ~ 0.3–3 bar.

Although the body of evidence favors the match between experimental and model molar ratios at 4300 K and 1 bar, it should be noted that a second match of ratios can be found at 6000–6300 K and 50 bar—a condition that is also consistent with a saturated vapor in equilibrium with liquid Al_2O_3, based on our extrapolation of the literature thermodynamic functions *(18a)*. In principle, pressures much greater than one bar are possible; however, we believe that the onset of significant laser-plume interaction limits the attainment of much higher effective (i.e., laser pulse time averaged) pressures *in this case*. Further evidence in favor of the lower pressure limit (ca. 1 bar) is presented below (*see* "Surface Pressure Regulation").

Surface Temperatures—Indirect Observations

Resolution of questions concerning chemical equilibration at or near the target-vapor interface requires target surface temperature information that, on the ns time-scale involved, is currently not reliably measurable by conventional (pyrometric) means. For moderate fluence conditions, the presence of persistent, bright, high-energy plume light, the difficulty of quantitatively eliminating laser interference, and the likelihood that the plume itself is optically opaque for most of its lifetime, all mitigate against direct target surface measurements on the laser-pulse time scale. Hence, indirect *(14)* and model (energy balance, e.g., *see* ref. 22 and p. 275 of ref. 29) temperature estimates have usually been made.

Indirect estimates of T_s have been made as follows:

1. For systems where the vaporization thermochemistry is reasonably well known, e.g., C, BN, Al_2O_3, HfO_2, $BaTiO_3$, and so forth, mass spectral observations of the *relative* partial pressures of species have been compared with those calculated from the known thermodynamic functions at various temperatures (and pressures). Because all species from each particular system, e.g. C_1–C_7 for graphite, were found to have relative partial pressures that are quite consistent with a single temperature, it appears likely that a local chemical

equilibrium condition was present and that the thermodynamically indicated temperature (*see* Table 1) was the target or near-surface temperature. For the laser fluence conditions used in the thermal vaporization studies (Table 1), these target temperatures were typically in the region where the material vapor pressure is ~ 1 bar, as calculated from available thermodynamic functions *(18)*. The Al_2O_3 study, summarized in Fig. 7, is a case in point.

2. A check on near-surface plume pressure and rate of material transport from the surface should also be consistent with the T_S values obtained by the above approach and also with our earlier interpretation of a pressure-limiting condition with fluence. A number of determinations of total plume pressures, made by summation of individual species partial pressures obtained via Eq. 1 (e.g., *see* refs. *14,21*), indicated values in the region of 1 bar. Several indirect checks on target material transport rates were made from observed film deposition rates. In isolated cases, direct weight loss measurements have also been made by others, as noted above *(19)*. These direct and indirect mass transport rates were related back to total surface pressure values of about 1 bar, consistent with the other observations already discussed, such as the summation of partial pressures. These mass transport approaches to pressure determination are relatively imprecise, however, because of the difficulty in ascertaining an accurate time interval over which the hot spot continues to vaporize (if at all) after termination of the laser pulse. Where ejection of unvaporized particulates occurs, mass loss attributed to vapor species would be too high, causing P_S to be overestimated. We have observed that surfaces can continue to be visibly hot ($T_S \lesssim 1500$ K) for times typically on the order of a few μs. This observation could be influenced by cases where slow-moving particulate emission is occurring. Also, the visible plume itself appears to remain close to the surface on a similar time scale, as may be seen in Fig. 1, for example. Thus, the plume/plasma could act as an additional source for energy transfer to the surface.
3. Gasdynamic correlations (discussed further in the following section) of measured postexpansion beam temperatures with pre-expansion plume temperatures and then with target surface temperatures (taken as T_{bpt}) also support the other indirect indicators of surface temperatures and the values given in Table 1.

Surface Temperatures—"Direct" Observations

We have recently made more direct temperature observations by examining the surface continuum emission from graphite target hot

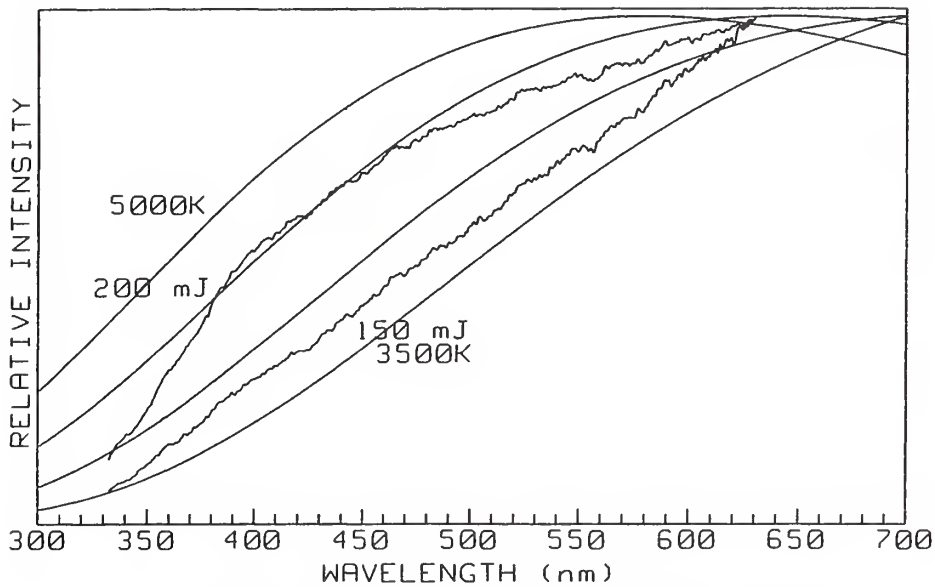

Fig. 8. OMA-based surface temperature measurement (data points) for graphite heated with pulsed (15 ns) Nd/YAG laser, λ = 1064 nm, laser energies 150 mJ (E ~ 1.3 J/cm^2) and 200 mJ (E ~ 1.7 J/cm^2). Detection time (OMA gate duration) 10 ns, OMA gate triggered at the end of the laser pulse. The solid curves are fits made with the Planck blackbody radiation law, at the indicated temperatures. Uncertainties are: laser energy, ±5 mJ; E ±10% relative, ±30% absolute; experimental relative intensities, linear scale (est.) ±5%.

spots. A calibrated OMA was used to obtain broad range relative spectral radiance data for the 10 ns interval following the end of 1064 nm Nd/YAG laser pulses. The wavelength dependence of this emission over the visible ↔ ultraviolet range is shown in Fig. 8. Fits of the emission intensity vs. wavelength curves with Planck's Law (Fig. 8) yielded surface temperature values, at the end of the laser pulse, of 4050 (± 50) and 4590 (± 60) K for the two representative laser fluences. These temperatures are similar to the values obtained earlier *(14,17)* by the indirect approach of method 1, above.

Very recently, Geohegan *(23)* has reported similar emission-based, time-resolved temperature observations made on target-ejected plume particulates for BN and YBaCuO systems; an example of this particulate-producing behavior can be seen in the last frames of Fig. 1. Extrapolation of Geohegan's *(23)* data back to the time of the end of the laser pulse and correcting for the particle radiative cooling observed also indicates target surface temperatures near the T_{bpt} values for the target material. This result is consistent with our own indirect temperature indicators for the BN system *(21)*. One should caution, however, that the comparison is based on the *assumption* that the particulate release mechanism coincides

in time with the main vaporization or vapor ejection process. This assumption appears to be a reasonable approximation, based on current understanding of particulate release mechanisms (e.g., *see* pp. 14, 71, and 160 of ref. *1*) and our extrapolations back in time of particulate trajectories in ICCD images, such as Fig. 1G.

More systematic work on temperature measurements and energy-balance models is obviously needed. However, to date, it appears that pulsed laser-driven vaporization conditions can be established where the species identities and concentrations are at least near to what would be expected for chemical equilibration. We stress, however, that the conditions required to approach chemical (species) equilibrium in laser plumes represent a window, outside of which nonequilibrium processes can be of greater significance.

Gasdynamic Expansion

Whereas plume thermochemistry is of great significance during the initial stage of plume formation, gasdynamic expansion plays a significant role during the plume transport and decay process.

Correlation of Post- and Pre-expansion Temperatures

For an isentropically expanding gas flow, typical of high-pressure gas expanding supersonically into near-vacuum, explicit thermodynamic relationships exist between the pre-and postexpansion conditions *(24)*. These conditions, including pressure, temperature, and density are interrelated through the flow Mach number, defined as the ratio of the local gas velocity to the local speed of sound, and the heat capacity ratio, γ, also referred to as the gasdynamic factor. Accordingly, we might expect to find a correlation between, for example, the measured postexpansion beam temperature and the pre-expansion plume temperature *(15)*. Knudsen layer theory predicts a direct relationship between plume temperature and T_s, although the derived relationship appears to only be qualitative (e.g., *see* p. 55 of ref. *(1)*). Hence, it is reasonable to expect a simple relationship to hold between T_b and T_s. The following expression can be derived from the isentropic relationships mentioned above:

$$T_b / T_s = [P_b / P_s]^{(\gamma-1)/\gamma} \Leftrightarrow T_s = f(P_b / P_s, \gamma) \times T_b \ , \qquad (2)$$

where P_b/P_s, defines the post- to pre-expansion ratio. Under our conditions, the expansion process "freezes-in" when the beam pressure reaches about 5×10^{-5} bar because collisions effectively cease. Thus, the expansion ratio can provide a measure of the source pressure. The discussion above regarding the strongly limited behavior of the thermally emitted vapor (*see* "Self-Regulation of PLV"), together with Eq. 2, indicates that a simple relationship between T_b and T_s should exist for different materials and/or λ's if a regulating condition controls P_s, and γ is constant. Figure 5 shows, for λ = 1064 nm, the presence of a limiting effect, interpreted to occur over a pressure interval of ~ 1–10 bar.

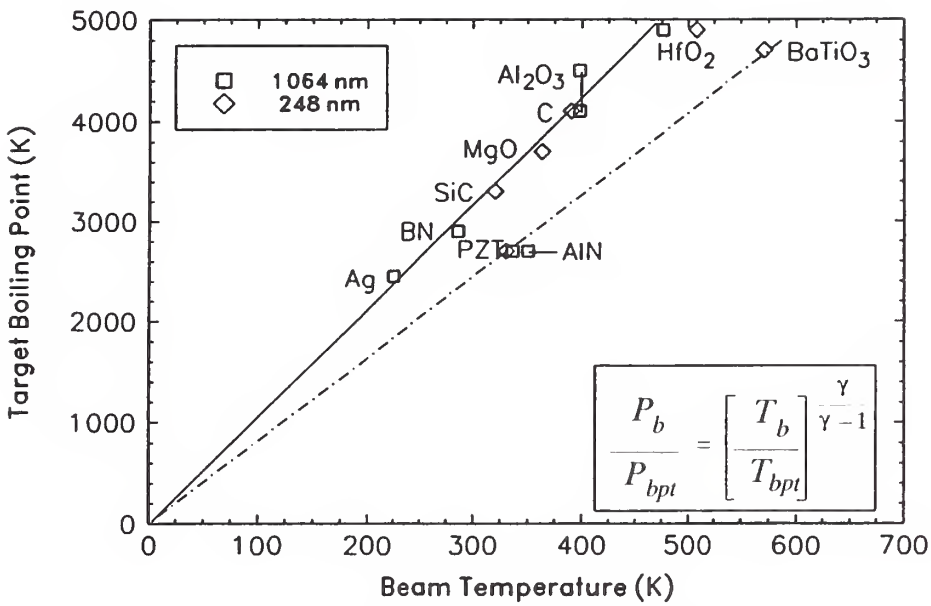

Fig. 9. Gasdynamic correlation test showing linear relationships between target material normal "boiling" point (T_{bpt} at 1 bar) and measured expanded plume translational beam temperature (T_b). Note for Al_2O_3 at 1064 nm, AlO was used to obtain T_b. Data symbols indicate various laser λs. Similar data (not shown) to that at 1064 nm were also observed at 532 nm. Typically, for 1064 nm points, fluence was set just below the threshold for visible plume emission. Uncertainties are estimated as typically ≤ ± 4% in T_{bpt} and ± 10% in T_b.

Surface Pressure Regulation

We selected $T_s \approx T_{bpt}$ as an approximate surface (or near-surface) temperature to test for the presence of a material-independent regulated condition for P_s implied in Eq. 2. Figure 9 shows the degree of correlation existing between T_{bpt} and T_b for a variety of materials and even different laser sources (with markedly different λ and τ). Values of T_{bpt} were determined mainly from an evaluation of available literature thermodynamic data (cf. ref. *18*) for the condition of excess condensed material in a sealed, evacuated isothermal volume with condensed and vapor phase in equilibrium at unit accommodation coefficient. For $BaTiO_3$ and PZT (*see* Table 1), a more detailed evaluation of the general literature was required *(25)*. The solid curve represents a fit to systems where the moderate laser fluence conditions used favored predominately thermal vaporization gasdynamic processes. The dashed curve applies to higher fluence (~ 8–15 J/cm^2) studies where domination of local pre-expansion plume heating and plasma effects, because of laser-plume interactions

already noted above, raised the effective pre-expansion plume temperature well above the near-surface vapor temperature. Also, higher T_s and P_s values (> T_{bpt}) cannot be ruled out in these cases.

The fact that data obtained for a variety of materials, laser wavelengths, and fluences follow the simple linear relationship of Eq. 2, as shown in Fig. 9 (solid curve), suggests that each system:

1. probably reaches a plume state with similar "effective" γ;
2. has a similar expansion ratio (P_b/P_s);
3. has thermal P_s values, by virtue of sufficient near-surface collisions to produce a local thermal equilibrium; and
4. has similar P_s values that appear to be regulated by some controlling process.

The first condition is quite sensitive. The presence of the plasma, driven by the laser-plume interaction, can make available sufficient additional degrees of freedom to significantly reduce the value of γ to below the range 1.67–1.4 for mixtures of predominately atomic and diatomic neutral species. For the assigned pressure of 1 bar in Fig. 9, we find $\gamma = 1.29 \pm 0.04$. The uncertainty range in P_s, for this effective uncertainty range, is 0.95 ± 0.3 bar, about a factor of 2×, assuming a constant terminal expansion pressure of 5×10^{-5} bar. Thus, if $T_s \neq T_{bpt}$, there would need to exist an additional proportionality of unknown nature between T_s and T_{bpt} to yield this correlation among various material systems. In particular, the apparent constancy of P_b/P_s and γ further restricts such a proportionality to also yielding proportional pressures.

It should be noted that the experimental establishment of similar target vapor-pressure conditions for the various materials could have a systematic bias. For the 1064 nm studies in Fig. 9, the laser fluence was adjusted to just below the threshold for visible plume formation. It should also be noted that some of these data have been collected over a period of several years, with many different optical components and arrangements, substantial changes in laser-target and target-MS geometries, and with large changes in target region base pressure. None of these factors appear to have caused any major change in the correlation, other than the effect attributed here to super-heating of the plume gas by the laser-plume interaction.

In addition to the imposition of an external governing effect on system energy, there also appears to be an internal governing effect that limits the near-surface plume pressure or number density, particularly, but not exclusively, at longer laser wavelengths. This governing effect is evident from the observation of similar MS signal intensities, even with significant changes in laser fluence. A likely governing mechanism is the onset of the laser plume interaction. Figure 5, for instance, depicts a case where such a limiting effect on the thermally-produced vapor appears to

be present; e.g., at E > 4 J/cm^2. Beyond this interaction threshold, any additional increase in fluence tends to interact primarily with the plume, and naturally regulates the rate of increase and the maximum plume pressure to equivalent number densities of about 10^{18-19}/cm^3.

This interpretation of the observed T_b vs. T_{bpt} correlation is also consistent with the other indications already discussed (*see* "Species Concentrations/Partial Pressures"); i.e., the P_s values produced in all the lower-fluence systems of Fig. 9 were all in the region of 1 bar. This apparently limiting condition is not necessarily a universal one. Some variation should be expected with different materials and, particularly, laser wavelengths. Thus, for the lower fluence systems considered in Fig. 9, we cannot, for the present, rule out near-surface pressure variations within the range, $P_s \sim 0.1$–10 bar.

Surface/Near-Surface Pressures and Temperatures

Few systems have been calibrated to date (by any laboratory) in terms of quantitative species concentrations, pressures, or material removal rates (*see also* "Surface Temperatures—Indirect Observations" and Surface Temperatures—"Direct Observations" and ref. *30*). Thus, the question of near-target vapor phase conditions is, in general, argumentative.

A recent piezoacoustic device measurement (p. 101 of ref. *5*) of recoil forces at the target (high T_c YBaCuO material at 248 nm) was interpreted to indicate that surface pressures up to several hundred bar are possible at relatively high laser fluences (at 100x their pressure detection E threshold). These elevated pressures suggest that near-surface temperatures could approach the critical state values, provided the target material-ejection process is of a thermodynamic nature. However, as we have stressed in the present study, at higher laser fluences, laser-plume interactions and plasma effects become very significant. Their effect on target recoil force measurements may require consideration, particularly when converting the observed impulse to an apparent surface vapor pressure (*see also* p. 394 of ref. *29*). Also, the proportionality between P_s and T_s, for a given number density (η) may be a factor in higher energy plumes. As an example, consider a representative plasma energy condition of 45 eV (*see* ref. *20*), with η appropriate to $P_s \sim 1$ bar and $T_s \sim 4300$ K. Heating of the vapor by thermal transfer of the plasma energy would then lead to $P_s \sim 100$ bar. In this instance, target weight loss, deposition rate, and MS observations would all be consistent with the thermally produced 1 bar, 4300 K near-surface condition. "Observation" *(23)* of T_s values appropriate to $P_s \sim 1$ bar for YBaCuO at E appropriate to $P_s \sim 300$ bar (p. 101 of ref. *5* from the piezoacoustic measurements) would appear to support this hypothesis (*see also* ref. *30*). Other instances appear feasible where high values of η could indeed occur, more appropriate to $P_s \sim 300$ bar but still with $T_s \sim 4300$ K. These cases could occur by volume expulsion of target material (e.g., *see* ref. *11*), similar to the prompt particulate ejection

processes we have discussed, with subsequent laser or plasma vaporization from these very high surface areas. Thermomechanical rather than thermodynamic models would probably be more appropriate descriptions of these events.

Recent energy balance calculations *(29)*, with IB-type laser-plasma interactions taken into account, indicated the possibility of transient high pressure (~ 200 bar) "spikes" of a few ns duration during a longer (30 ns), relatively high fluence laser pulse. However, the overall pressure was calculated to be far less (~ 1 bar) over most of the pulse time, owing to the self-regulating behavior of the plasma. For the case of Ag at 2 J/cm^2, model calculations *(22)* without laser-plume interaction indicated a maximum pressure, P_s ~ 1 bar. For the present case of Al_2O_3 at 12 J/cm^2 application of plasma-surface interaction model relationships (p. 61 of ref. 5) indicated that *impulse* pressures as high as ~ 100 bar could result. However, we estimate, from film deposition rates and the consideration of self-limiting conditions, the limiting surface pressure as P_s ~ 10 bar, under our conditions where laser reflection and other losses were apparent. We obtain a similar limiting pressure value from an analysis of target weight-loss data *(19)*.

If very high P (>> 1 bar) and T (>> 4300 K) conditions were actually present in these studies (e.g., the moderate fluence case of Fig. 9), then one would need to infer the following: Suppose T_s and P_s are near their critical point values, rather than at the normal "boiling" point; for instance, P_s ~ P_{crt} ~ 200 bar instead of 1 bar and T_s ~ T_{crt} ~ 8000 K instead of 4000 K. Under these conditions, thermodynamic calculations indicate that molecular species are of considerably lesser significance than at the normal "boiling" point *(25)*. The observations presented here would then require that, during the initial stages of plume expansion (~ 100 ns), the atomic species present undergo extremely fast chemical kinetic transformations to form the molecular species that are observed experimentally (e.g., *see* Table 1). Moreover, these chemical transformations would (fortuitously!) need to cease at a composition consistent with the normal "boiling" point T and P condition (or some other interim condition, noted for Al_2O_3 as 50 bar, 6300 K) in order to agree with our observations of species partial pressure ratios. Thus, the correlation of Fig. 9 would need to apply to an initial condition not present at the surface but at a particular expanding plume location at a distance several μm from the surface. The final condition would then be the result of expansion from the condition present at this near-surface, partially expanded, kinetically frozen location. We have recently demonstrated *(25)* that a modest composition shift resulting from chemical kinetic processes appears feasible under these near-critical conditions (*see also* "Gas Kinetic Reactions"). However, it appears unlikely that such a situation could occur concertedly for all of the systems represented in Fig. 9, where material type, E, λ, τ, and spot size were all varied. Also, the other arguments given above strongly support much lower values of T_s and P_s.

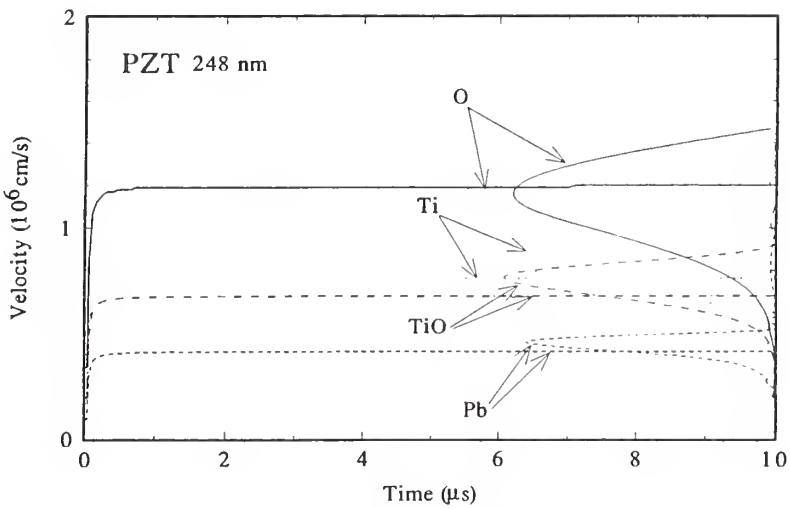

Fig. 10. Comparison of gas dynamic superheated plume model velocities (vs expansion time) with experimentally-based MS velocity distribution profiles (RHS) for various plume species. Excimer laser, λ = 248 nm, E = 30 ± 10 J/cm^2; target, PZT (lead zirconate titanate); model conditions: T_S = 2700 K, T_P = 22,000 K, γ = 1.3, spot size ~ 0.005 ± 25% cm^2. Estimated uncertainties in experimental velocity distributions (RHS scale) are ±10% within an individual species profile, and ±20% among different species.

Gasdynamic Models

It is clear from the effects of increased laser fluence on plume species velocity distributions spectral emission, beam temperatures, and electronic level temperatures, that a general gasdynamic description of the plume expansion process requires consideration of plume temperatures well in excess of target surface temperatures. Recently, Singh et al. utilized a modeling algorithm that allowed for separate consideration of surface and plume temperatures in the gas dynamic flow problem *(26)*. We adapted this approach to our particular plume conditions and found good agreement between model and experimental plume front positions determined by ICCD imaging, both in space and time *(6)*. Good model agreement was also found with the mass spectrometrically determined most probable velocities, as shown by the example in Fig. 10. Depending on the laser fluence, wavelength, and target material, model plume temperatures that were required for good agreement with experimental velocity data for neutral species ranged from near T_S (~ 4000–5000 K) to values of 10,000–70,000 K or greater. These super-heated plume temperatures were also found to be consistent with observed line ratio electronic temperatures and also with the observed beam Mach numbers, expansion temperatures, and gasdynamic relations. Thus, the gasdynamic

models support the other evidence presented concerning laser-plume interaction heating and its consequences.

Gas Kinetic Reactions

By coupling the gasdynamic model and mass spectrometric results, information on plume species number densities and temperatures has been obtained as a function of time and distance, particularly during the adiabatic expansion process. We have used such information as input to gas kinetic calculations involving elementary reactions between the various uncharged vapor species *(25)*.

The elementary reaction scheme selected to represent Al_2O_3-derived plume kinetics is summarized in Table 2. Using this scheme with an initial pre-expansion condition of 4300 K and one bar, and with allowance made for real-time adiabatic expansion, we calculated time-dependent chemical compositions for Al-O vapor species, as shown by curves in Fig. 11 *(25)*. Note that significant compositional changes are predicted to occur, particularly during the first $t \sim 40$ ns of expansion. The reported (27) appearance of a delayed emission (20 ns following the laser pulse) for YO relative to Y in plumes from YBaCuO may be further evidence of plume chemistry ($Y + O \Rightarrow YO$), at least during the initial stage of plume formation. Also note in Fig. 11 that the experimental species mole fractions agree with the kinetic model curves only at a very short expansion time ($t \lesssim 20$ ns). Such an observation suggests that the plume expansion has resulted in a sudden-freeze condition, with respect to chemical relaxation, on the same time scale. The gas dynamic calculations indicate a pressure reduction (and consequent reduced collision and reaction rates) of a factor of ~ 20 and a temperature reduction factor of ~ 2 over the first 20 ns of expansion. Such a pressure and temperature reduction greatly reduces the reaction rates and should lead to the early freeze-in of species mole fraction ratios shown in Fig. 11. That the model predicted freeze-in condition occurs around $t \sim 100$ ns, rather than the experimental indication of $t \sim 20$ ns can be explained on the following basis:

1. Uncertainties in estimated rate constants *(25)*.
2. Model selected expansion conditions were too slow.
3. Unaccounted-for laser photodissociation losses of AlO and Al_2O; we have noted such effects at lower λ and higher E than those used for the study of Fig. 11.

Calculations, similar to those of Fig. 11, were also made at higher pressures and temperatures *(25)*, where the chemical kinetic compositional shift was calculated to be more pronounced, as expected. At pressures of $P_s \gtrsim 50$ bar and temperatures $T_s \sim 6000$–7500 K, molecular O_2 and Al_2O_2 were predicted to be present at concentration levels readily detectable with our MBMS apparatus. That we did not detect these species, at E = 3.8 J/cm^2, is consistent with our earlier argument con-

Table 2.
Chemical Kinetic Reactions in Plumes Over Al_2O_3

$O + O + X^a$	=	$O_2 + X$
$Al + O + X$	=	$AlO + X$
$AlO + AlO$	=	$Al_2O + O$
$AlO + AlO$	=	Al_2O_2
$AlO + AlO + X$	=	$Al_2O_2 + X$
$AlO + Al$	=	Al_2O
$AlO + O$	=	$Al + O_2$
$AlO + O_2$	=	$AlO_2 + O$
$Al + O_2 + X$	=	$AlO_2 + X$

[a]X represents a general nonreactive gas collision species, involved in a three body reaction

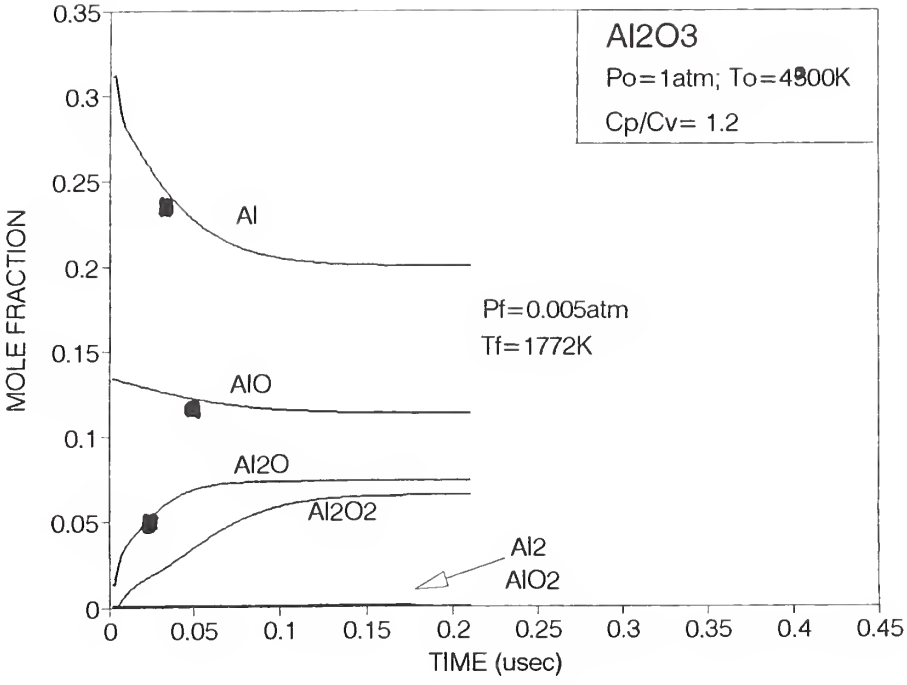

Fig. 11. Comparison of experimental mf data (■, conditions same as for Fig. 7) with gas kinetic model predictions of Al_2O_3 system species steady-state mole fractions (mf) as a function of plume expansion time; initial conditions: calculated thermodynamic equilibrium composition at T = 4300 K, P = 1 bar, and γ = 1.2. The terminal (no further compositional change with time) conditions were 1773 K and 5×10^{-3} bar. Estimated uncertainties are: kinetic model, ±5% in relative mf and ±30% among different species; experimental mfs, ±10%, unless otherwise indicated. Other species considered (AlO_2, O_2, Al_2) are present at concentrations too low to appear on the mole fraction scale.

cerning maximum local equilibrium plume pressures being in the region of 1 bar, rather than at $\geqslant$ 50 bar. However, with regard to the major species, Al, O, AlO, and Al_2O, we find that comparisons between the kinetic model and experimental MS species molar ratios cannot be used to uniquely define the source conditions of P_S and T_S. At $P_S \sim 50$ bar and $T_S \sim 6300$ K, a second comparison match (i.e., similar to Fig. 11) exists at $t \sim 20$ ns, corresponding to a kinetic freeze-in condition of ~ 1 bar and ~ 4500 K! Arguments against this alternative case, in addition to the absence of detectable O_2 and Al_2O_2, were made earlier (*see* "Surface/ Near-Surface Pressures and Temperatures").

CONCLUSIONS

From the examples considered here, it is clear that laser plumes provide a unique opportunity for observation and utilization of high temperature chemistry under extreme conditions. The following picture appears to best describe the high temperature chemical behavior of laser-induced plumes. Laser fluence and, secondarily, wavelength appear to be major determining factors in defining the overall plume character. For PLV processes, as opposed to laser desorption, sputtering, or ablation, there exists a useful window of fluence and wavelength where the main plume vapor species can be represented by local thermodynamic equilibrium considerations, at least for vaporization into high vacuum. For neutral species, rapid elementary reactions can occur on a time scale similar to that of the laser pulse duration, thereby establishing, or maintaining, a local chemical as well as translational equilibrium over a wide range of fluence conditions. If the laser fluence is low to moderate, then one can describe the system a priori using vaporization and chemical equilibria, and a surface/near-surface condition approximated by the material's normal boiling point pressure and temperature appears to be favored, particularly at longer wavelengths. This feature of PLV has proven to be uniquely useful in extending the upper measurement limit of temperature and pressure for vaporization equilibria, particularly for refractory materials. Likewise, one can utilize existing thermodynamic data to model or simulate PLD vaporization conditions. We anticipate extending these results on plume neutrals chemistry to include consideration of plume ion chemistry in future studies.

As the fluence is increased beyond a threshold, e.g., about 4 J/cm^2 for Al_2O_3, a self-limiting condition manifests itself. A restriction in vapor production rate is observed for many refractory systems, with *typical* local equilibrium near-surface pressures apparently in the region of 1–10 bar. This restriction may be attributed, at least in part, to laser-plume interaction effects that increasingly (with E) render the plume opaque with respect to further laser transmission to the surface. The developing plasma nature of the plume appears to be the determining factor, and the

use of longer λ (e.g., 1064 vs 532 or 248 nm) radiation favors interaction with the plume, in keeping with the wavelength dependence of the more important plasma absorption coefficients. At shorter λ, multiphoton excitation becomes important, and broad molecular-specific absorptions can also render the plume opaque. Consideration of the various laser-plume interaction modes suggests that the limiting condition is number density-based, but, at present, there are insufficient data to correlate the limiting condition with detailed interaction models. At least where the plasma component does not significantly heat the plume neutrals, it appears that the self-limiting condition also allows for existence of a local equilibrium state. This limiting state has a characteristic pressure/temperature/number density that appears able to serve, in the absence of more accurate direct determinations, as a fiducial point (or at least a narrow span) for ultra-high temperature thermochemical measurements via PLV.

There appears to be a dichotomy of evidence and viewpoints concerning the moderate fluence conditions of temperature/pressure/number density, at, or near, the target surface. We have offered several explanations, including the possibility that, in special cases, relatively low values of T_S ($\sim T_{bpt}$) may be present even for high values of P_S ($P_{bpt} < P_S \lesssim P_{crt}$). In such cases, P_S and T_S cannot be thermodynamically linked; i.e. PLV conditions do not apply. Many factors contribute to the lack of definitive evidence for P_S and T_S. For instance, the related mass transport rates are found to vary over a wide dynamic range and sometimes with a nonmonotonic dependence on fluence. Accurate determinations of fluence from target spot size are difficult, and mass transport rates can vary with spot size, even at the same fluence. Thus, intercomparing observations among laboratories and among systems, with nominally similar fluence, may not always be reliable. Clearly at issue is the need for a controlled more quantitative study of the conditions of pressure and temperature at, or very near, the target surface. This issue becomes of particular importance where the plume becomes more plasma-dominated and interferes with laser transmission to the surface—conditions of great significance to PLD applications.

REFERENCES

1. Chrisey, D. B. and Hubler, G. K., (eds.), *Pulsed Laser Deposition of Thin Films*, Wiley, New York, (1994).
2. Hastie, J. W. and Hager, J. P., Vapor transport in materials and process chemistry, in *Proc. The Elliott Symposium on Chemical Process Metallurgy* Iron and Steel Soc., Warrendale, PA, (1990), p. 301.
3. Hastie, J. W., Bonnell, D. W., Transpiration mass spectometry: a new thermochemical tool, in *Thermochemistry and Its Applications to Chemical and Biochemical Systems*, Ribeiro da Silva, M. A. V. (ed.), Reidel Publishing, Boston, MA, (1984), p. 183.

4. Braren, B., Dubowski, J. J., and Norton, D. P. (eds.) *Laser Ablation in Materials Processing: Fundamentals and Applications, MRS Proc.* **285,** The Materials Research Society, Pittsburgh, PA (1993).
5. Fogarassy, E. and Lazare, S. (eds.) *Pulsed Laser Deposition: Basic Mechanisms and Applications*, Elsevier, Amsterdam, the Netherlands (1992).
6. Hastie, J. W., Bonnell, D. W., Paul, A. J., and Schenck, P. K. Gasdynamics and chemistry in the pulsed laser deposition of oxide dielectric thin films, *MRS Proc.* **334,** The Materials Research Society, Pittsburgh, PA (1994), p. 305.
7. Schenck, P. K., Hastie, J. W., Paul, A. J., and Bonnell, D. W. Imaging and modeling of pulsed laser thin film deposition plumes, *Opt. Eng.*, in press (1995).
8. Schenck, P. K., et al., *In Situ* monitoring in the pulsed laser deposition of ferroelectric thin films, *MRS Proceedings*, **361,** The Materials Research Society, Pittsburgh, PA (1995) (in press).
9. Hastie, J. W., Bonnell, D. W., Paul, A. J., and Schenck, P. K. Species temporal and spatial distributions in laser ablation plumes, *MRS Proc. 285,* loc cit. [4], p. 39.
10. Predtechensky, M. R., Bulgakov, A. V., Mayorov, A. P., and Roshchin, A. V., *Appl. Supercond.*, **1**, 1995 (1993).
11. Kelly R., Miotello, A., Mele, A., Giardini, A., Hastie, J. W., Schenck, P. K., and Okabe, H., Gasdynamic effects in desorption and sputtering processes: evidence for a phase explosion with AlN, *Proc. of the Conf. on Desorption Induced Electronic Transitions*, Krakow, Poland October (1994), in press.
12. Schenck, P. K., Bonnell, D. W., and Hastie, J. W., *High Temp. Sci.* **27**, 483 (1990).
13. Hastie, J. W., Bonnell, D. W., and Schenck, P. K., Molecular basis for laser-induced vaporization of refractory materials, *NBSIR 84-2983*, National Tech. Information Service, Washington, DC. (1984).
14. Hastie, J. W., Bonnell, D. W., and Schenck, P. K., *High Temp. High Press.*, **20**, 73 (1988).
15. Hastie, J. W., Paul, A. J., and Bonnell, D. W. Free-jet mass spectrometry of laser ablation plumes in thin film deposition, *Specialists Workshop on Applications of Free-Jet Molecular Beam Sampling*, Estes Park, CO., Oct. 12–14, 1994; in press (NREL/DOE, 1995).
16. Walkup, R. E., Jasinski, J. M., and Dreyfus, R. W., *Appl. Phys. Lett.*, **48**, 1690 (1986).
17. Bonnell, D. W., Schenck, P. K., and Hastie, J. W., Laser induced vaporization time resolved mass spectrometry of refractories, *Proc. Int. Symp. Laser Processing for Microelectronic Application* The Electrochemical Society, Pennington, NJ (1987).
18. (a) Chase, M. W., Jr., Davies, J. R., Downey, Jr., J. R., Fruirip, D. J., McDonald, R. A., and Syverud, A. N., *JANAF Thermochemical Tables, Third Edition*, ACS & AIP, Washington, DC, reprinted from *J. Phys. Chem. Ref. Data* **14,** suppl. 1, (1985).
(b) Gurvich, L., et al., *Thermodynamic Properties of Substances*, Izvesta <<Nauka>>, Moscow, Russia, (1979).
19. Funken, J., et al., *Surface and Coatings Technology*, **52,** 221 (1992).
20. Schenck, P. K., Bonnell, D. W., Hastie, J. W., Cook, L. P., and Chiang, C. K. Optical characterization of thin film laser deposition processes, #1594-41 in *Process Module Metrology, Control, and Clustering*, C. J. David, I. P. Herman, and T. R. Turner (eds.), SPIE Proceeding Series Vol. 1594, p. 411–417 (1992).

21. Hastie, J. W., Bonnell, D. W., and Schenck, P. K., *High Temp. Sci.*, **25,** 117 (1988).
22. Veiko, V. P., et al., *J. Phys. D: Appl. Phys.*, **13,** 1565 (1980).
23. Geohegan, D. B., Imaging and blackbody emission spectra of hot particulates generated during laser ablation, *AIP Conf. Proc. 288,* Am. Inst. Phys. (1994), p. 407.
24. Owczarek, J. A., *Fundamental of Gas Dynamics* International Textbook Co., Scranton, PA, (1964), p. 159
25. Yeheskel, J., Bonnell, D. W., Paul, A. J., and Hastie, J. W. Gas phase chemical equilibrium and kinetic models in pulsed laser evaporation of high temperature materials, *8th Int. Conf. High Temp. Materials Chemistry, IUPAC,* Vienna, April 4 (1994). To be published.
26. Singh, R. K., Holland, O. W., and Narajan, J., *J. Appl. Phys. 68,* 233 (1990).
27. Wu, X. D., Dutta, B., Hegde, M. S., Inam, A., Venkatesan, T., Chase, E. W., Chang, C. C., & Howard, R., *Appl. Phys. Lett.* **54,** 179 (1989).
28. Rosenfeld, A., Mitzner, R., and Konig, R. Spectroscopic investigations of the ablation plume of several inorganic materials, in *MRS Proc.* **285,** loc cit. [4], p. 123.
29. Dreyfus, R. W., Phipps, C., and Vertes, A. Extending laser fusion concepts into the lower power microelectronics arena, in *Laser Ablation: Mechanisms and Applications - II,* J. C. Miller and D. B. Geohegan (eds.), AIP Conf. **288** (1993), p. 285 (*see also* p. 275 ibid.)
30. The sparse literature on higher fluence etch and deposition rates is inconclusive; e.g., for YBaCuO, indicated pressures span the range $200 < P_S < 10$ bar for apparently similar conditions; cf.
    a. Inam, A., Wu, X. D., Venkatesan, T., Ogale, S. B., Chang, C. C., and Dijkkamp, D., *Appl. Phys. Lett.* **51,** 1112 (1987); and
    b. Muenchausen, R. E., Hubbard, K. M., Foltyn, S., Estler, R. C., Nogar, N. J., and Jenkins, C., *Appl. Phys. Lett.* **56,** 579 (1980).
31. Rosen, D. I., Mitteldorf, J., Kothandaraman, G., Pirri, A. N., and Pugh, E. R., *J. Appl. Phys.* **53,** 3190 (1982). Surface Al pressures required for plasma ignition under our conditions of E and τ, but at shorter λ, are indicated as $P_S < 10$ bar. At 1064 nm we can therefore expect $P_S \approx 1$ bar.

APPENDIX C

* Presented at *Specialists Workshop on Applications of Free-Jet Molecular Beam Sampling*, Estes Park, CO. (US DOE National Renewable Energy Laboratory, October 12-14, 1994,)

Free-Jet Mass Spectrometry of Laser Ablation Plumes in Thin Film Deposition*

John W. Hastie, Albert J. Paul, and David W. Bonnell

Materials Science and Engineering Laboratory, NIST
Gaithersburg, MD 20899

INTRODUCTION

Plumes generated by high-power pulsed (10 — 30 ns) laser vaporization or ablation of refractory materials can attain ultra-high temperatures (5,000 — 30,000 K) and relatively high pressures (>1 bar = 10^5 Pa). However, plume expansion into a vacuum is sufficiently rapid that the initial species information can be retained and representative sampling with molecular beam mass spectrometry (MBMS) can be achieved. In order to verify and supplement the MBMS results, complementary investigations using emission spectroscopy and real-time imaging, coupled with gasdynamic, thermodynamic, and gaskinetic models are also carried out. In addition to plume species identities and abundances, MBMS analysis also provides beam time-of-flight information, yielding velocity distributions and gas temperatures. MBMS applications are considered here for systems important in thin film processing, such as Al_2O_3 and C. Attention is also given to the essential features required of a free-jet MBMS system for representative sampling of laser ablation plumes.

Significant progress in defining the general nature of laser vaporization/ablation plumes, used for thin film deposition, has been made in recent years (1). Our current understanding of the main plume features are summarized by the idealized schematic of Fig. 1. As shown, the plume initiates at the laser focus spot on the target surface and moves away along an axis normal to the target (*i.e.* to the right in Fig. 1). After a few ns time delay from the onset of the laser pulse, sufficient vapor density develops for collisional local equilibrium ("loc. eq." in Fig. 1) to become established, followed by a supersonic adiabatic expansion process. This expansion process is isentropic and rapidly leads to a free-flight, collision-free condition. In the present work, species are sampled from this free-flight region for MBMS analysis (note orifice shown at the extreme right in Fig. 1).

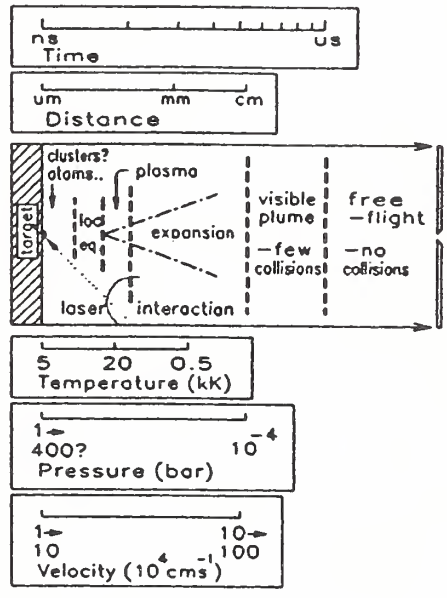

Figure 1 — Laser vaporization/ablation schema

APPARATUS

Laser vapor plumes are particularly complex, and their detailed characterization is not amenable to a single measurement technique. Hence, a variety of *in situ*, real-time monitoring devices are used, as discussed elsewhere (2). These techniques involve rapid (ns-time scale) video imaging and spectroscopic analysis, using photodiode linear arrays and two-dimensional CCD (charge-coupled-device) array detection, in addition to MBMS analysis.

Here, we consider application of the MBMS technique. Fig. 2 shows, schematically, the main features of the apparatus developed for this purpose. This system has high speed differential

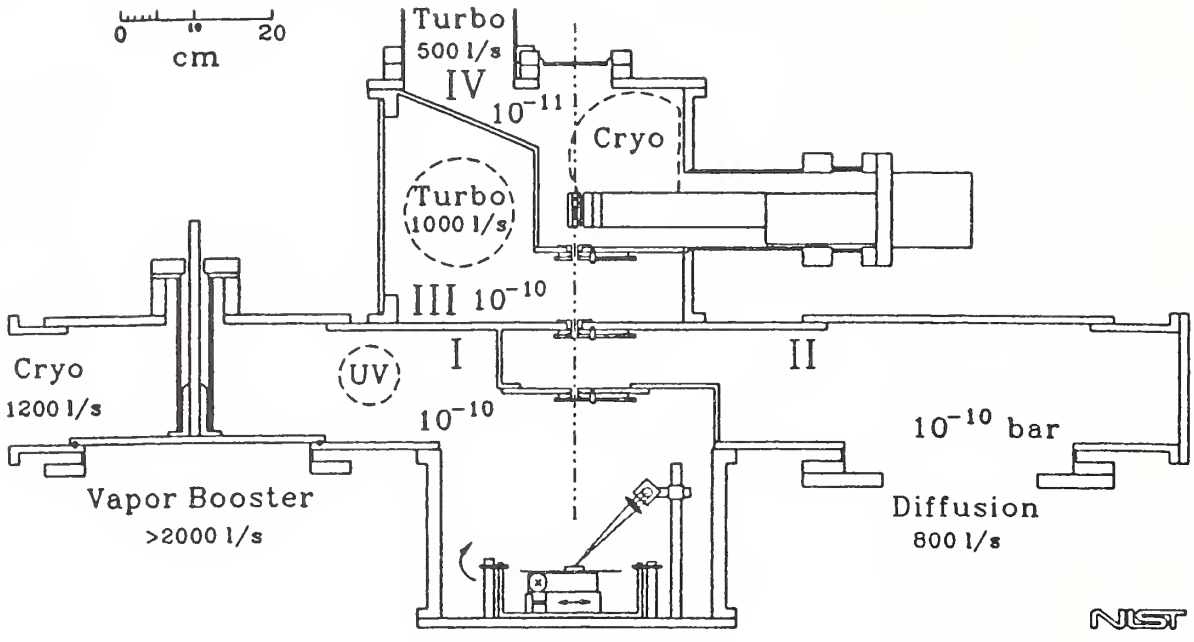

Figure 2 — Laser vaporization/ablation molecular beam mass spectrometer

pumping to allow for rapid free-jet expansion and representative sampling of the expanded vapor. Because of the high temperatures and velocities accompanying laser plumes, coupled with the differential pumping requirement, the distance between the plume and the mass spectrometer ion source has been made relatively long (47.9 cm). As will be shown, this distance allows for sufficiently long flight times to permit observation of velocity distributions over the range of 10^4 to $> 10^6$ cm s^{-1}, which is characteristic for expanded plumes.

RESULTS AND DISCUSSION

Results from a few representative investigations are presented here to demonstrate application of the MBMS technique to laser plumes. Table 1 indicates the variety of materials studied by us and lists the identities of the dominant plume species. It is noteworthy that no evidence of cluster species, present in the plume or formed in the expansion cooling process, was found in these studies. For the most part, the species observed are those we predict from their thermochemical stabilities for conditions near the atmospheric boiling points of the target materials (3-5).

Velocity Distributions In a typical experiment, the mass spectral intensity (I) of each species is monitored as a function of time-of-arrival (TOA) at the detector, relative to the termination of the laser pulse. Fig. 3 shows an example for Al produced by 1064 nm Nd/YAG laser interaction (~10 ns pulse) with an Al_2O_3 target at a moderate fluence. The intensity scale (I') has been corrected for the velocity (v) discrimination associated with the density detection nature of the electron impact ion source. As we have shown elsewhere (2), an appropriate velocity distribution [P(v)] model in this case is that of a full-range Maxwellian distribution referenced to a center-of-mass net flow or drift velocity (u):

$$P(v_z) \propto v_z^3 \exp[-(m/2kT_c)(v_z-u)^2]. \qquad [1]$$

The z axis is the molecular beam axis (see Fig. 2); T_c is the local terminal gas temperature at the onset of collisionless flow; m is molecular mass and k is the Boltzmann constant. In practice,

Table I. Species identified in laser ablation plumes

Material	Application	Atoms	Ions (M^+)	Molecules
Nd/YAG Laser:				
C	Thermo at 4000 K	C	C_{1-3}	C_2 - C_9
BN	Thermo at 2800 K	B, N	-	B_2, B_3, BN, N_2
SiC	Thermo at 3500 K	Si, C	-	SiC, Si_2C, SiC_2, Si_2, Si_3, C_2, C_3
HfO_2	Thermo at 4900 K	Hf, O	Hf, HfO, HfO_2	HfO, HfO_2
MgO	Thermo at ~3300 K	Mg, O	-	MgO
$BaYCuO_x$	High T_c films	Ba, Cu, O	Ba, Cu	CuO, O_2, BaY
Ag/Fe_3O_4	Plasma study	Ag, Fe, O	Ag, Fe, O	-
$BiPbCaCuSrO_x$	Plasma Study	O, Cu, Pb, Ca, Sr	Cu, Ca, Sr	CuO, SrO, CaO
Al_2O_3	Thermo at 4000 K	Al, O	-	AlO, Al_2O
Pb_2ZrTiO_6	Ferroelectric Films	Pb, Zr, Ti, O	Pb, Zr, Ti	PbO, ZrO, TiO, ZrO_2, TiO_2
Eximer Laser:				
Ag/Fe_3O_4	Nanostr. mag. films	Ag, Fe, O	Ag, Fe	-
Pb_2ZrTiO_6	Ferroelectric films	Pb, Zr, Ti	Pb, Zr, Ti	ZrO, TiO
$BaTiO_3$	Dielectric films	Ba, Ti, O	Ba, Ti	BaO, TiO, TiO_2
$BaYCuO_x$	High T_c films	Ba, Y, Cu	Ba, Y, Cu	YO
$BiPbCaCuSrO_x$	High T_c films	Pb, Bi, Ca, Cu, Sr	(to be analyzed)	(to be analyzed)
AlN	thermal	Al, N	AlN, N	AlN
Al_2O_3	thermal	Al, O	-	AlO, Al_2O

as the experimental data are obtained (initially) in time rather than velocity space, an analogous time-dependent expression $P(t_z)$ may also be used to fit the TOA profiles (as in Fig. 3). These nonlinear fits provide values of T_c and u. Similar results are obtained from plotting the observed mass-dependence of the peak TOA values for various species (see Fig. 4). As shown in Figs. 3

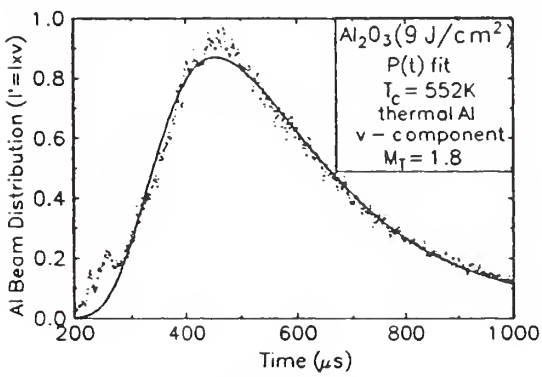

Figure 3 — Time-of-arrival for Al (Al_2O_3); λ = 1064 nm, fluence = 9 J cm^{-2}

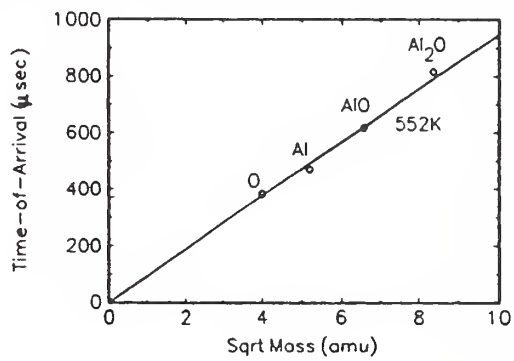

Figure 4 — Peak TOA dependence on $(mass)^{1/2}$ for species from Al_2O_3; λ = 1064 nm.

and 4, the value of T_c = 552 K is evidence of considerable expansion cooling. From the magnitude of the mass spectral intensities, we have determined that the initial pre-expansion pressure is typically of the order of one bar (4). For Al_2O_3, a surface temperature of 4500 K would be needed to generate a pressure of this magnitude.

Conversion of the TOA profiles to a velocity scale shows that the data of Fig. 3 correspond to relatively low velocities ($\sim 10^4$ cm s^{-1} range), characteristic of moderate terminal Mach numbers ($M_T \sim 1.8$). As the laser fluence is increased, an additional discrete faster velocity distribution(s) is found (see Fig. 5). This faster velocity distribution becomes relatively more significant with increasing fluence and has a very high T_c ($\sim$31,000 K). These effects can be attributed to laser-plasma interactions (2,6). The plasma gasdynamic model fit, shown in Fig. 5. and discussed in detail elsewhere (2,6), agrees well with the observed high-energy distribution,

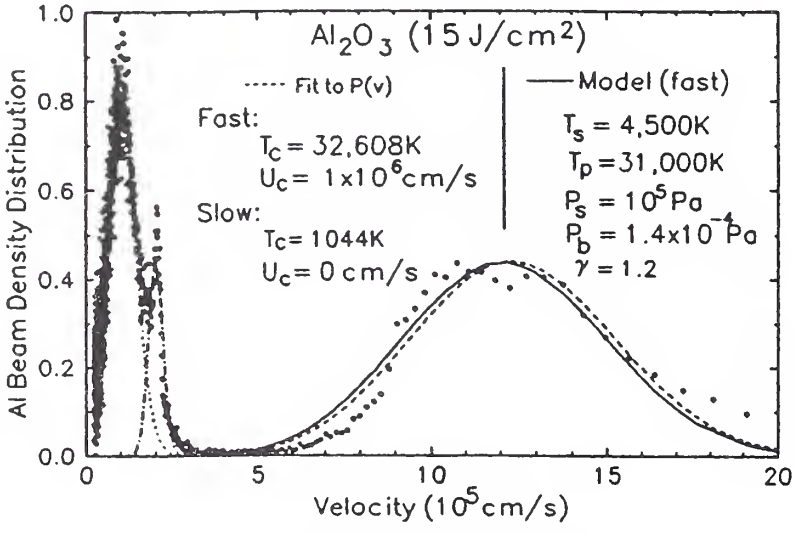

Figure 5 — Velocity distribution for Al (Al_2O_3) at 15 J cm^{-2}; λ=1064 nm

Sampling Fidelity A key question concerning any free-jet MBMS measurement approach is the reliability of the sampling process. In contrast with our earlier sampling of atmospheric pressure flames (7) and transpiration vapors (8,9), a sampling probe was not inserted into the active high pressure core of the plume. Instead, the sampling orifice was located (usually) well downstream of the shock front (Mach disc) location and in a region of collisionless flow. The target-to-orifice distance was 22 cm, compared with the calculated (from measured Mach numbers) distance to collisionless flow in the range of 0.05 — 5 cm. Also, the pumping speed and conductance was high enough that the calculated Mach disc location was always downstream of the transition to collisionless flow. Agreement between experimental and calculated expansion temperatures indicates that the sampling process was indeed located at a fully expanded jet location, and no gasdynamic or other thermal perturbation was occurring.

There is strong evidence that local thermal equilibration of neutral species occurs in these laser plumes. It can be shown (*e.g.* from Eq. [1]) that the peak time-of-arrival times should vary inversely with species mass provided the local thermal equilibration condition is maintained. In general we have found such a dependence (Fig. 4). Data analysis using this type of relationship also provides an additional benefit in assuring the reliability of the mass spectral species assignments. If electron impact fragmentation interference occurs, it would be evident as a displacement from the line in Fig. 4, since the peak times refer to the preionized condition of each species. As we have indicated elsewhere, free-jet MBMS can lead to very different fragmentation patterns than those found conventionally (4,10). With a few notable exceptions (10), the expansion cooling process can be very beneficial in reducing electron impact fragmentation (4).

A more stringent, and more difficult to establish, test of sampling fidelity is provided by examination of possible shifts in chemical equilibria or kinetics. That is, are the relative concentrations of the sampled species modified by the sampling and analysis process? We have shown elsewhere that, for systems that are demonstrably in thermodynamic equilibrium, sampling perturbations are negligible (8,9). In laser-generated plumes, however, there is no *a priori* assurance that the pre-expansion plume is chemically equilibrated. We have shown elsewhere that

for moderate laser fluences, sufficient to attain a near-atmospheric boiling condition at the target surface, the pre-expansion species are frequently present in local thermodynamic equilibrium (4,6). The MBMS species distributions are also found to agree well with thermodynamic equilibrium calculations, *e.g.* for C (4), BN (11), HfO_2 (5), $BaTiO_3$ (2,6) and Al_2O_3 (6). For the Al_2O_3 case, we have also carried out detailed gaskinetic calculations, showing that relatively small changes in species concentrations are possible and particularly during the first 20 ns of plume expansion (6).

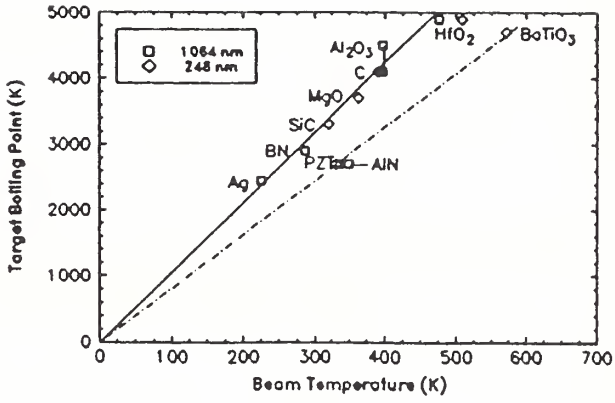

Figure 6 — Beam-surface temperature correlation

Conversion of Final (Expansion) to Initial State Properties The MBMS measurements yield information on terminal velocities (v_T) and temperatures ($T_T \equiv T_b \equiv T_c$). If we assume that the formation of an expanding vapor plume from a focused hot spot is gasdynamically similar to expansion through an orifice, then various standard gasdynamic relationships apply. The initial pre-expansion temperature of the gas, T_o, may then be obtained from:

$$T_T/T_o = [1 + \frac{\gamma-1}{2} M_T^2]^{-1} \qquad [2]$$

Typical values fall in the range 2500 — 8000 K (for gas heat capacity ratio γ = 1.4 — 1.2 range). Pressure ratios may be obtained from:

$$T_T/T_o = [P_T/P_o]^{\frac{\gamma-1}{\gamma}} \qquad [3]$$

Typical values of P_T/P_o in our system fall in the range 10^{-4} — 10^{-5}, or lower. When combined with P_T values determined from calibration of the mass spectral intensities, values of P_o in the range of 1 — 10 bar are obtained. Direct and indirect measurement of surface temperatures also indicate target temperature and pressure conditions near the boiling point at moderate fluence conditions ($\leq$ 1 — 10 J cm^{-2}). Based on eq. [3], we should then expect to find a linear correlation between the thermodynamically derived target boiling temperature ($T_{bpt} \sim T_o$) and the final, or beam, temperature (T_b) if T_o is strongly correlated with the surface temperature. The solid curve in Fig. 6 shows such a correlation for a variety of materials. The second dashed curve was obtained with significantly high laser fluence, where laser-plume interactions raised the effective values of T_o to values much greater than T_{bpt} (*i.e.* > 10,000 K).

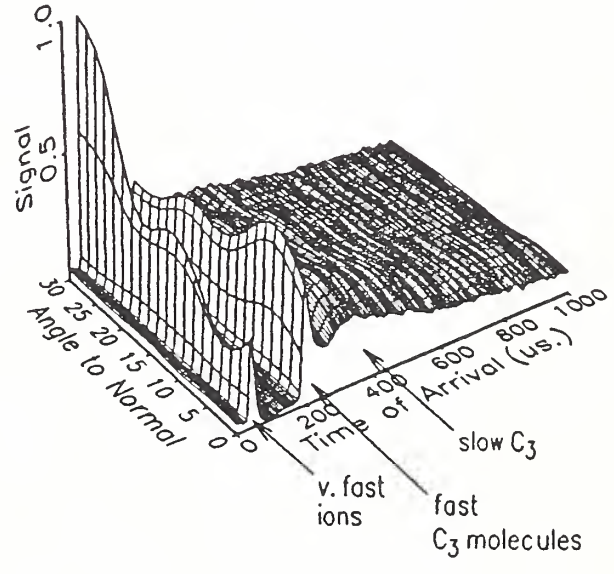

Figure 7 — Angular distribution TOA behavior for C_3 from graphite.

Plume Angular Distribution Effects The target kinematic stage can be tilted, *in situ*, relative to the fixed MBMS sampling axis. Measurement of species intensity changes, as a function of angle from the normal, have allowed us to observe high order cos θ^n distributions with $n \sim 5 - 20$. These values of n are consistent with other arguments made here concerning the supersonic nature of expanding laser plumes. Other intriguing observations, such as are shown in Fig. 7, have also been made (work in progress). The unusual angle dependencies shown for the fast neutral and charged species are attributed to laser-plume interactions, which are more significant for ions and can lead to non-symmetrical geometry effects in the plume.

CONCLUSIONS

In summary, the application of free-jet MBMS to laser plumes is of considerable value. Identities and concentrations of all significant species can be obtained. Velocity distributions and temperatures, combined with gasdynamic and plasma models, yield information on the pre-expansion plume properties. These results also complement those obtained by optical probes [not discussed here, see (2)].

The species identity, flux and kinetic energy information obtainable is directly applicable to growth models of thin film formation. Information on spatial and temporal plume evolution can indicate optimal target, laser, and substrate positioning. Determination of species relationships with process variables (fluence, wavelength, pulse time, pressure, ...) also allows for selection of optimum process conditions. Finally, MBMS results complement and enhance the development of more non-intrusive optical probes for *in situ*, real-time process monitoring and control.

REFERENCES

1. Chrisey, D. B. and Hubler, G. H.,(eds.) *Pulsed Laser Deposition of Thin Films* (John Wiley and Sons, Inc., 1994).
2. Hastie, J. W., Bonnell, D. W., Paul, A. J., and Schenck, P. K., "Gasdynamics and Chemistry in the Pulsed Laser Deposition of Oxide Dielectric Thin Films," *MRS Proc.* 334, (MRS, Pittsburgh, PA, 1994), p. 305.
3. Hastie, J. W., Bonnell, D. W., and Schenck, P. K., "Molecular Basis for Laser-Induced Vaporization of Refractory Materials," *NBSIR 84-2983* (National Technical Information Service, Washington, DC., 1984).
4. Hastie, J. W., Bonnell, D. W., and Schenck, P. K., *High Temp. High Press.*, 20, 73, (1988).
5. Bonnell, D. W., Schenck, P. K., Hastie, J. W., and Joseph, M."Ultra-High Temperature Laser Vaporization Mass Spectrometry of SiC and HfO_2," *5th Intl. Symposium on High Temperature Materials Chemistry*, PV90-18, (Electrochemical Society, Pennington, NJ, 1990).
6. Hastie, J. W., Paul, A. J., Yeheskel, J. Bonnell, D. W., and Schenck, P. K., *High Temp. Sci.*, in press (1994).
7. Hastie, J. W., *Combust. and Flame*, 21, 187 (1973).
8. Hastie, J. W., Bonnell, D. W., "Transpiration Mass Spectrometry: A New Thermochemical Tool," in *Thermochemistry and Its Applications to Chemical and Biochemical Systems*, (ed.), M. A. V. Ribeiro da Silva, (Reidel Publishing, Boston, MA, (1984), p. 183.
9. Hastie, J. W. and Hager, J. P., "Vapor Transport in Materials and Process Chemistry," *Proc. The Elliott Symposium on Chemical Process Metallurgy*, (Iron and Steel Soc., 1990), p. 301.
10. Bonnell, D. W., Hastie, J. W., and Zmbov, K. F., *High Temp. High Press.* 20, 251 (1988).
11. Hastie, J.W., Bonnell, D. W., and Schenck, P. K., *High Temp. Sci.*, 25, 117 (1988).

• Presented at *Specialists Workshop on Applications of Free-Jet Molecular Beam Sampling*, Estes Park, CO. (US DOE National Renewable Energy Laboratory, October 12-14, 1994,)

APPENDIX D

Film Synthesis and Growth using Energetic Beams, D.H. Lowndes, et al (eds) (MRS, PA, 1995)

In Situ Monitoring and Model Simulation of $BaTiO_3$ Pulsed Laser Thin Film Deposition

ALBERT J. PAUL, PETER K. SCHENCK, DAVID W. BONNELL, JOHN W. HASTIE
National Institute of Standards and Technology, Gaithersburg, Md 20899

ABSTRACT

We have applied Intensified Charge Coupled Detector (ICCD) imaging to real-time, *in situ* monitoring of excited vapor species emission during the pulsed excimer (248 nm wavelength) laser deposition (PLD) of $BaTiO_3$ ferroelectric thin films. Molecular beam mass spectrometry (MS) was used for species identification and velocity distribution analysis. Gasdynamic model simulations of the plume formation and transport process are tested by comparison with the ICCD and MS results. Particular attention is given to the time scale during and immediately following the laser pulse (0 – 460 ns), and also to the effects of added O_2. Atomic oxygen was found to be the predominant species present at the leading edge of the vapor plume. Other, slower species found included neutral Ti, TiO, Ba, and BaO.

INTRODUCTION

The PLD technique is emerging as an alternative approach to more conventional methods for the production of stoichiometrically complex thin films such as $BaTiO_3$[1]. High energy pulsed laser light is focused onto a target, generating a vapor plume that is transported gasdynamically and is condensed onto a substrate. The vapor pressures developed at the target surface typically lie in the range, 10^5 – 10^7 Pa (~1 – 100 bar). Current understanding of the detailed dynamics of the evaporation/ablation process is limited, and new or improved diagnostics and models are needed to clarify the gas-collision and laser-gas interaction events occurring in the near-target region of the expanding plume[1,2]. Experimental tests of most reported gasdynamic models under pre- or interim-expansion (near-field) conditions have been limited by the lack of direct observations within the short time frame of the early expansion (0 – 100 ns)[1]. In this work we applied ICCD imaging to the temporal and spatial analysis of the early stages of the laser plume expansion in the near-field. The results are used to test a three-dimensional gasdynamic simulation of plume expansion. Post-expansion (far-field) MS–determined velocity distributions and temperatures were used to assign gasdynamic model parameters, from which the near-field nature of the plume was simulated.

MODEL SIMULATION

Our model simulation approach has been discussed earlier[1,2] and is based primarily on the work of Dawson, *et al*[3], Singh and Narayan[4], and Predtechensky and Mayorov[5]. In the present three-dimensional simulations, we continue to utilize the isothermal expansion approximation to model the plume region during the laser pulse[4]. Following the ending time ($t=\tau$) of the laser pulse, the plume is considered to expand adiabatically (*see Eq.* 1). To model this expansion process with a background gas present, we adopted Predtechensky's approach[5], converting his radial formulation to Cartesian coordinates assuming equivalent equations of motion in each direction (*see Eq.* 2). The adapted model correctly reduces to the Dawson model[3] when the background gas density $\rho_0 \approx 0$. Each individual species was considered independently of other species of differing mass. Thus, an effective combined pressure at the species-specific plume "front", $P_i(t)$ for a species i at any time $t > \tau$, was treated using:

$$P_i(t) \approx P_o + P_{s,i}\left(\frac{X_o Y_o Z_o}{X_i(t) Y_i(t) Z_i(t)}\right)^{\gamma} \quad ; \qquad (1)$$

$P_{s,i}$ is the maximum partial pressure of species i at the target surface, P_o is the static background pressure; the coordinates $X_i(t)$, $Y_i(t)$, and $Z_i(t)$ are the Cartesian extents of the plume "front," an ellipsoidal "boundary" where the species vapor density has fallen to 60.65 percent of its maximum at t; X_o, Y_o, and Z_o are the plume extent coordinates at the end of the isothermal expansion stage[4]; γ is the gasdynamic factor (the effective plume heat capacity ratio). The equation of motion for the plume front location of species i in the z-direction (perpendicular to the target surface) is:

$$\frac{d^2 Z_i}{dt^2} = \frac{X_i(t) Y_i(t) P_i(t) - X_i(t) Y_i(t) \rho_o \left(\frac{dZ_i}{dt}\right)^2}{(M_i + [X_i(t) Y_i(t) Z_i(t)] \rho_o)} \quad ; \qquad (2)$$

M_i is the total vaporized mass (in gm) of species i; ρ_o is the mass density of the background gas, determined from P_o and the calculated volume at the end of the laser pulse. The time evolution of the plume extent was simulated using a step-wise Runge-Kutta method to obtain time-dependent solutions of the model equations of motion. The model for the centerline (z-axis) number density (n) of the plume during adiabatic expansion ($t > \tau$) at distance z is given by[4]:

$$n(z,t) = \frac{N_T}{2^{0.5}\pi^{1.5} X(t) Y(t) Z(t)} \times e^{\left(\frac{-z^2}{2\,Z(t)^2}\right)} \quad , \qquad (3)$$

where N_T is the total population of all species produced during the isothermal stage.

The required model input parameters included: the initial plume coordinates that we obtained from direct measurements of the laser footprint at the target; the pressure and temperature of the vapor at the target, taken from estimates based on MS data and deposition rates[6]; the measured pressure of any added background gas (usually, $P_o \ll P_s$); the pre-expansion plasma temperature (treated as an adjustable parameter); γ taken as 1.3, based on MS observations of the expanded plume[6]; and the time interval for the isothermal expansion phase of the simulation (assumed to be the duration of the laser pulse, $\tau \sim 30$ ns, in this study).

EXPERIMENTAL

Apparatus for *In Situ* Monitoring

The apparatus details have been given elsewhere (ICCD[1,2]; MS[1,7]). The essential features are as follows. The ICCD camera provides time-resolved (to 5 ns, both in frame duration {gate width}, and time of frame relative to the beginning of the laser pulse) two-dimensional images. These images may be linked together to form sequential "movie"-like representations of the PLD plume emission history. The MS has a direct path to the target through differentially pumped apertures. This geometry allows one to define a molecular beam with a composition that is representative of the expanded plume. The total path length from the target to the MS ion source is $\ell = 47.4 \pm 0.1$ cm. Time-resolved molecular beam analysis of mass-selected species provides post-expansion intensity I ($\propto$ beam number density) *vs.* time-of-arrival (TOA) profiles of all major

vapor species. These profiles can also be transformed into flux distributions ($I' = I \times \ell/t$) for velocity analysis, as shown in Figs. 1 and 2.

RESULTS AND DISCUSSION

TOA profiles and ICCD images were obtained for $BaTiO_3$ using excimer laser irradiation at 248 nm wavelength and ~13 J cm^{-2} fluence. The MS intensity (I) data were converted to flux (I') by scaling each intensity point by the factor ℓ/t to correct for the v discrimination of the number-density-sensitive MS ion source.

Velocity and Temperature Analysis

We have determined[1] that the MS-derived velocity (v, measured here in the Z-direction) distributions for individual species are best represented as a full-range Maxwellian velocity distribution (beam *flux*) that includes a net (center-of-mass) flow velocity, u:

$$f(v) \propto v^3 \exp\left[\frac{-m}{2kT_b}(v-u)^2\right] , \qquad (4)$$

where $-\infty < v < \infty$, T_b is the beam temperature, k ($= 1.38\times10^{-16}$ erg K^{-1}) Boltzmann's constant, and m, the species atomic/molecular mass. The values of T_b and u were obtained from non-linear fits of this expression to our experimentally-derived TOA distributions, as shown in Fig. 2. Likewise, the mass dependence of t_{max}, the time of peak *flux* in Eq. 4, can be used to obtain T_b, as well as to provide a stringent test for thermal equilibration among the different molecular weight (M) species present, as shown in Fig. 3. We derive the following relationship between T_b and the *slope* of the fitted line (in μs/M$^{1/2}$, *e.g.*, as in Fig. 3):

$$T_b = 4.01\times10^3 \left\{\frac{\text{mol}\cdot\text{K}}{\text{erg}}\right\} \frac{\ell^2}{(slope)^2}\left[\frac{t_{max}}{t_{mp}}\right]^2\left(1 - \frac{u\,t_{max}}{\ell\times10^6}\left[\frac{t_{mp}}{t_{max}}\right]\right) , \qquad (5)$$

where T_b is in K, ℓ is in cm, u is in cm s^{-1}, and t_{max} is in μs. The transformation term, t_{mp}/t_{max} (*i.e.*, the ratio of the time corresponding to the most probable velocity to the TOA of peak flux), is a function of the flow velocity and temperature:

$$\frac{t_{mp}}{t_{max}} = \left(1 \pm \left[1 + \left(\frac{20kT_b}{mu^2}\right)\right]^{1/2}\right) \Bigg/ \left(1 \pm \left[1 + \left(\frac{12kT_b}{mu^2}\right)\right]^{1/2}\right) . \qquad (6)$$

T_b is obtained by iteration of Eqs. 5 and 6.

Model Simulations

A representative model simulation fit to the O-atom data of Fig. 1 is indicated in Fig. 4. Here, the model pre-expansion plume temperature (T_p) was adjusted until the model post-expansion temperature (T_b) agreed with the MS-determined value and the resultant distribution was then calculated. The experimental t_{max} values for all the neutral species could be satisfactorily simulated by the model, *e.g.*, as shown for O in Fig. 4. However, no reasonable set of input parameters allowed the model to simulate the observed *shape* of the distribution. We believe that one source of this discrepancy is due to not including the flow velocity term (u) in the simulation,

with the consequence that the model assumes the vapor density maximum to remain at the origin (laser impact point) whereas both the MS data and the ICCD images indicate motion of the maximum. Explicit incorporation of the flow term into the model is under investigation. Also, the model assumes continuum flow at all distances, while the MS is located considerably downstream of the transition to molecular flow — explicit inclusion of the transition to molecular flow is also currently being considered.

Mass and optical emission spectral observations have indicated the outer plume extent to be predominantly composed of atomic oxygen. Model simulation of the 60.65 percent atomic oxygen density contours in the plume yielded an expansion time/distance history similar to the image data when high model plasma temperatures and target vapor densities were assumed, as indicated in Fig. 5. The presence of strong continuum plasma emission close to the surface, which persisted through the 180 ns frame and exceeded the collisional emission maximum, distorted the "normal" plume contours at 100–180 ns. As the collisional emission is more representative of the species transport the model describes, the frames at 100, 140, and 180 ns have been corrected to eliminate the effect of the continuum emission maximum. Other effects may also be present, but are not considered in present expansion models. These effects include ion-electron recombination and surface charging[8], and the phase explosion mechanism discussed elsewhere for AlN PLD[9].

In summary, these results clearly indicate the distinctly differing energetics of those components of the plume responsible for observed emission (where $T_p \sim 750{,}000$ K, as in Fig. 5), in contrast to the lower energetics of the primarily non-emitting ground state species components (where $T_p \sim 6700$ K, as in Fig. 4) observed *via* MS in the far-field molecular beam. This aspect, of various plume components with widely differing energetics, will be discussed in future work. Also needing further consideration is the question of the most appropriate transition period, τ, between the isothermal and supersonic adiabatic expansion regions of the expansion model. The current assumption, that the laser pulse termination time determines τ, is a rather arbitrary convenience, as plume densities and velocities generally appear to attain a supersonic expansion state well before the end of the laser pulse under typical film deposition conditions.

REFERENCES

1. J.W. Hastie, D.W. Bonnell, A.J. Paul, & P.K. Schenck, "Gasdynamics and Chemistry in the Pulsed Laser Deposition of Oxide Dielectric Thin Films," in *Gas-Phase and Surface Chemistry in Electronic Materials Processing*, T. Mountziaris, G. Paz-Pujalt, F. T.J. Smith & P. Westmorland (Eds), MRS Proceedings **334** (MRS Pittsburgh, PA 1994), p. 305-316.
2. P.K. Schenck, J.W. Hastie, A.J. Paul, & D.W. Bonnell, "Imaging and Modeling of Pulsed Laser Thin Film Deposition Plumes," in *Laser-Induced Thin Film Processing*, J.J. Dubowski (Ed), SPIE Proceedings **2403**, 26-38 (1995).
3. J. Dawson, P. Kaw, & B. Green, *Phys. Fluids*, **12(4)**, 875-882 (1969).
4. R.K. Singh & J. Narayan, *Phys. Rev. B*, **41(13)**, 8843-8859 (1990).
5. M.R. Predtechensky & A.P. Mayorov, *Appl. Supercond.*, **1(10-12)**, 2011-2017 (1993).
6. J.W. Hastie, D.W. Bonnell, A.J. Paul, J. Yeheskel, & P.K. Schenck, *High Temp & Matr. Sci.* (formerly *High Temp. Sci.*), **33**, 135-169 (1995).
7. J.W. Hastie, A.J. Paul, and D.W. Bonnell, "Free-Jet Mass Spectrometry of Laser Ablation Plumes in Thin Film Deposition," in *Specialists Workshop on Applications of Free-Jet Molecular Beam Sampling*, *NREL Report CP433-7748*, T. Milne (ed), (NTIS, Washington, DC, 1995).
8. R.M. Gilgenbach, C.H Ching, J.S. Lash, & R.A. Lindley, *Phys. Plasmas*, **1**, 1619-1625 (1994).
9. R. Kelly, A. Mele, A. Miotello, A. Giardini, J.W. Hastie, P.K. Schenck, & H. Okabe, *Nucl. Instr. Meth.*, in press (1995).

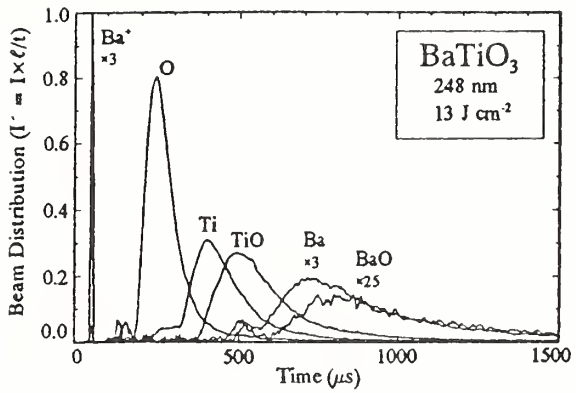

Figure 1. TOA species flux (distribution) curves (arb. units) for MS-sampled PLD beam. $P_o \lesssim 10^{-5}$ Pa (chamber background). Measurement uncertainties are: $I' \pm 0.01$; $t \pm 5$ μs.

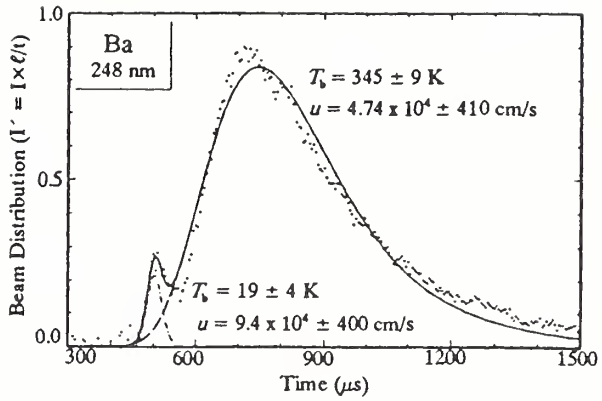

Figure 2. Comparison of TOA distribution (points) for Ba (from Fig. 1) with fitted (sum of two; includes u term — *see text*) full-range Maxwell distributions.

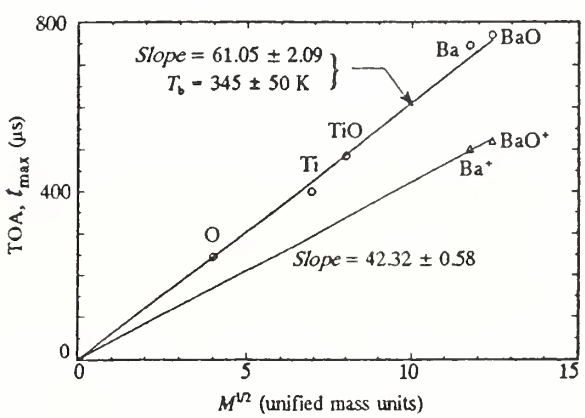

Figure 3. Plot of t_{max} *vs* $M^{1/2}$ for species sampled from $BaTiO_3$ plumes (from Fig. 1). The symbols denote fast (triangle) and slow (circle) peaks in the TOA curves of Fig. 1. Uncertainties: $t_{max} \lesssim \pm 20$ μs; MS-observed $M \pm 0.1$ umu.

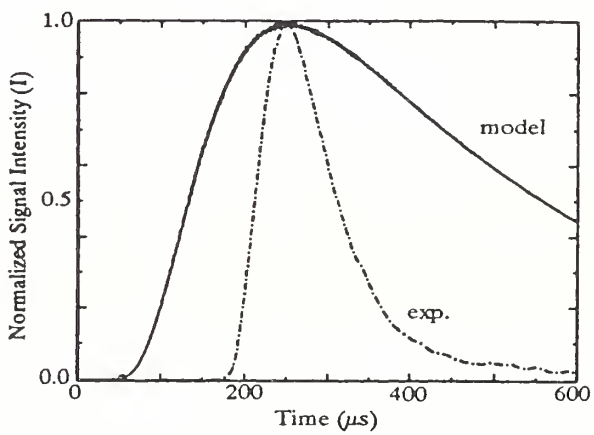

Figure 4. Comparison of far-field model simulation of O-atom density *vs.* time with MS data (I) for Fig. 1 conditions. Model density derived using Gaussian density expression (*see* Eq. 3), with $z = \ell = 47.4$ cm. Model parameters: laser footprint $0.1 \times 0.063 \pm 0.005$ cm; $T_s = T_p = 6700$ K, $P_s = 5$ MPa (50 bar), $P_o = 5$ Pa (5×10^{-5} bar), $\gamma = 1.3$.

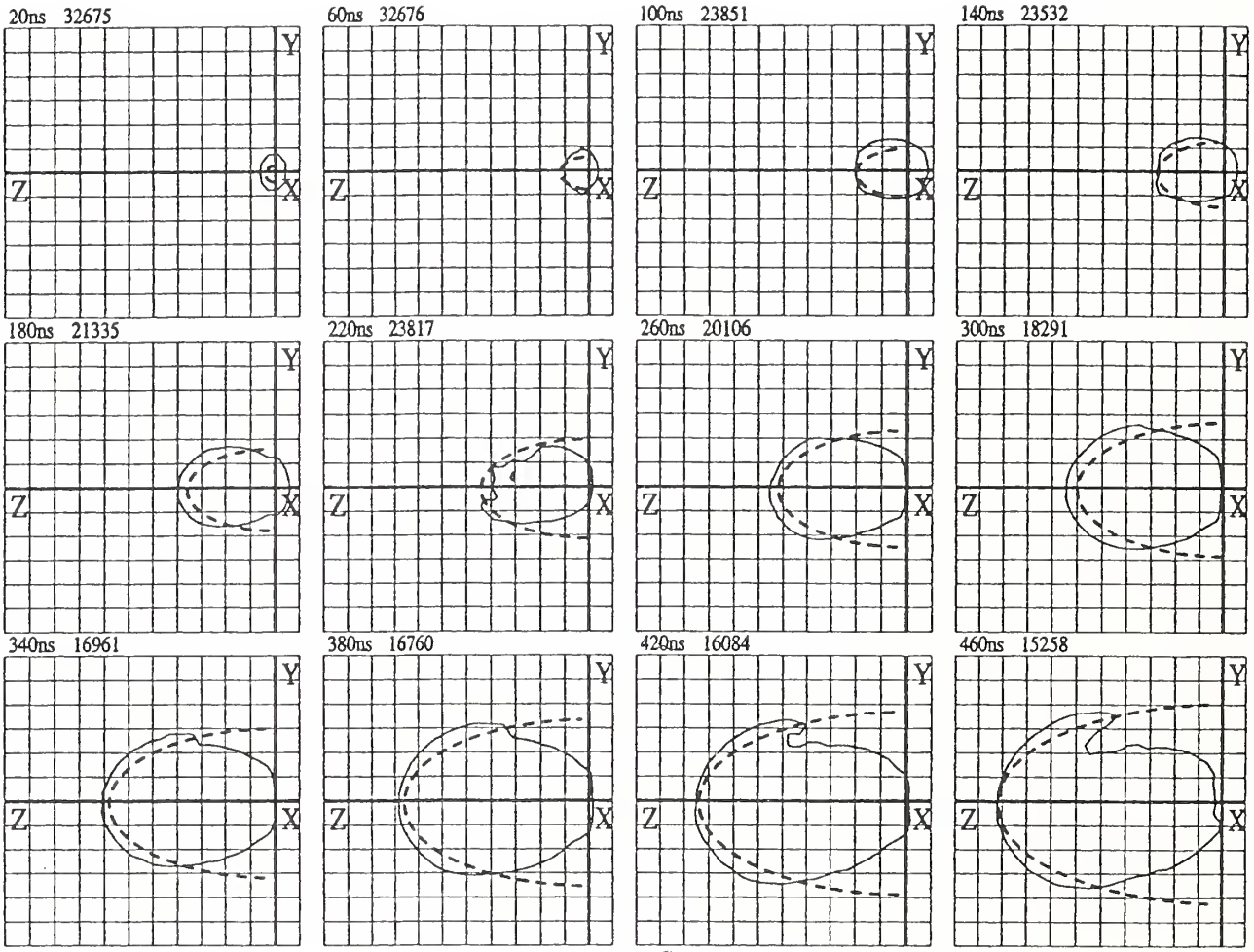

Figure 5. Contour plots (solid curves) from sequential ICCD images of visible emission (500–800 nm) from laser-irradiated $BaTiO_3$ at 248 nm, ~13 J·cm^{-2} fluence, with P_o ~ 13 Pa (O_2). Grid scale is 1 mm. Individual image intensities have been scaled to the frame maximum (*see text*); relative intensity maxima (in digitizer counts) for each frame are indicated beside the frame time shown at the upper left of each frame. Frame times are ±1 ns and are referenced to the beginning of the laser pulse, whose duration was nominally 30 ns. Contours outline 60.65 percent of emission intensity maximum in each frame. The camera "shutter" (frame duration) gate width was nominally 10 ns; images were collected at 20 ns (nominal) intervals as the sum of eight generated plumes, but only the 40 ns interval frames are shown here. Dashed curves are two-dimensional projections in the ICCD camera plane of model simulations of the ICCD image contours. As the long dimension of the laser footprint was oriented at 45° to the image plane, a linear transformation of the model $X(t)$, $Y(t)$ coordinates was made to coincide with the experimental X, Y observation coordinates noted on each frame. Uncertainties in experimental contour location estimated as ±0.2 mm in observed X and Y.

Model conditions used were: laser footprint 0.16×0.04 cm; plasma temperature T_p = 75 eV (~750,000 K); T_s = 6700 K; $P_s = 5\times10^6$ Pa (50 bar); P_o = 13 Pa; γ = 1.3.

APPENDIX E

NISTIR 6768

A Predictive Ionization Cross Section Model for Inorganic Molecules

J.W. Hastie,
Ceramics Division

MSEL

July 2001

U.S. Department of Commerce
Donald L. Evans, Secretary

National Institute of Standards and Technology
Karen H. Brown, Acting Director

A Predictive Ionization Cross Section Model for Inorganic Molecules

J. W. Hastie
National Institute of Standards and Technology
Gaithersburg, MD 20899, U.S.A.

Abstract

To address a long-standing lack of experimental data for electron impact ionization cross sections for inorganic molecules, or the availability of a reliable predictive method, we have developed a modified classical model. The model relies on the known or expected ionic bonding character of most inorganic and, particularly, of high temperature molecules. Based on isoelectronic analogy, use is made of available cross section data for the elements, together with known or readily calculated ionization potentials for the molecules of interest. Very good agreement is found for several of the species considered here and elsewhere using the more extensive and primarily ab initio binary-encounter Bethe model. Good overall agreement is also found with experimental results for fifty-one species, with up to ten constituent atoms. The model appears to be at least as accurate as experimental methods, is free of adjustable parameters, and is generally applicable to inorganic and high temperature molecules. An expected relationship with polarizability is found in addition to support for a concept involving additivity of ionic cross sections. Model result implications for the accuracy of thermochemical data in existing databases are considered.

Keywords: ionization, cross section, high temperature, models, thermochemical data, autoionization.

1. Introduction

Electron impact ionization cross sections (σ) are important in diverse areas of science and technology. They are, and have been for nearly half a decade, particularly pertinent in the application of high temperature mass spectrometry to thermodynamic studies, as has recently been discussed in detail elsewhere [1]. In many instances, measurement of σ's for high temperature molecules is either impractical or inaccurate. For studies reliant upon estimates of molecular ionization cross sections, the estimates are based on additivity (or some empirical reduction thereof) of the component atomic cross sections. The additivity approximation has its basis in studies on organic or covalently bonded species. On the other hand, the majority of high temperature species are characterized by ionic bonding, where electron transfer to the more electronegative atom leads to anion-cation association with characteristic strong coulombic interaction. Ionic models have proven very satisfactory for prediction of bond dissociation energies [2] and of ionization potentials [3]. Here, we examine the application of an ionic model to the prediction of ionization cross sections. The cross sections considered here, and those of greatest utility, are for electron impact production of singly charged positive ions, including parent and all fragment ions. As multiply charged ions are usually negligible at the energies of interest (~10 – 50 eV), these σ's are effectively total ionization cross

sections. From theoretical and practicality-of-application considerations, emphasis is given here to σ_m, the maximum ionization cross section at energy E_m. These σ_m values can then be scaled, although with reduced accuracy, to other values of E.

Classical, molecular-orbital-based models have recently been applied, with some success, to a few relatively low molecular weight inorganic species such as SiF and SiF_2 [4]. However, the extension of such molecular-orbital-based models to high molecular weight, many electron high temperature species is problematic.

The difference in electron configurations, underlying cross section behavior, between an atom and its cation or anion can be considerable. It appears likely, therefore, that use of atomic cross-section-based models may be unreliable and hence lead to larger than expected errors in derived thermochemical or similar species-concentration-related properties. The importance of σ's and their uncertainty estimates have been noted in standard thermodynamic databases [5, 6]. In the present study, we show that these earlier error assignments to σ's can, in some instances, be greatly underestimated.

2. Approach

2.1 Model basis

Various classical models (discussed below) have been developed earlier, relating σ_i for orbital i with E, B_i, N_i, where E is the electron impact energy, B_i the orbital energy, and N_i the orbital electron occupation number (see literature summary in [1]). In one of these models, explicit consideration of orbital radii is also made [7]. These models have been applied with reasonable success primarily to the elements and secondarily to gaseous, covalently bonded molecules. While such models have a theoretical basis, empirical scaling has generally been required to obtain agreement with experiment, particularly for molecules. Also, complex molecular orbital calculations have been required to obtain model input values of B_i and N_i, in addition to other parameters.

We consider here the development of a predictive σ model, requiring minimal a priori knowledge (ie. ionization potential) of the molecule of interest and with a single gobal scaling factor, obtained from an averaged small set of experimental values. For high temperature species, the model must account for their characteristic ionic (vs covalent) bonding. Cross sections for high temperature species are usually associated with mass spectrometry experiments [1], where the ionization potential, B, is readily measured or can be calculated from an ionic model [3]. However, higher-level orbital energies are generally not known. From appearance potential studies, E_m, the energy at which σ is at a maximum, is often found to be much lower than for covalent species, particularly for open-shell electron configurations. For such cases, B, the energy of the lowest occupied molecular orbital, will have a dominant effect on the cross section.

Thus in its simplest and most practical form we consider the function (fn.) where:

$$\sigma_m \sim \text{fn. } (B, N, E_m) .$$

Hereafter, σ_m is taken to be at its maximum value and is designated as σ. Thus, for the present purposes, the energy scale is fixed at E_m. From consideration of the more detailed classical models discussed below, the form of the above σ relationship is suggested as:

$$\sigma \sim f N'/B, \qquad (1)$$

where f is a constant between like species (eg. atoms) and N′ is an empirical term we designate as an effective number of ionizable electrons. As will be shown (section 2.1.5), an explicit consideration of the functional dependence of N′ on E_m and B_i is unnecessary. Moreover, N′ is not necessarily an integer and is related very indirectly to the N term of classical models discussed below (sections 2.1.1, 2.1.2, 2.1.3). We stress here that the purpose of considering eq. (1) in this form is to relate σ's, at E_m , among various species categories, ie. atoms or molecules. Consideration of σ at other values of E is made separately (see section 3.6) where the energy dependence of N′ is explicitly considered. For discussion purposes, we designate the model described by eq. (1) as a modified classical method (MCM).

2.1.1. Binary-encounter Bethe (BEB) model simplification.

The BEB model [4] can be represented in the form:

$$\sigma_i \sim (N_i / B_i) (E + U_i + B_i)^{-1} (C),$$

for each contributing orbital i, and where
$C = 0.5 \ln x (1 - x^{-2}) + 1 - x^{-1} - \ln x (x + 1)^{-1}$,
$x = E / B_i$, and U_i is orbital kinetic energy.
Then $\sigma = \Sigma \sigma_i$. Values of B_i and U_i are obtained from Hartree-Fock molecular orbital calculations. For the lowest energy orbital, the experimental vertical ionization potential B is used. The terms within the collision factor C become more significant at higher E and particularly at $E > E_m$.

For high temperature and inorganic molecules, where we designate $E = E_m$ as the principal energy of interest, values of x are generally in the range, $x = 3 - 7$. Values of $E + B$ typically fall in the range 20 – 70 eV. For the relatively low E's of the present application, we neglect U. It appears that the semiempirical form of the present model adequately accounts for this U term in an indirect manner. If the U term was significant and was not effectively compensated for, the model σ`s would be expected to exceed the experimental values, but no such systematic trend is found. For these conditions, it can be shown that the product of the E-containing bracketed terms of the σ_i equation is, to a good approximation, constant for the above range of x, ie. well within the model and experimental σ uncertainties. Also, the empirical nature of N′ (discussed in section 2.1.5) is expected to account for differences between molecules in the E-containing terms. Thus, at E_m , the BEB model simplifies to the form of the present model, as given in equation (1). For relatively large values of x, such as would occur with closed shell multiatomic species, eg. SiF_4, WF_6, and W_2O_6, one might expect the approximations

made here to be less reliable. However, for such cases, the MCM model gives σ's in good agreement with experiment.

2.1.2 Mann (modified Bethe) model simplification.

The model approach of Mann [7], which applies exceptionally well to those elements where direct ionization is the main pathway, has the form:

$$\sigma_i = N_i \langle r \rangle^2 [E^{-1} \ln (E / B_i)]$$

where $\langle r \rangle^2$ are orbital (i) mean square radii. In practice, Hartree-Fock molecular orbital calculations are used to obtain $\langle r \rangle^2$ and B_i (higher level) data. The absolute $\sigma = \Sigma\sigma_i$ values are scaled using a single experimental value (ie. $\sigma_{Ar} = 2.83 \times 10^{-20} m^2$).

Empirically, we find for the non-gaseous elements that $\langle r \rangle^2 \sim B^{-1}$ and hence the Mann model and the present MCM model reduce to a similar form, for our conditions, where the bracketed term is constant to a good approximation. Similar arguments apply to a more recent version of this model (see [7]).

2.1.3 Gryzinski-binary encounter model simplification.

The Gryzinski model [8] has a similar form to that of the more recent BEB model, although in the latter case the E^{-1} term was replaced by $(E + U + B)^{-1}$. For our conditions (see section 2.1.1), collision terms involving x and the term E^{-1} simplify to an approximate constant, as was the case for the BEB model expression. The Gryzinski model, at E_m , then reduces to the form of eq. (1). Thus earlier classical and more current comprehensive models each may be simplified to the form of the present model. It should be noted, however, that our application of the complete form of the Gryzinski model to molecules of the type considered here did not lead to satisfactory results. A similar situation occurs for atoms, as indicated in [1].

2.1.4 Model dependences on E and B.

We note that for some molecular species, denoted MX, where $B_{MX} \sim d_{MX}^{-1}$ (the internuclear distance), the simplified Mann formula would indicate a higher order dependence of σ_{MX} on B_{MX}. Similarly, there exists a suggested relationship between σ and B^{-2} known as Thompson's Rule [9]. While the conditions leading to such a dependence are not typical of those for the species and conditions of interest here, we nevertheless carried out model tests for the relationship:

$$\sigma \sim N'/B^2 ,$$

and found much poorer accord with experiment. Also, very poor accord was found with Thompson's Rule, even for isoelectronic pair comparisons. Similarly, no empirical basis was found for possible model explicit inclusion of E^{-1} or E^{-2} terms which could be significant at high E_m values.

At this time we conclude that further refinements to the model are unwarranted, considering the model approximations and the present degree of uncertainty associated with atomic and, more particularly, molecular ionization cross sections.

2.1.5 Evaluation of N′ for MCM ionic model application.

In principle, we could assign N′ as the number of valence electrons in the highest occupied molecular orbital (HOMO) with an energy corresponding to B. For molecular species MX, knowledge of the electron distribution is needed for this purpose. Most of the species of interest can be considered ionically, as opposed to covalently, bonded; eg. M^+X^-. An ionic bonding model model has previously proven effective in predicting bond dissociation energies and ionization potentials, as mentioned earlier (section 1).

For each M^+, X^-, there exists an isoelectronic element M', X' with the same electron configuration and in some instances (particularly for X′) with similar size and, we assert, with similar cross section behavior. For M^+ and X^-, the ionic radii are close to the radii of M' and X' respectively. For higher valent M^{n+} cases, the M' radii are significantly larger [10]. Also, internuclear separations in ionic bonding molecules are significantly less than the combined M′ + X′ atomic radii. The proposed comparability between M^+ and M', for example, should be contrasted with the dramatic differences in $\sigma_M{}^+$ (free ion) and σ_M ,
eg. $\sigma_{Ba}{}^+ \sim 2 \times 10^{-20} m^2$ [11] vs. $\sigma_{Ba} \sim 17 \times 10^{-20} m^2$ [7]. (From this point on the $10^{-20} m^2$ unit factor will not be cited explicitly.) Such differences underscore the historical difficulties associated with atomic additivity cross section models.

As a key approximation to the MCM model, we obtain effective values for N' from M' and/or X' as follows. From the basic model form of eq. (1), it follows that:

$$N' = g\, \sigma_{M'}\, B_{M'}\,, \qquad (2)$$

and similarly for X'. Thus N' becomes an empirical parameter and is not necessarily an integer. The proportionality constant g is obtained by use of a value, or averaged species set of values, of, for instance, $\sigma_{M'}$ and $B_{M'}$ with an assigned value (s) of N′ based on the known atomic electron configurations and energies. For this purpose, we may select a case (s) where at E_m for M' only the HOMO level is ionizable, eg. Ca where N′ = 2. This calibration process is not essential, as a further empirical normalization for obtaining f (for molecules using eq. (1)) also encompasses g. However, this interim step provides useful model insight as we find a set of N' values for M', X' atoms that are consistent with expected valences and their periodicity. It is anticipated that the effect of many of the model simplifications made with respect to more rigorous models will be compensated for by this isoelectronic approach to model parameterization.

Combining eqs. (1) and (2), together with the model assumption that N'_{MX} is given by the sum of the N′ values for each M′ and X′, the molecular model is then given by:

$$\sigma_{MX} = k\, B_{MX}^{-1} (\sigma_M' B_M' + \sigma_X' B_X') , \qquad (3)$$

where k (= fg) is a fixed universal constant for all MX and other ionic bonding species. Corresponding expressions follow for the more polyatomic cases, ie. the prime terms continue to be summed for each additional atom. We note that the summation of N′ terms assumption has a parallel in the classical model (s) summation of orbital σ_i's. Also, the representation of N'_{MX} as σ - containing terms for isoelectronic atoms has the effect of introducing, empirically, collision factor information to the model, as discussed in section 2.1.1.

A value of k is obtained empirically from the slope of a linear least-squares fit to several reference species experimental σ_{MX} values versus the term following k in the above eq. (3). In principle, only a single experimental value is needed for this purpose. However, we averaged over several of the species where good experimental and model reliability was expected, ie. CsCl, CsI, SiO, and SiF_2, and where different laboratories and methods were used. With this approach, we find k = 0.62 ($\pm$ 0.04). The species σ's for this reference set also fall within the 95% confidence limit for the complete (51 species) data set, as given later in section 3, Table 1, Fig. 1.

From the model expression (eq. 3), we see that the model form is that of a scaled additivity of isoelectronic atoms where the empirical factor (0.62) scales for the lower σ of moleceules versus atoms. The B ratios scale for the effect of molecule formation on the ionization level. Factors contributing to a σ reduction on molecule formation include: electron participation in bonding orbitals, formation of ion pairs with reduced orbital extension in space, and possible shielding of a normally accessible orbital by the presence of neighbor atoms or, more particularly, ions.

2.2 Model extension to an ion cross section additivity principle

An alternate, heuristically attractive form of the model is given by:

$$\sigma_{MX} = 0.62\, \sigma_M'(B_M'/B_{MX}) + 0.62\, \sigma_X' (B_X'/B_{MX}) ,$$

which may be considered an isoelectronic component, scaled ion-additivity model. The factor 0.62 accounts for the typical (though not necessarily universal) lowering of cross sections on molecule formation, while the B ratio terms also account for changes resulting from molecule formation. This form may also be considered as an ion additivity model, in contrast with conventional atom additivity models. Moreover, we typically find

$$B_M'/B_{MX} < 1 \text{ and } B_X'/B_{MX} \sim 2.$$

These factors then effectively account for the coulombic interaction-based expected inequalities $\sigma_{X^-} > \sigma_X'$ and $\sigma_{M^+} < \sigma_M'$.

From the ionic model of ionization potentials [3], it follows that values of B_{MX} also include the coulombic effect of the presence of an adjacent, oppositely charged ion on the ease of electron removal during ionization. In the event that the model did not adequately represent the cross section differences between isolated M^+ vs. M' and X^- vs. X', we would expect to find systematic and opposite differences between model and experimental values for M' or X' dominance. No such trends have been found. We note that differences between $\sigma_M{}^+$ and $\sigma_{M'}$ can be small, eg. as for:
$C^{2+} \sim Be$, $Li^+ \sim He$, $K^+ \sim Ar$ (11).

From these considerations, it is possible to derive from the model or from experimental σ_{MX} data, values of $\sigma_M{}^+$, $\sigma_X{}^-$, etc. for additivity use, ie. where:

$$\sigma_{MX} = \sigma_M{}^+ + \sigma_X{}^-.$$

These ionic cross sections are then not those of isolated ions but are effective values for use as components of molecular species. A comprehensive set of ionic cross sections has been calculated, and the values generally follow the relations:

$$\sigma_X{}^-/\sigma_{X'} \sim 0.9\ (\pm 0.3)$$
$$\sigma_X{}^{2-}/\sigma_{X'} \sim 1.8\ (\pm 0.3);$$
for closed-shell configuration:
$$\sigma_M{}^+/\sigma_{M'} \sim 0.03\ (\pm 0.03)$$
$$\sigma_M{}^{2+}/\sigma_{M'} \sim 0.03\ (\pm 0.03);$$
for open-shell configuration:
$$\sigma_M{}^{n+}/\sigma_{M'} \sim 0.3 - 0.9 \text{ range.}$$

Here, the terms closed- or open- shell configuration have their usual meaning. That is, a closed-shell cation or anion molecular component has a full-shell electron complement, similar to that of a rare gas atom. The inherent stability of a closed-shell leads to relatively high B values and low σ values. Conversely, for the open-shell case, one or more electrons are readily available for ionization, leading to low B, high σ values.

While this ion-additivity approach is very satisfactory, we prefer the more rigorous model of eq. (3) where explicit inclusion of B_{MX} is considered. For cases where such data are not available or easily calculated, the ionic additivity form of the model may be useful.

2.3 Electron localization

2.3.1 Heteronuclear systems

For application of the model, consideration of electron localization is desirable, although it is not critical to the general applicability of the model, as the relative contribution of cation or anion centers to the nature of the ejected electron is generally accounted for by the $\sigma_M' B_M'$ (ie. N_M') and $\sigma_X' B_X'$ (ie. N_X') terms in eq. (3). For a cation closed-shell electron configuration, the cation contribution to the overall cross section is negligible, as noted in section 2.2. In addition, electron removal from a cation is appreciably more difficult than from a neutral isoelectronic atom. Hence, for such a case, the $\sigma_M' B_M'$ term is not included in eq. (3). For the open-shell case, both cation and anion contributions are considered.

In the extreme delocalization case we consider the bonding as covalent and we find, as in earlier studies [1], that

$$\sigma_{MX} \sim \sigma_M + \sigma_X \, .$$

For several of the systems considered here we find, from differences in electronegativity, from changes in binding energy on ionization, and from other bonding considerations, a comparable weighting of ionic and covalent character. In these cases, an average of the fully ionic and fully covalent models gives very good agreement with experiment (as will be shown in section 3.1).

Arguments concerning electron localization (ie. at M^+ or X^-, or both) may also be given support where ion intensity ($\sim \sigma$) vs. E appearance potential curves are known. For instance, the SiF, SiF_2, SiF_3 set of species is exceptionally well characterized from the σ vs. E measurements of Freund et al [12 – 14] and from the molecular orbital (MO) and BEB σ calculations of Kim et al [4]. For SiF, the σ vs. E curve is very similar to that of the M′ element Al. For SiF_2, the curve is shifted to higher E than for the M′ = Mg curve, consistent with an expected additional contribution of F^- to σ. A similar behavior is noted for SiF_3. These indirect arguments are verifiable, in this particular species set, from the MO results [4], where: for SiF about 90% of the orbital contributions to σ_M are of Si^+ character; for SiF_2, 70%; and for SiF_3, 25%.

In the MCM model, where the terms $\sigma_M' B_M'$ etc. derive from the concept of effective N′ contributions, the relative values of these terms for M′ and X′ are also indicative of orbital contributions to σ. Using this approach, we find 77% Si^+ character for SiF, 65% for SiF_2, and 25% for SiF_3, in good accord with the above MO results. Thus for these cation open-shell species, the inclusion of cation and anion terms in the model (eq. (3)) is consistent with independent MO results.

Application of the ionization potential ionic model to expected ionic bonded species, such as CsI and ZrO, gives good agreement with experimental B's, where electron loss is from the anion and primarily the cation, respectively. For significantly covalent species, such as GaCl, markedly different B values are obtained using an ionic model as compared with experiment. For GaCl, the ionic model yields B ~ 12 eV for

either anion or cation electron localization cases, versus 10.1 eV by experiment. Similar differences are found for SnCl.

Earlier theoretical work on diatomic metal halides indicated a predominantly ionic bonding-type [3, 17], and the location of the lowest removal energy (HOMO) electron and its B value were readily calculated. From the change in bonding energy resulting from ionization, as represented by $D_{MX}^{+} - D_{MX}$, the nature of the ejected electron could also be surmised [15]:

$$D_{MX}^{+} - D_{MX} = B_{MX} - B_{M} . \qquad (4)$$

Application of the MCM ionization cross section model to similar species utilizes an a priori assignment of the electron localization, similar to that of the earlier above-mentioned work.

For closed-shell species, such as the alkali halides, where the $M^{+}X^{-}$ configuration leads to $M^{+}X$ on ionization and $D_{MX}^{+} << D_{MX}$, the removed electron originates primarily at X^{-}. The rare gas atom, isoelectronic with X^{-}, is then used to represent the cross section properties of X^{-} which, in combination with the experimental B_{MX}, effectively accounts for the influence of M^{+} on the X^{-} electron removal energy. Similar arguments apply to other closed-shell, electron complement molecular species, eg. the dioxides of Ti, Zr, Ce, Th; and oxides such as BaO, Li_2O, UO_3 and W_2O_6, in addition to WF_6. For the heavier and more polyatomic of these species, ie. W_2O_6 and WF_6, we can expect a more delocalized electron character and the values of $D_{MXn}^{+} - D_{MXn}$ generally reflect this behavior. Thus for these latter cases, all nuclei are considered in the σ model calculation.

For open-shell molecular species, typically those where M is at less than its maximum valence, the most accessible electron is located at M^{n+}, eg. for the monoxides of V, Si, Ti, Zr, Hf, Y, Ce, La, Th, and U. In these cases (except for SiO), there is no significant difference between D_{MX}^{+} and D_{MX} and therefore M′ (M^{2+}) together with X′(O^{2-}) are used to model σ.

For sulfides and the other chalcogenides, which characteristically are more covalent than the corresponding oxides, the $D_{MS}^{+} - D_{MS}$ values indicate removal of a partly-bonding electron. Hence, for these (open-shell) species, S^{2-} (and Se^{2-}, Te^{2-}) and M^{2+} each contribute significantly to the ionized electron, eg. for US, GdS and PbS.

For very polyatomic cases, an increased delocalization in electron character results, eg. for As_4O_6 where M′ (Zn) and X′ (Ne) each contribute to σ. Similarly, for smaller species where a significant covalent character is present as evidenced by MO electron distributions, electronegativity differences, etc., a delocalized electron case applies, eg. for GaCl, GeCl, and SnCl. For GaCl, ionization greatly diminishes the bond energy, which is not in keeping with an ionic model and electron (e)-removal primarily from Ga^{+} which has two readily available e's. This observation further supports the other indicators of a significant covalency for this species, thereby leading to a low MCM

model σ value based on a Ga^+Cl^- charge distribution. These arguments are also supported by earlier molecular orbital results on charge distribution and orbital mixing [17]. For a partially covalent closed-shell species such as HCl, where e-removal for an ionic model would be from Cl^-, a large bond energy reduction would result from ionization, ie. similar to that of the alkali halides. However, only a small change is noted, in keeping with a delocalized electron character and significant covalency.

In principle, one can use electronegativity, molecular orbital calculations, or other bonding arguments, to estimate the degree of covalency or partial charge present in M^+X^- species, for instance. When this is done, eg. for GaCl, GeCl, SnCl, then a weighted averaging of σ's from the present ionic model and from additivity (~covalent case) can be shown to give much closer agreement with experiment (see section 3.1). For most high temperature species, the degree of ionicity is sufficiently large that such an adjustment is unnecessary.

2.3.2 Homonuclear systems

Homonuclear molecules M_n, typically where n = 2 – 5, are prevalent high temperature species. Here, the ionic model would not appear to be applicable. However, the principle of isoelectronic analogy may be successfully applied using the following formalism. For the simplest case of M_2, we represent the electron configuration as an electron pair bond, ie. M: : M, irrespective of the normal valence of M. Here, each M provides an electron pair to bond formation and each M nucleus formally becomes M^{2+} in the M_2 molecule. The isoelectronic M′ for M^{2+} is then used to model σ in the same manner as for heteronuclear species. Comparison between model and experimental σ's indicates this approach to be very reliable, as will be shown in section 3.2. Trimers and tetramers are modeled similarly.

2.4 Heteronuclear dimer systems

Dimers such as $(M_nX_m)_2$ where n, m ≥ 1 are particularly common high temperature species. From limited experimental evidence, the following empirical relationship has been developed [20] and is widely used [5]:

$$\sigma\,(MX)_2 = 1.5\,\sigma_{MX}\,.$$

In a more recent relationship, the 1.5 factor is reduced to 1.25 ± 0.35 [1]. Homonuclear systems have similarly been estimated and the reliability of such estimates will be indicated in section 3.4.

A model test of this dimer/monomer relationship can be made using the system

$$2\,WO_3 = (WO_3)_2.$$

An experimental value of σ = 11.4 is known for $(WO_3)_2$ [1]. As no σ value is available for WO_3, we use the ionic model to indicate a value of σ = 6.5. Similarly, the MCM model value for $(WO_3)_2$ is σ = 13.4. Application of the empirical 1.5 factor to the

monomer gives $\sigma = 9.8$ for the dimer. Each of these values is within the uncertainties of model and experiment. On the other hand, application of the atomic additivity model gives $\sigma = 26.2$.

2.5 Cross sections for the atoms

Experimental σ's are unavailable for a majority of atoms [1] and for some of the elements, where multiple studies have been carried out, appreciable differences have been noted. The only complete, self-consistent set of σ's appears to be the calculated results of Mann [7], which we have used for this work with a few noted exceptions. Comparison between Mann's values and experimental results, where available, is usually satisfactory with the notable exception of the Group IIIA elements measured by Freund et al [16]. The experimental values appear anomalously high (by ~ 37%), but Kim and Stone [21] have shown theoretically that autoionization has enhanced σ, as discussed below (section 2.5.1). Also, for Group IVA, the σ values of [16] are moderately higher (~20%) than those of [7]. Hence the experimental values [16] are used for Groups IIIA and IVA. For Group IA, the experimental σ_m values of Rb [18] and Cs [1] are also higher (~18%) than those of [7], on account of autoionization, and they are used in the model. For heavy elements such as Th, the abundance of energy levels increases the possibility of autoionization [19]. However, only direct ionization model σ values are available [7]. In summary, the following σ values, given in parentheses, were used here in preference to those of Mann [7]: Al (9.9), Ga (9.2), In (12.2), Rb (10.2), Cs (est. 13.1), Si (6.7), Ge (7.5), Sn (9.8), Pb (8.3), P (5.3), As (6.1), Sb (8.3). For the lightest elements H and He, more recent, accurate experimental and model results [1] supplant the Mann values.

We prefer Mann's values using his relation V as opposed to IV (see in [7]), the former being the basis for his later values [7]. In addition to the maximum values of σ and E, Mann's calculations also provide σ's as a function of E. These data, however, are only available in the recent survey [1]. It should be noted that if Mann's [7] data are renormalized to a more recent and more precise value of σ_{Ar} [16], they are decreased by 8%. This change is compensated for in the present work within the k normalization factor of eq. (3).

2.5.1 Autoionization-enhanced cross sections for the elements

In addition to direct ionization, which can be satisfactorily modeled [7, 22], a few elements are known or suspected to be candidates for excitation autoionization. This phenomenon can occur where excitation is to a quasi-bound state above the ionization level with decay to the ion state outweighing radiative decay [23]. Such an effect is expected to be limited to a relatively few elements where appropriate energy levels are present above, but near, the ionization limit.

In view of the periodicity of the electron configurations for the elements, candidate groups of elements can be, or have been, identified. These include, in decreasing order of significance, the groups III_A , I_A , and III_B. Relatively small cross section enhancements may be expected in a few other elements of groups IV_A, VI_B, and possibly the actinides. The best examples, established experimentally [16] and theoretically [21], are Al, Ga, and In, in addition to B and probably Tl [21]. As an aside, early experimental evidence for an unusually high σ_{Ga} was cited by Mann [7] from the work of K. Gingerich. The measurements of Freund et al [16] and the model values of Mann [7] are in good agreement for direct ionization cases; we have therefore selected the Freund et al values [16] for autoionization to supplement the Mann set [7] of atomic cross sections for use with the MCM σ model. When this is done, good model agreement is found for MX cases where M′ is an autoionized atom, consistent with the presence of a similar autoionization contribution to σ_{MX}.

2.6 Energy scaling of cross sections

In its most convenient and accurate form, the model provides maximum σ values (σ_m). Also, the majority of high temperature mass spectrometric cross sections available for comparison with the model are for E_m , or for some other single E value which is scalable to E_m. When scaling σ_m to other E values giving σ_E , any of the following five procedures may be used. Several of these procedures take into consideration the ionic bonding character of MX species. We estimate that E-scaling over a wide interval (ΔE) from E_m to values near B_{MX} , or vice versa, could lead to a doubling of the σ uncertainty (see section 3).

A number of scaling procedures are considered here as each has particular advantages/disadvantages. As noted elsewhere [1], methods based on a simple proportionality of σ and (E – B) are likely to be more uncertain over large ΔE, or where autoionization is present. For scaling over relatively large ΔE, the approach defined by eq. (8) is found to be more reliable than those of eqs. (5) – (7), but here E_m needs to be known. However, even when E_m is estimated, eq. (8) usually leads to more reliable σ's than eq. (7), for instance. In some cases, estimation of E_m can be problematic. The corresponding values for M′ (or X′ or both) appear to provide an upper limit estimate for E_m. We note that so systematic trends for predicting E_m are found for E_m/B ratios for MX species or between MX and M′ or X′. For closed-shell configurations, σ varies slowly over a large ΔE range near E_m and hence the accuracy of an E_m estimate is not critical to the σ-scaling result in this case.

In view of the additional σ_E uncertainty resulting from scaling from E_m to E values near the ionization threshold, it would seem desirable to carry out mass spectrometric experiments at E_m when utilizing the MCM model. This is often not practical, however, owing to interference from electron impact fragmentation, as discussed in detail elsewhere [1]. In principle, this difficulty can be largely avoided

through use of beam modulation [24]. A proper accounting of all fragment ions arising from the molecule of interest is also required when the mass spectrometric data are interpreted using model σ's which are total ionization cross sections for singly charged positive ions.

2.6.1 σ_E from σ_m and appearance potential curves

Actual values of E_m can usually be obtained most accurately from experimental appearance potential (AP), ie. ion intensity (I) vs. E curves. Relative values of σ_E / σ_m can also be obtained from such curves and these data may be used, together with model σ_m values, to obtain absolute values of σ_E. Thus $\sigma_E = \sigma_m (I_E/I_m)$. However, for cases where AP data are not available, the form of σ vs. E, up to E_m, may be approximated as that of M′ or X′ or some combination thereof, depending on the electron localization mode used in the model. This approach appears to be a reasonable approximation. For instance, the form of the σ_{Cd} vs. E curve [1] provides a good representation of the known curve for SnCl [25]. This approach is considered most suitable for cases when the electron is principally localized at either M or X.

2.6.2 σ_E from MCM model and (E – B) differences

The common practice of σ - scaling using (E – B) differences may be used although significant errors can occur [26, 27], particularly over large intervals or where autoionization is present. The assumption of the model concerning E/B terms terms in the BEB and other classical models also may be less reliable at higher E's (see section 2.1). Thus the model is likely to be most reliable for relatively low E_m cases (< 50 eV). Fortunately, many high temperature species are candidates for relatively low E_m behavior.

The following procedure is recommended, combining the MCM model with the common scaling approximation for $E < E_m$, namely: $\sigma_E \alpha (E - B)^{1.1} \alpha (E - B)$. Hence, to a good approximation:

$$\sigma_{MX,E} = 0.62 (\sigma_{M',E} B_{M'}) B_{MX}^{-1} (E - B_{MX})(E - B_{M'})^{-1} \quad , \qquad (5)$$

and similarly for X′ electron localization. Good agreement is found, for instance, with the experimental σ(E) data for SiF [12] and SiF_2 [13].

2.6.3 σ_E from $\sigma_{M'}$ and (E – B) differences

Alternatively, the following scaling procedure may be used to convert σ_{MX} to a value at $E < E_m$; eg. for X′ electron localization:

$$\sigma_{MX,E} = \sigma_{M',E} \sigma_{MX} \sigma_{X'}^{-1} (E - B_{MX}) (E - B_{X'})^{-1}. \qquad (6)$$

A term in $(E_{M'}, _{max} - B_{M'}) / E_{MX,max} - B_{MX})$, not included in this relation, can be assumed to be near unity to a good approximation, thereby avoiding use of E_m values which may not be well known.

2.6.4 σ_E from σ_{MX} and (E – B) differences

It should be noted that a few cases may occur, eg. for X′ a rare gas, where $E < B_{X'}$. For such a case, the procedure of eq. (6) is not applicable and E_m must be considered explicitly and is either measured or approximated by $E_{m, M' (or X')}$. Then

$$\sigma_{MX,E} = \sigma_{MX} \ (E_{MX} - B_{MX}) \ (E_{m,MX} - B_{MX})^{-1} \ . \qquad (7)$$

A more rigorous analytical model, based on a coupling of classical limiting behavior at low (Wannier Theory) and at high (Born approximation) E, is given by [28]:

$$\sigma_{MX,E} = \sigma_{MX} \ 3.86 \ [\ (E_{MX} - B_{MX})(E_{m,MX} - B_{MX})^{-1}]^{1.127} \div [0.8873 + (E_{MX} - B_{MX})(E_{m,MX} - B_{MX})^{-1}]^{2.127}. \qquad (8)$$

This model is also applicable at $E > E_m$, but is subject to the approximation of single orbital dominance. A test of the model on the σ (E) vs. E curves for Mg, Ag [16], and GaCl [25] shows very good agreement with experiment and to E > 100 eV. Thus, where E_m is reasonably well known, this model can be coupled with the MCM model – determination of σ_m to provide a complete curve of σ (E) vs. E. For known E_m , eq. (8) is estimated to yield $\sigma_{MX,E}$ values with an additional $\delta \sim 10\%$ over that of σ_m. For estimated E_m , an additional $\delta \sim 30\%$ is possible. In view of the apparent utility of this scaling approach for expanding the range of application of the MCM model to more than a single energy (E_m), the desirability of measuring E_m , where possible, is clear.

3. Results and discussion

3.1 Comparison of model with experiment

As a test of the model, and for the possible identification of anomalous or erroneous experimental molecular cross sections, we compare in Table 1 and Fig. 1 model and, to the extent possible, all known experimental values. Only σ_m comparisons are given here as most of the experimental data are at or near E_m. In the previous section (2.6) methods were given for scaling to or from other energies.

The model results were calculated using eq. (3) and the following examples illustrate the process involved. Consider SiF, where the electronegativities of Si and F indicate Si^+F^- as the likely electron configuration to be considered with the ionic MCM model. The isoelectronic M′ and X′ are then Al and Ne, respectively, from which the bracketed term of eq. (3) becomes:

$$(\sigma_{Al} B_{Al} + \sigma_{Ne} B_{Ne}).$$

The maximum ionization cross sections of Freund et al [16] and the corresponding ionization potentials are used to determine this term and hence σ_{SiF}, the maximum ionization cross section (see Table 1a). For the homonuclear case, consider C_2 as an example. According to the proposed formalism (section 2.3.2), the electronic structure is $C^{2+} :: C^{2+}$ for which M′ = Be. Hence the bracketed term becomes $(2\sigma_{Be} B_{Be})$, from which the maximum ionization cross section for C_2 is determined.

Uncertainties (δ) associated with experimental cross section data were considered in [1] for a number of the molecules included in Table 1. Reported δ values range from 10% to 100%, or more, with 20% being typical of the more accurate results [25]. For the MCM model, we estimate the σ uncertainties to be within $\delta = \pm 30\%$. Input data uncertainties to the model include (δ values in parentheses): B_{MX} (5%), $B_{M'}$ (<1%), k (<2%), $\sigma_{M'}$ (20%). In addition, for the range of E_m/B values considered here, the model approximations discussed in section 2.1 are estimated to be reliable to within $\delta = 20\%$. The overall model uncertainty estimate is supported by model-experimental comparisons for over 50 molecules where $\delta < 30\%$.

In keeping with the primary model objectives, the survey of experimental σ data is limited, in Table 1.a, to condensible inorganic species where the bonding is appreciably ionic. In Table 1.b we consider, in addition, several significantly covalent species for comparison purposes. A survey of experimental and various model results for primarily covalently bonded, gaseous species (some inorganic) has recently been made by Deutsch et al [29], and supplemented by Probst et al [30]. Before discussing the tabulated results, we reiterate the degree of independence of the model from experimental values, with the exception of the scaling factor (k) which is based on a small set of experimental values.

3.1.1 Treatment of experimental data

The following comments pertain to procedures used to obtain the experimental results of Table 1. For $NaBO_2$ and KBO_2, the σ_e experimental values are based on model values of NaF (~ 1.0) and KF (~ 1.2) respectively. The experimental values are probably lower limits as the electron impact energy used may have been less than E_m. For C_2, the BEB model value [32] is used as an "experimental" result. A moderately higher value ($\sigma = 3.9$) was calculated [29] using the so-called DM formalism. Similarly, for C_3F_8 [34] and SiF_4 [4, 32], the BEB model values are used as "experimental."

Where possible, or necessary, the experimental values have been scaled to an appropriate E_m for comparison with the model. This was done for the species ZrO_2, CeO_2, ThO_2, ThO, NaCl, CsCl, PbS, PbSe, PbTe, LiF, BaO, in addition to S_2, Se_2, As_4 and Te_2 using the scaling procedures discussed in section 2.6, with preference given to that of eq. (8) where possible. Many of the experimental σ values are the result of $\sigma\gamma$ species ratio measurements, with γ ratios either estimated as an $M^{-0.5}$ or $M^{-0.4}$ dependence

or neglected. In a few instances, γ has been measured (eg. [20]) without any obvious systematic or predictable trend for high temperature molecules. For the most part, γ uncertainties are within δ limits but the rare possibility of an $\delta > 30\%$ in σ due to unmeasured or poorly estimated γ's cannot be discounted. Usually, the experimental value of σ will be too high if an unaccounted for γ–effect is present.

3.1.2 Treatment of model data for autoionization

For SiF, the autoionization-enhanced σ for Al [16] was used as the model M′ value. Similarly, for YO, the autoionized σ value for M′ = Rb [30] was used. For LaO, where M′ = Cs, the autoionization enhancement of Cs was estimated from Rb. This estimated enhancement for σ_{Cs} is also supported by the known autoionization of the isoelectronic case, Ba^+ [35]. The selected cross section agrees with one of the experimental determinations, namely that of Tate and Smith, as reported in [36]. For Se_2 , the M′ = Ge experimental value [16] was used. For As_4 , the autoionization value of σ_{Ga} [16] was used for M′ in the model. For GaCl and SnCl, the Freund et al [16] σ_{Ga} (autoionization) and σ_{Sn} (autoionization?) values are used for the covalent case. Similarly, for the ionic component of GeCl, σ_{Ga} [16] was used.

3.1.3 Partial covalent cases

A few representative cases where the bonding character is between the extreme cases of ionic or covalent are considered in Table 1.b. An average value of the two model cases gives very good agreement with experiment. We are reluctant to extend the model to cases that are even more covalent, owing to an ambiguity in assigning an appropriate M′ (or X′), and the likely significant contributions of high energy orbitals together with high E_m values (as discussed in section 2.1). A case in point is $HgBr_2$, where σ vs. α (polarizability) correlations (see section 3.3) and other considerations indicate a predominantly covalent character. High values of $\sigma \sim 20$ and $E_m \sim 70$ eV are found experimentally [37]. Additivity of the elements gives $\sigma \sim 15.4$, which is still within the $(\delta) \sim 30\%$ uncertainty for model – experimental σ comparisons. A similar value is obtained from σ vs. α relationships (section 3.3). The species In_2O and In_2S also appear to be predominantly covalent and the reported [1] In_2O/In cross section ratio (with δ of $\pm$ 50% and hence not included in Table 1) agrees with either a covalent or a partly ionic, autoionization (see section 3.2) model prediction.

3.1.4 Discussion of results

A source of potential difference between model and experiment, eg. as with VO, results from difficulty, in the latter case, in accounting for all ion contributions to σ_e. In some instances the σ_e results may be partial σ's only and hence represent a lower limit to σ - total. For SiF_3 , the model result is notably higher than experiment (Table 1). We

note that the model use of B to represent all contributing orbitals, including those with energies higher than B, could lead to too large a σ value. However, the BEB model, which includes all appropriate orbitals, leads to a similar disagreement [4]. This anomaly has been discussed in the literature in terms of a steric interference effect of each F^- restricting access by the incoming ionizing electron to the lone electron on Si^{3+} [38]. Such steric effects are not readily accounted for by this or other models except to the extent that they affect B, but even if they occur such cases appear to be rare. Also, steric effects appear to be more significant at higher E [39] and E_m for SiF_3 is uncharacteristically high considering its open-shell electron configuration.

Another case where the model is notably higher than experiment is UO_2. Perhaps a similar steric effect to that discussed for SiF_3 is the cause of the low experimental value. However, the experimental difficulty associated with accounting for fragmentation and the simultaneous presence of UO and UO_3 may also contribute to a low experimental result (see also section 3.2).

For CS (Table 1.b), the MCM ionic case ($C^{2+}S^{2-}$) somewhat fortuitously is in exact agreement with experiment. This is surprising in view of the similar electronegativities of C and S and a high degree of covalency in CS. The electron pair bond model (for : C : : S :) gives essentially the same result, whereas an average value for C_2 and S_2 is $\sigma \sim 4.5$. For As_4O_6 , an additional lower E experimental value is 10.6 at 20 eV [33]. With E-scaling, this value is consistent with the higher E value listed.

Inspection of Table 1, and the corresponding graphical representation of Fig. 1, indicates no case where model and experiment disagree to more than the $\delta = \pm 30\%$ uncertainty estimate. This is remarkable agreement as the experiments, except in a few instances, are lacking in precision and the model is greatly simplified from the usual classical approaches. These results, then, serve to provide (a) overwhelming empirical support for the reliability and general utility of the model, and (b) support for the overall reliability of the various experimental approaches and results.

Several empirical observations of σ trends [1] are also supported by the model. For the empirical ratios of partial cross sections, $\sigma_{MO}/\sigma_M \sim 0.65 \pm 0.1$, the corresponding average model value is 0.63; however the range is from 0.09 (BaO/Ba) to 0.99 (UO/U). As the model values are for total σ's, they represent an upper limit for comparison with experiment. Similarly, for the experimental ratios $\sigma_{MO2}/\sigma_{MO} \sim 0.5 \pm 0.25$, the average model value is 0.4 with a range of 0.2 to 0.9. The outliers notably have significantly different electron configurations which, as the model reveals, are a key determinant for the magnitude of σ.

3.1.5 Comparison with other models

Conceptually, one could envision possible extension of the model, eg. to include, explicitly, higher level orbitals and E/B terms. However, given the demonstrated model reliability, additional complexity does not appear warranted, even where feasible. It

appears that the use of $\sigma_{M'}$ and $\sigma_{X''}$ terms in the model adequately represents the orbital occupation and energy-dependence characteristics of the MX species being modeled. This assertion is well supported from a comparison of the MCM and BEB [4] model results for SiF_2 , and SiF_3 , where the two models give essentially the same result. For SiF, some partial improvement in agreement between the BEB model and experiment was obtained if the kinetic energy terms in the BEB model were reduced, arbitrarily, by a factor of 3 [4]. However, the contribution of autoionization (see section 3.2) seems a more likely explanation for the low BEB model σ_m value for SiF, which is based on direct ionization only. The MCM model results also compare favorably with the DM model [29, 30], eg. for BF_3 , CF_2 , CF, and C_2.

Model extension to the determination of partial ionization cross sections (σ_i) is considered impractical although, for relatively simple high temperature species, the ionic bonding concept does provide guidance to the degree of electron impact fragmentation expected [40]. For a few simple covalent species, a semiempirical model (at high E) has been used recently [41]. The most practical approach to determining σ_i appears to be the experimental determination of fragmentation pathways, coupled with the use of model σ_m.

3.2 Autoionization in molecular species

As indicated above (section 2.5), autoionization is reasonably well established as a contributing pathway to ionization for a select number of atoms. However, there appear to be no established cases for molecules in general and for ionic bonded species in particular. Application of the MCM σ model, where direct ionization atomic σ's [7] are used, provides direct ionization molecular cross sections. For cases where the model values lie well below experimental values, autoionization is reasonably indicated. A few such cases, discussed in section 3.1.2, are given in Table 1.

Where use was made of available $\sigma_{M'}$ data containing the effect of autoionization, the σ_{MX} model result usually agreed well with experiment, thereby confirming the assignment of molecular autoionization, eg. for SnCl, GaCl, GeCl, SiF, YO, and LaO. It is particularly pertinent that the BEB model result for SiF using direct ionization only [4] is significantly less than the experimental value whereas the MCM result using M′ = Al agreed with experiment. Notably, no cases of an enhanced autoionization (ie. >M′) due to molecule formation were indicated.

Another possible candidate species for autoionization is UO. However, in this case where M′ = Th, no work appears to have been done yet that would reveal autoionization in Th, although such a heavy atom is a reasonable autoionizing candidate [19]. For UO, several reasons may be offered to explain the difference between the two experimental σ values (see Table 1). First, as was pointed out by the authors of the higher value [27], the number of coexisting species and the presence of extensive electron impact fragmentation complicates the quantitative assignment of UO^+ to UO vs. UO_2 and UO_3. However, the

peaking of UO^+ ion intensity ($\sim \sigma$) at low E is pronounced and experimental error may not be the sole explanation. The most likely physical phenomenon is autoionization to an excited energy state of UO^+ above, but very near, the ionization threshold. This process could produce a strongly peaked appearance potential curve at low energies. At high energy, the direct ionization process would be more evident. Hence the lower apparent σ_{UO} value at high E most likely mainly represents the direct ionization process.

With the ionic model, the electron configuration of U^{2+} is represented by Th ~ (Rn) $7s^2$ $6d^2$, modified by the field of O^{2-}. Ionization of UO would then lead to a configuration Th^+ ~ (Rn) $7s^2$ 6d, with low lying configurations of (Rn)7s $6d^2$ and (Rn)$7s^2$7p also present. A similar known autoionization case, $Ca^+ \rightarrow Ca^{2+}$ involves 4s $\rightarrow$ 4p transitions [35]. In this case, electron impact results in an electron transition to a quasi-bound state of Ca^+ above the ionization threshold. This effect in UO should be evident in an appearance potential curve of Th^+(Th). A small segment of the Th^+(Th) AP curve is known [42] near the threshold, with an apparent $E_m \sim 12$ eV, as compared with a calculated [7] direct ionization value of 31 eV. This E_m difference is consistent with autoionization. Also, the low E_m value for Th is consistent with the corresponding value for UO of ~ 8 eV. However, for the limited data available, no sharp peaking is apparent for Th^+, unlike the case for UO.

Depending on the location of M^+ energy levels that lie above B, it appears that one may find autoionization enhancement of σ over a narrow ΔE interval near B or, more typically, over a wide ΔE range at E >>B. Thus cases may occur where no enhancement is apparent at high E, eg. as with UO [43] and the σ model would then remain applicable if $E_m >> E$ for autoionization resonance.

With respect to the σ_{UO} behavior at low E, we conclude that both the experimental artifact and autoionization arguments presented here are plausible, but that further work is needed. For this reason, the higher value of σ_{UO} given in Table 1 was not included in Fig. 1 even though the data point falls within the $\delta \sim 30\%$ uncertainty limit.

The reported ratio $\sigma\gamma$ (Sc)/ $\sigma\gamma$ (Ag) = 4.17 at 25 eV [44] indicates $\sigma_{Sc} \sim 14$, vs. the direct ionization value of 9.5 [7]. However, application of this value of σ_{Sc} (ie. as M′) to the σ_{VO} model would increase the model value to well above the experimental result. This observation suggests the high σ_{Sc} value to be in error, even though Sc is an <u>a priori</u> candidate for autoionization.

Based on known or expected autoionization for M′, the following representative species types may be expected to show enhanced σ's due to autoionization. For each set, M′ is indicated in parentheses:

SrF , Sr_2O, (Rb); BaF, Ba_2O, ZrF_3 , ZrOCl (Cs); CF (B); SiCl (Al); GeF, AsO (Ga); SnF, SbO (In); PbCl, BiO (Tl); TiF, VF_2 , CrF_3 (Sc); ZrF, NbO, $MoCl_3$

(Y); CeF, PrO, $NdCl_3$ (La); MnF, FeO, CoF_3 (Cr); ScO, TiF_3, (Ca^+ [37]); CeF_3 (Ba^+ [37]); ZrF_3 (Sr^+).

Based on the known autoionization of Ca^+ and Ba^+, one might anticipate similar behavior for Mg^+ and hence for AlO and SiF_3. However no evidence for autoionization was found for SiF_3 (see Table 1).

Similar examples for M_2 species include:

Si_2 (Al); As_2 (Ga); Sb_2 (In); Bi_2 (Tl); La_2 (Cs), etc.
For these candidate species, those based on M′ = B, Al, Ga, In, Tl, are expected to show an autoionization enhancement of ~37%, in slight excess of the model δ = 30% uncertainty limit. For the other cases, the difference between direct [7] and autoionization [16] $\sigma_{M'}$ is less than 20% and a similar degree of enhancement is expected for the counterpart molecular species.

For CF, the reported experimental $\sigma_m \sim 1.5$ (loc. cite [29]) and the MCM model values agree for M′ = B where the direct ionization σ_B value [7] is used. However, applying a model-predicted autoionized σ_B value [21] with the MCM model gives $\sigma_{CF} \sim 2.6$. On this basis we suggest that the σ_{CF} experimental value is too low.

In concluding these considerations of autoionization in molecular species, we reiterate the key observation that the isoelectronic atom (M′), with established autoionization cross section enhancement, provides a good representation of autoionization in MX. At the present time, no other models are able to consider autoionization in molecular species.

3.3 Model cross section – polarizability (α) relationships

Empirical relationships, with some theoretical rationale, between σ and α have often been noted in the past [45, 46], principally for covalent species. Similar underlying factors influence both σ and α, namely the presence of low lying electronic states, the spatial extension of orbitals, and the ease of electron transfer to higher states.

The general trends of α, known for a few anions and cations [47], within the periodic system and those of σ_M^+ and σ_X^-, or of σ_{MX} in the present model, are found to be similar. Table 2 shows a convincing comparison between σ and α data, particularly for the cesium and magnesium halides which were modeled (see Table 1 for CsCl, CsI) as an anion X′ case. The σ_{MX} model values for CsCl, CsBr, CsI also duplicate, exactly, the trend for α_{HX} for the corresponding hydrogen halides [45]. The close correspondence between α_X^- and model σ_{MX} is particularly striking and may be taken as verification of a direct σ vs. α relationship and of the MCM model. Values of α_X' show similar trends but are about a factor of two less than the corresponding α_X^- and cesium halide σ_{MX}

values. This latter observation is consistent with our earlier comments (section 2.2) concerning $\sigma_X^- > \sigma_X'$. It follows from the above observations that the MCM model may be used to estimate anion and cation polarizabilities.

In Table 2 we also compare known molecular α's for inorganic species [48] with the corresponding model and experimental σ's; the same general trends are found, particularly if the bond component to α can be separated from total α [49]. On the basis of the good one-to-one correlation found between σ and α, it is reasonable to suggest that the relatively high $MgBr_2$ and UF_6 experimental cross sections may be in error. Indeed, experimental difficulty with $MgBr_2$ was noted owing to the presence of oxybromide impurities. The σ vs. α relationship observed here follows that suggested earlier for covalent species [46].

3.4 Dimer cross section rules

For dimer species of the type M_2 , $(MX)_2$ etc., cross sections are usually estimated from:

$$\sigma_{M2} \sim 1.5\, \sigma_M \quad [5]$$

or

$$\sim 1.8\ (\pm 0.2)\, \sigma_M \quad [1].$$

The M_2 species considered in Table 1 indicate, however, that the model monomer to dimer factor varies significantly for different M, ie.: $C_2/C = 1.6$, $Ag_2/Ag = 1.5$, $As_4/As_2 = 1.8$, $S_2/S = 1.4$, $Se_2/Se = 1.2$, $Te_2/Te = 1.1$.

For $(MX)_2$ species, the MCM model reduces to the form:

$$\sigma_{(MX)2} = 2(B_{MX})(B_{(MX)2})^{-1}\, \sigma_{MX}.$$

Values in the range of 1.7 – 1.9 are then calculated for the monomer to dimer factor for the following alkali halides: LiCl, NaCl, KCl, and CsCl, which are somewhat higher than the literature approximation of 1.5. On this basis, reported [5, 6] partial pressures of these alkali halides could be high by about 20%.

3.5 Model comparison with additivity and consequences for thermochemical studies

A few representative cases are considered in Table 3 in order to indicate the differences between the conventional additivity and MCM models. In recent years, the likely overestimation of σ's using the additivity model has been recognized and an arbitrary 25% or other empirically based reduction has sometimes been made (see discussion in [1]). However, as shown in Table 3, reductions of about 1000% may sometimes be necessary, particularly for closed shell electron configurations. For open shell cases, the errors are not so egregious, typically less than 100%. That such

differences can be expected is readily apparent from inspection of the periodic nature of σ_M and B_M and the sharp differences present between adjacent elements, corresponding to $M \rightarrow M^+$ or $X \rightarrow X^-$, for instance.

The authors of the comprehensive thermochemical database IVTANTERMO [5] have allowed for molecular σ uncertainties of 150% in their error assessments. They also follow the dimer/monomer ~ 1.5 σ rule. A σ uncertainty of 150% typically leads to an uncertainty in high temperature enthalpies of ~ 8 k Joule $mole^{-1}$, depending on temperature, and can be the main source of data uncertainty. As we have shown, even this seemingly conservative σ uncertainty estimate can be low by an additional factor of six.

In view of the possibility of large errors associated with ionization cross section estimations, one might expect to find literature examples where, eg. Second and Third law – based enthalpies, or D^o_{MX} obtained from mass spectrometric equilibria vs. spectroscopic, photodissociation etc., disagree beyond the expected experimental uncertainties. Without resorting to a systematic search for such cases, several representative examples are considered as follows.

The enthalpy of formation of SiF_2 is based on measured enthalpy changes (ΔH) for reactions such as

$$2CaF + Si = 2Ca + SiF_2.$$

In this particular case, the Second and Third law ΔH's differ by about 40 k Joule $mole^{-1}$ [50]. For the Third law determination, the additivity σ model was used. Application of the MCM model indicates that this procedure overestimates the reaction equilibrium constant by at least an order-of-magnitude, which corresponds to 20 k Joule $mole^{-1}$. With this correction, the Second and Third law ΔH's differ by a more acceptable 20 k Joule $mole^{-1}$.

Similarly, for the well-studied case of AlO, original differences between D^o_{AlO} from MS vs. spectroscopic methods [5, 6] can be explained through use of lower σ_{AlO} values predicted from the present model.

An example of application of a modified additivity model is the PN system [51]. For PN, additivity, modified additivity, and the MCM model lead to the following σ values: 6.0, 7.2, and 3.3 respectively. Hence, in this case, the reported partial pressure (p) of PN, resulting from this σ analysis, is likely to be too low by a factor of two (as $p \sim \sigma^{-1}$).

A further example, where the Gryzinski model was used to calculate σ_{LiF} and hence LiF partial pressures, is as follows [52]. The authors used the ratio σ_{LiF}/σ_{Ag} =

0.61, as compared with the present value of 0.2 (from Table 1). Hence their LiF partial pressures are too low by a factor of three. A comparison of their pressures with those of JANAF [6] indicates the latter to be a factor of 2.5 x greater, which is consistent with the use of too high a σ_{LiF} value in [52].

Other examples of excessively low mass spectrometrically determined partial pressures (by an order of magnitude) were noted more than thirty years ago for species such as PtO_2 and RuO_3 [53]. One of the explanations offered by the authors was the possible use of estimated cross sections that were too high. Application of the present model to their data does explain, at least in part, the observed discrepancies between the mass spectrometric and transpiration vapor pressures.

For other cases, where the bonding is significantly covalent and/or the electron configuration is open-shell, earlier estimates are not too different from the MCM model values and thermodynamic data inconsistencies are not as apparent. For instance good Second-Third law accord is found for D^{o}_{LaSe} [54].

From these few examples it is apparent that past practice in estimating ionization cross sections can lead to significant errors in thermochemical data. However, as has been discussed in detail elsewhere [1], with the use of appropriate experimental and data analysis procedures, such errors can often be avoided or their presence at least revealed. For those cases where reliance on cross sections is unavoidable, application of the present model should markedly reduce the data uncertainties.

4. Summary

In summary, the following procedure is recommended in applying the MCM cross section model. First, identify the likely ionizing electron character (bonding, non-bonding, cation-like...) based on the ionization potential change resulting from molecule formation, or the change in bond energy on ionization. Second, identify from common valence considerations whether the constituent cations and anions have a closed or open shell electron – complement. Third, identify if the molecule can be expected to have some covalent character, or if its many atom complement (typically > 3 atoms) would favor significant electron delocalization. This criterion essentially represents the degree to which the molecule can be expected to depart from the ideal case of complete ionic bonding. From these three steps, it should be possible to attribute either anion, or anion together with cation, as contributors to ionization. Then use the isoelectronic counterpart atoms to simulate the cross sections of the component ions. This information, together with a knowledge of the molecule ionization potential, is sufficient to allow for prediction of ionization cross sections for virtually any high temperature species or other inorganic molecule.

The accuracy of the model predictions appears comparable with or, in some instances, better than that of experimental methods. A least squares difference of only 2% is found from a comparison between the model and experimental values for fifty-one molecules. For an individual species, the main source of model uncertainty appears to

arise from the cross sections of the isoelectronic atoms. For the most part, the calculated direct ionization values of Mann [7] and, more recently, of others [22, 55], appear sufficiently accurate for use with the model. For the few cases where an unknown autoionization contribution may be present, the model values could be low but still within the assigned 30% uncertainty limit.

Acknowledgements

Discussions with Dr. Yong-Ki Kim on the BEB model and autoionization of Al, Ga, and In are acknowledged, in addition to general discussions with colleagues Drs. David W. Bonnell, Jean Drowart, and Christian Chatillon on cross sections and high temperature mass spectrometry.

References

[1] J. Drowart, C. Chatillon, J.W. Hastie, and D.W. Bonnell. "Determination of Thermodynamic Properties for Condensed Phases and Gases with the Mass Spectrometric Knudsen Cell and Vapor Transport Methods: Accuracy, Precision, and the Influence of Ionization Cross Sections," to be published, Pure Appl. Chem. (2001).

[2] K.S. Krasnov, N.V. Karaseva, Opt. and Specty., 19 (1965) 14;
J.L. Margrave, J. Phys. Chem. 58 (1954) 258. These are representative works, amongst numerous others.

[3] J.W. Hastie, J.L. Margrave, Fluorine Chem. Rev. 2 (1968) 77.

[4] W. Hwang, Y-K Kim, M.E. Rudd, J. Chem. Phys. 104 (1996) 22.

[5] L.V. Gurvich, I.V. Veyts, C.B. Alcock, Thermodynamic Properties of Individual Substances, 4th Ed., Vols. 1 – 3. Hemisphere Pub. Corp., N.Y., 1989.

[6] M. Chase, Jr., NIST – JANAF Thermochemical Tables, 4th Ed., J. Phys. Chem. Ref. Data Monograph 9, NIST, Gaithersburg, MD, 1998.

[7] J.B. Mann, In Recent Developments in Mass Spectroscopy, Proc. Conf. Mass Spectroscopy, Tokyo (K. Ogata, T. Hayakawa, Eds.), University Park Press, Baltimore, MD, 1970, p. 814; also J. Chem. Phys. 46 (1967) 1646; more recently a similar formalism (known as DM) has been used, with empirical input, for gaseous molecular species [29].

[8] M. Gryzinski, Phys. Rev. A 2 (1965) 336.

[9] B. Peart, S.O. Martin, K.T. Dolder, "Recent Measurements of Cross Sections for the Ionization of Ions by Electron Impact," in Sixth Intl. Conf. Phys. and Electron and Atomic Collisions, 1969, p.1.

[10] R. Rich, Periodic Correlations, W.A. Benjamin, Inc., N.Y., 1965.

[11] M.A. Lennon, K.L. Bell, H.B. Gilbody, J.G. Hughes, A.E. Kingston, M.J. Murray, F.J. Smith, J. Phys. Chem. Ref. Data 17 (1988) 1285.

[12] T.R. Hayes, R.C. Wetzel, F.A. Baiocchi, R.S. Freund, J. Chem. Phys. 88 (1988) 823.

[13] R.J. Shul, T.R. Hayes, R.C. Wetzel, F.A. Baiocchi, R.S. Freund, J. Chem. Phys. 89 (1988) 4042.

[14] T.R. Hayes, R.J. Shul, F.A. Baiocchi, R.C. Wetzel, R.S. Freund, J. Chem. Phys. 89 (1988) 4035.

[15] J.W. Hastie, J.L. Margrave, High Temp. Science 1 (1969) 481.

[16] R.S. Freund, R.C. Wetzel, R.J. Shul, T.R. Hayes, Phys. Rev. A 41 (1990) 3575.

[17] J.W. Hastie, J.L. Margrave, J. Phys. Chem. 73 (1969) 1105.

[18] Y.-K. Kim, J. Migdalek, W. Siegel, J. Bieron, Phys. Rev. A 57 (1998) 246.

[19] E.W. McDaniel, Atomic Collisions, Wiley and Sons, N.Y., 1989, p. 392.

[20] R.T. Meyer, A.W. Lynch, High Temp. Science 5 (1973) 192.

[21] Y.-K. Kim, P.M. Stone, "Ionization of Boron, Aluminum, Gallium and Indium by Electron Impact," in press, Phys. Rev. A (2001).

[22] Y.-K. Kim, M.E. Rudd, Phys. Rev. A 50 (1994) 3954.

[23] R.H.G. Reid, Photon and Electron Collisions with Atoms and Molecules, Ed. P.G. Burke, C.J. Joachain, Plenum, N.Y., 1997, p. 37.

[24] D.W. Bonnell, J.W. Hastie, K.F. Zmbov, High Temp. High Press. 20 (1988) 251.

[25] R.J. Shul, R.S. Freund, R.C. Wetzel, Phys. Rev. A 41 (1990) 5856.

[26] J.W. Hastie, Pure Appl. Chem. 56 (1984) 1583.

[27] P.E. Blackburn, P.M. Danielson, J. Chem. Phys. 56 (1972) 6156.

[28] J.M. Rost, T. Pattard, Phys. Rev. A 55 (1997) R5 – R7.

[29] H. Deutsch, K. Becker, S. Matt, T.D. Mark, Int. J. Mass Spectr. 197 (2000) 37.

[30] M. Probst, H. Deutsch, K. Becker, T.D. Mark, Int. J. Mass Spectr. 206 (2001) 13.

[31] K.J. Nygaard, Y.B. Hahn, J. Chem. Phys. 58 (1973) 349.

[32] Y.-K. Kim, private communication of unpublished BEB model result, NIST, 2001; result of [29] also from a model.

[33] J.W. Hastie, unpublished observation, NIST, 2001.

[34] H. Nishimura, W.M. Huo, M.A. Ali, Y.-K. Kim, J. Chem. Phys. 110 (1999) 3811.

[35] D.C. Griffin, M.S. Pindzola, C. Bottcher, J. Phys.. B. At. Mol. Phys. 17 (1984) 3183.

[36] R.H. McFarland, Phys. Rev. 159 (1967) 20.

[37] W.J. Wiegand, L.R. Boedecker, Appl. Phys. Lett. 40 (1982) 225.

[38] M. Bobeldikh, W.J. Van der Zande, P.G. Kistemaker, Chem. Phys. 179 (1994) 125.

[39] C. Vallance, S.A. Harris, J.E. Hudson, P.W. Harland, J. Phys. B: At. Mol. Opt. Phys. 30 (1997) 2465.

[40] J.W. Hastie, J.L. Margrave, High Temp. Sci. 1 (1969) 48.

[41] S. Pal, S. Prakash, S. Kumar, Int. J. Mass Spec. 184 (1999) 201.

[42] R.J. Ackerman, E.G. Rauh, High Temp. Science 5 (1973) 463.

[43] A. Pattoret, J. Drowart, S. Smoes, Trans. Faraday Soc. 65 (1969) 98. See also [1].

[44] L.L. Ames, P.N. Walsh, D. White, J. Phys. Chem. 71 (1967) 2707.

[45] P.W. Harland, C. Vallance, Int. J. Mass Spec. Ion Proc. 171 (1997) 173.

[46] F.W. Lampe, J.L. Franklin, F.H. Field, J. Amer. Chem. Soc. 79 (1957) 6129.

[47] M.J. Sienko, R.A. Plane, Physical Inorganic Chemistry, W.A. Benjamin Inc., N.Y., 1963.

[48] CRC Handbook of Chemistry and Physics, 79th Ed., CRC Press, N.Y., 1998.

[49] R. Kremens, B. Bederson, B. Jaduszliwer, J. Stockdale, A. Tino, J. Chem. Phys. 81 (1984) 1676.

[50] T.C. Ehlert, J.L. Margrave, J. Chem. Phys. 41 (1964) 1069.

[51] M. Guido, G. Gigli, High Temp. Science 7 (1975) 122.

[52] M. Yamawacki, M. Hirai, M. Yasumoto, M. Kanno, J. Nucl. Sci. Tech. 19 (1982) 563.

[53] J.H. Norman, H.G. Staley, W.E. Bell, Advan. Chem. Series 72 (1968) 101.

[54] R.Y. Ni, P.G. Wahlbeck, High Temp. Science 4 (1972) 326.

[55] H. Deutsch, K. Becker, T.D. Mark, Int. J. Mass Spec. Ion Proc. 151 (1995) 135.

Table 1.a - Molecular Species Model (σ_m) and Experimental (σ_e) Maximum Ionization Cross Sections, Ionization Potentials (B) and Maximum Energies (E_m)

Species	Model [d] σ_m (10^{-20} m^2)	Experimental σ_e (10^{-20} m^2)	Ionization Potential B, eV	Max Energy [a] E_m, eV
Closed Shell				
LiF	0.9	1.0 [24] b	11.3 c	55 [52]
Li_2O	1.7	2.0 [1]	6.2 c	~70
NaCl	2.3	2.4 [26,33]	9.1 [3]	~50
$NaBO_2$	2.3	1.9 [1]	9.2 [1]	~80
KBO_2	2.5	1.7 [1]	8.6 [1]	~70
CsCl	3.5	3.5 [26,33]	7.8 c	~50
CsI	7.1	8.0 e	6.5 c	~50
BaO	1.6	1.8 f	6.9 c	50 f
TiO_2	2.3	2.6 [1]	9.5 c	50 v
ZrO_2	2.3	2.8 g	9.5 c	25 g
CeO_2	2.2	2.0 h	9.7 c	~25 o
ThO_2	2.5	3.2 [42]	8.7	~25 o
UO_3	3.0	2.5 [27]	10.6 c	25 i
W_2O_6	13.4	11.4 [1]	12.2 c	~70
WF_6	10.0	9.5 [32]	~ 13	~70
Open Shell				
BS_2	6.4	6.9 [1]	~8.5	~60
SiF	6.5	6.4 [12] t	7.3 [12]	30
SiF_2	4.1	4.2 [13] u	11.2 [13]	80
SiF_3	4.8	3.4 [14]	9.2 [14]	90
SiO	3.4	3.1 [1]	10.8 c,n	~30
TiO	7.5	6.8 j	6.7 c	30 v
VO	6.5	4.7 [1]	7.4 [1]	~30
YO	7.9	8.1 [1,44]	5.9 [1]	~20 m
ZrO	8.6	(8.6) g	6.5 c	~25 g
LaO	8.6	9.7 [1,44]	4.9 [1]	~20
CeO	12.8	11.0 h	5.2 [1]	11 h
ThO	11.1	11.0 [1,42]	6.1 [1]	16 [42]
UO	15.7	14.1 [1] 17.0 [27]	4.7 [27] p	~50 [43] 8 [27]
UO_2	14.3	11.6 [27]	5.5 [27]	18 [27]
VO_2	2.0	1.5 [1]	9.6 [1]	~20
PbS	8.0	6.6 [1]	8.6 [1]	~50
PbSe	9.0	8.2 [1]	8.4 [1]	~50
PbTe	10.5	11.5 [1]	8.3 [1]	~50
GdS	11.4	10.8 [1]	6.9 [1]	~20
US	16.0	17.2 [1] q	5.6 c	~30
C_2	3.4	3.2 [32] 4.0 [29]	10.9 c	~30
S_2	7.3	7.0 [1] k	9.4 c	~40
Se_2	8.2	7.9 [1] w	8.9 [1]	~40
Te_2	10.6	10 [1]	8.3 [1]	~40
Ag_2	7.8	7.5 [1]	7.3 c	~30
As_4	13.8	12.9 [1]	9.9 c	~50

Table 1.b - Heteroatom Cases With Significant (~50%) Covalency

Species	Model			Experimental	B	E_m
	Ionic	Covalent (additive)	Average			
Closed Shell						
HCl	2.0	3.6	2.8	2.3 [26] 2.7 l	12.7 c	~60
SiF_4	4.1	9.3	6.7	5.5 [32]	~13	100
C_3F_8	7.0	14,0	10.5	12.5 [34]	13.7 c	100
$TiCl_4$	11.7	22.3	17.0	15 r	11.7	30-100
UF_6	8.0	22.0	15.0	18 s	14	~80
Open Shell						
GaCl	5.4	12.6	9.0	9.1 [25]	10.1 [25]	40
GeCl	8.6	9.1	8.8	11 [25]	7.2 [25]	50
SnCl	10.4	13.7	12.0	11.7 [25]	6.8 [25]	35
CS	4.0	5.9	5.0	4.0 k	11.3 k	80
As_4O_6	18.1	27.8	23.0	23.0 [33]	9.5 [26]	~30

Table 1 Footnotes, References:

a. Estimated (~) values are based on analogy with similar species or on the corresponding values for M′ or X′ atoms, which probably provides an upper limit.

b. References, cited in main text, indicated in parentheses.

c. R.D. Levin, S.G. Lias, Ionization Potential and Appearance Potential Measurements, 1971 – 1981, NSRDS – NBS (NIST) 71 , 1982. J.G. Dillard, K. Draxl, J.L. Franklin, F.H. Field, J.T. Herron, H.H. Rosenstock, Ionization Potentials, Appearance Potentials, and Heats of Formation of Gaseous Positive Ions, NSRDS – NBS (NIST) 26 , 1969.

d. Atomic B values used in the model, available from various reference sources, eg. [48].

e. L.N. Gorokhov, N.E. Khandamirova, Advan. Mass Spec. B , Wiley and Sons, N.Y., 1985, p.1031.

f. J.W. Hastie, D.W. Bonnell, P.K. Schenck, Pure Appl. Chem. 72 (2000) 2111.

g. R.J. Ackerman, E.G. Rauh, C.A. Alexander, High Temp. Science, 7 (1975) 304; σ ratio ZrO/ZrO_2 given.

h. R.J. Ackerman, E. G. Rauh, J. Chem. Thermodyn. 3 (1971) 609.

i. Low value [27].

j. R.I. Sheldon, P.W. Gilles, in Characterization of High Temperature Vapors and Gases, NBS (NIST) SP 561, Ed. J.W. Hastie, U.S. Govt. Clearinghouse, 1979, p. 231.

k. R.S. Freund, R.C. Wetzel, R.J. Shul, Phys. Rev. A 41 (1990) 5861; a value of 5.7 is given as a partial σ for the parent ion.

l. From σ vs. α relationship.

m. Rb has two peaks at 10 and 40 eV [31].

n. An alternate B ~ 11.6 yields σ_m ~ 3.1; for B see D.L. Hildenbrand, Int. J. Mass Spectr. 197 (2000) 237.

o. Estimated from ZrO_2 E_m and periodic trends.

p. An alternate, probably more accurate value is 5.6, from G. Rauh, R.J. Ackerman, J. Chem. Phys. 60 (1974) 1396. However, we used the value of [27] to maintain a self consistent comparison with σ_e [27].

q. An alternate value of 13.7 is derived from the data of E.D. Cater, E.G. Rauh, R.J. Thorn, J. Chem. Phys. 44 (1966) 3106.

r. Cited in [29]; also DM model [29] gives σ_m = 16.3.

s. Cited in [40].

t. For the analogous species CF, σ_m = 2.3 (MCM model, σ_B auto [21]), or 2.5 (DM model [29]).

u. For the analogous species CF_2, σ_m = 3.5 (MCM model), or 3.1 (DM model [29]).

v. S. Banon, C. Chatillon, M. Allibert, High Temp. Sci. 15 (1982) 17.

w. σ_e scaled from 14 eV; an alternate σ_e value in [1] of 13.8 is considered an experimental outlier.

Table 2

Cross Section – Polarizability (α) Comparisons

Species	σ_{MX} model (10^{-20} m^2)	σ_{MX} exper. (10^{-20} m^2)	α_X^- [47] (10^{-30} m^2)	α_X' [48] (10^{-30} m^2)
CsF	1.1	–	1.0	0.4 (Ne)
CsCl	3.5	3.7	3.6	1.6 (Ar)
CsBr	4.6	–	4.8	2.5 (Kr)
CsI	7.1	8	7.1	4.0 (Xe)
			1.6 α_X^-	
MgF_2 a	1.6	(1.6) b	1.6	
$MgCl_2$	4.9	3.8	5.8	
$MgBr_2$	6.6	9.0	7.7	
MgI_2	9.3	10.4	11.4	
			α_{MX} [48]	
BF_3	4.3	3.6 c	3.3	
SiF_4	6.5	6.0 d	5.4	
SeF_6	8.7	---	7.3	
UF_6	15	18 e	12.5	
$AsCl_3$	12.7	---	14.9	
CS_2	7.6	---	8.7	

Footnotes:

a. B's, 13.5, 11.1, 10.6, 10.0 eV, from fluoride to iodide.

b. Experimental values, referenced to MgF_2 , measured by J. Berkowitz, J.R. Marquart, J. Chem. Phys. 37 (1962) 1853. These values are not included in Table 1 as they are not absolute measurements.

c. DM model [30].

d. BEB model [32].

e. Cited in [45].

Table 3

Cross Section Comparison for MCM and Additivity Models (units 10^{-20} m^2)

Species	MCM Model	Additivity
closed shell		
BaO	1.6	18.6
CsI	7.1	17.6
CsF	1.2	11.8
CeO_2	2.2	18.5
SrI	3.2	19.7
Li_2O	1.7	7.9
open shell		
As_4	13.8	20.0
As_4O_6	18.1	27.8
Se_2	6.1	10.0
TiF	6.8	9.7
Cs_2Te_2	38.3	40.2

Caption

Fig. 1. Comparison of model (σ_m) and experimental (σ_e) cross sections; solid curve represents an exact correspondence line for σ_m and σ_e which is virtually indistinguishable from a least squares fit; broken curves indicate uncertainty limits (δ) of $\pm$ 30%; least squares fit has a 0.95 coefficient of determination and the slope leads to $k = 0.62 \pm 0.01$, in agreement with the value based on four selected reference species (see text, section 2.1).

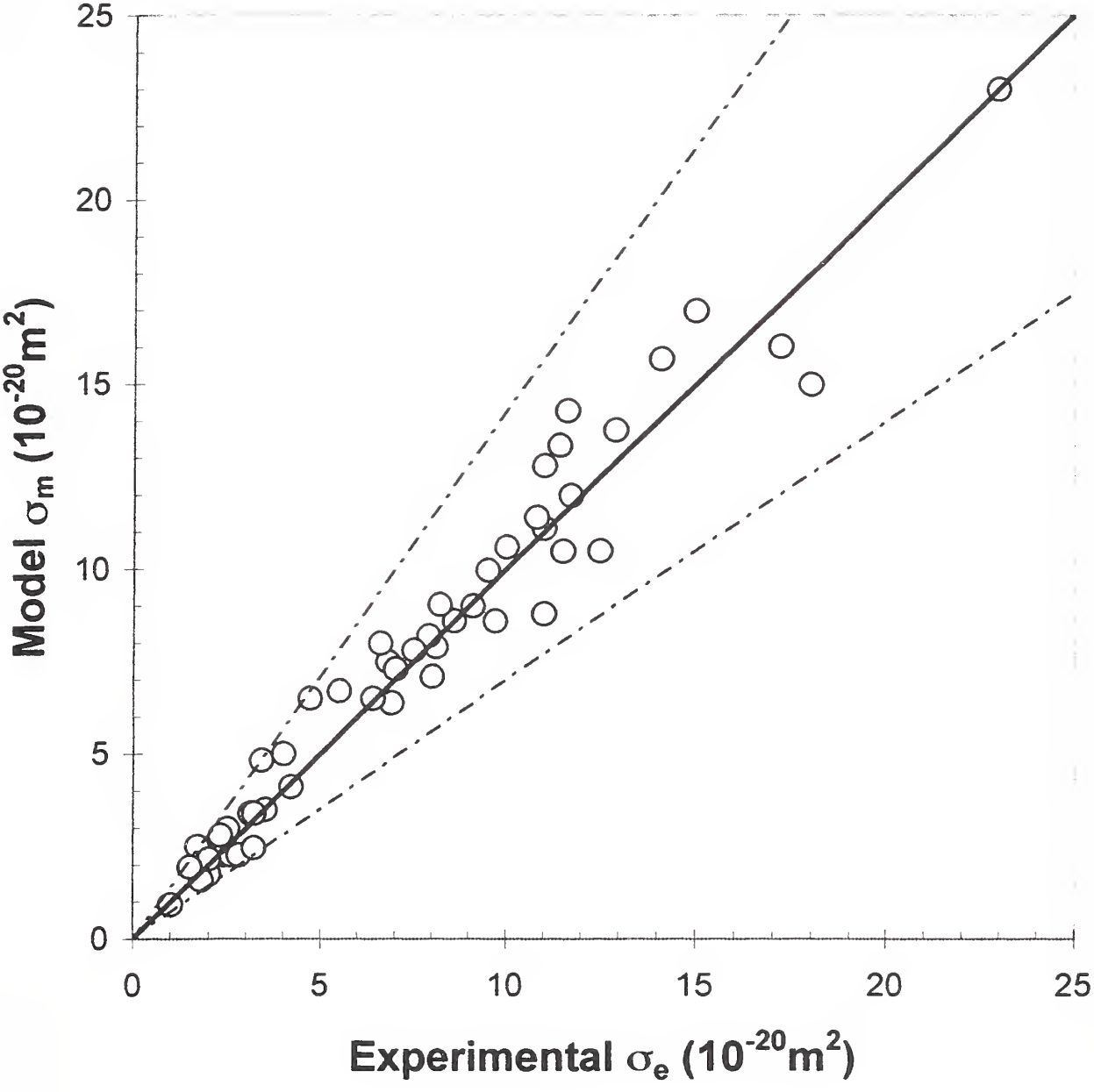
25
20
15
10
5
0
0
5
10
15
20
25
Model σ_m ($10^{-20}m^2$)
Experimental σ_e ($10^{-20}m^2$)